2014

The Development of a Novel Silicon on Insulator Microdosimeter with Sensitive Volumes Modeled after Living Cells

Anthony P. Mazza
Louisiana State University and Agricultural and Mechanical College, amazza2@gmail.com

THE DEVELOPMENT OF A NOVEL SILICON ON INSULATOR MICRODOSIMETER WITH SENSITIVE VOLUMES MODELED AFTER LIVING CELLS

A Thesis

Submitted to the Graduate Faculty of the
Louisiana State University and
Agricultural and Mechanical College
in partial fulfillment of the
requirements for the degree of
Master of Science

in

The Department of Physics and Astronomy

by
Anthony P. Mazza
B.S., Wheeling Jesuit University, 2006
May 2015

ACKNOWLEDGEMENTS

I am thankful to Dr. Oleg Vassiliev for his constant support and guidance throughout this project, especially with the simulation codes and understanding the theoretical basis of microdosimetry. I also thank my supervisory committee: Dr. Wayne Newhauser, Dr. Rui Zhang, and Dr. Jeff Blackmon. Dr. Newhauser's experience in experimental microdosimetry was very valuable to the project. Dr. Zhang was always ready with the tough questions to help further my understanding. Dr. Blackmon's expertise with silicon charged particle detectors, running the GEANT4 simulations to benchmark our in-house code, and providing the ^{241}Am source were all very beneficial.

I thank my classmate Andy Halloran for his many hours of service setting up the microdosimetry laboratory and helping me get the project off the ground. Thanks to Dr. Stephen Pittman for the analysis code and help in the lab. Dr. Kip Matthews and Paul Maggi's electronics expertise helped immensely with troubleshooting the device and modifying/maintaining the circuit boards.

Dr. James Ziegler of the United States Naval Academy and Quentin Dolecek provided the qMIDN device for this research. Dr. Anatoly Rozenfeld of the University of Wollongong provided SOI designs and lent us test chips. Dr. Brent Gila at the Nanoscale Research Facility fabricated the microdosimeters, and Jeff Chancellor of the National Space Biomedical Research Institute provided guidance and support. Dr. Frank Fronczek of the LSU Chemistry Department provided camera equipment. Susan Hammond, Paige Barcia, Arnell Nelson, Katie Bailey, and Yvonne Thomas helped with many administrative tasks and lightened the paperwork load.

Finally, I thank my family and friends for their constant love and support throughout this journey, especially Team Tony. You were my strength, to keep me from faltering.

TABLE OF CONTENTS

LIST OF TABLES

LIST OF FIGURES

ABSTRACT

Purpose: The purpose of this work was to test the feasibility of using a silicon on insulator microdosimeter, which mimics the size and shape of particular cells within the human body, to determine dose equivalent from a ^{239}PuBe neutron source with uncertainty less than 10%.

Methods: A batch of microdosimeters were analyzed in terms of their physical surface conditions and basic diode characteristics such as leakage current as a function of bias voltage, to select those with the best performance. A calibration protocol was developed utilizing an ^{241}Am alpha particle source and a reference tail pulse generator. Neutron spectra were acquired using two different converter layers placed atop the microdosimeter: a tissue-substitute converter made from high-density polyethylene, and a boron converter consisting of epoxy coated with boron powder. To compare the experimental results, a Monte Carlo code was written to simulate the alpha particle and neutron irradiations. Dose equivalent was determined using an average quality factor calculated for each spectrum on the basis of the ICRU definition (1986).

Results: Using the tissue-substitute converter, the cell-shaped microdosimeters were able to determine dose equivalent with uncertainty less than 10%. However, uncertainties were 13.5% when using the boron converter.

Conclusion: The cell-shaped silicon on insulator microdosimeters proved feasible for further research and development. With higher quality silicon chips, this type of microdosimeter could become a simple, small, and lightweight device to determine dose equivalent in real-time and to provide improved radiation protection for radiotherapy patients and personnel who are occupationally exposed to radiation.

1 INTRODUCTION

1.1 Overview

The field of microdosimetry consists of a conceptual framework and the corresponding experimental methods to analyze the microscopic distribution of energy deposition events in irradiated matter (ICRU, 1983). The regions of interest in microdosimetry are quite small, comparable to that of biologic cells and subcellular structures, since radiation effects in tissue strongly depend upon interactions at the cellular level. For such small regions, the primary dosimeter used has been the tissue-equivalent proportional counter (TEPC). Based upon Bragg-Gray cavity theory, the charge induced by radiation interactions within the counter's gas-filled cavity is a good measure of the absorbed dose to the surrounding material (Farahmand, 2004). However, TEPCs have some disadvantages including a relatively large physical size which limits spatial resolution and increases the chance of charge pile-up, and the addition of wall effects which will be discussed later.

Another type of dosimeter is the silicon semiconductor. These detectors offer much higher sensitivity, smaller physical size, and good mechanical stability (Rozenfeld, 2011). Silicon microdosimeters tend to suffer from poor definition of the sensitive volume from which charge is collected. It is possible for charge to diffuse into the depletion region from areas surrounding the sensitive volume. An improvement to this design is the silicon on insulator (SOI) microdosimeter. Such a device consists of a silicon p-n junction situated above a layer of silicon dioxide which acts as an insulator and prevents the collection of charge from the area below the sensitive volume. This allows the sensitive volume of the detector to be precisely defined.

With SOI technology, a device can be constructed which consists of an array of well-defined sensitive volumes. These sensitive volumes can be made to mimic the size and shape of actual cells. Microdosimeters resembling particular cells within the human body will allow for the study of the importance of cell size and geometry, which has been shown to have an appreciable effect on energy deposition within cells, especially for low doses of radiation (Byrne et al., 2013). Of particular interest are radiation sensitive cells.

1.2 Microdosimetric Quantities

The quantities used in microdosimetry to describe energy transfer are different than those typically used in a clinical medical physics environment. For this project, the most relevant quantities are energy imparted, ε, and lineal energy, y.

Energy imparted is a stochastic quantity measured in units of keV, which may be due to one or more energy deposition events within a volume.

$$\varepsilon = \sum_i \varepsilon_i. \tag{1.1}$$

The energy deposited in the volume by a single interaction, ε_i, is defined by (ICRU, 1983):

$$\varepsilon_i = T_{in} - T_{out} + Q_{\Delta m} \tag{1.2}$$

where T_{in} is the energy of the incident ionizing particle (exclusive of rest mass), T_{out} is the sum of the energies of all ionizing particles leaving the interaction (exclusive of rest mass), and $Q_{\Delta m}$ represents the changes of the rest mass energy of the atom and all particles involved in the interaction.

A more useful quantity is lineal energy, which is also stochastic and is commonly specified in units of keV/ μm. Lineal energy is found by

$$y = \frac{\varepsilon_s}{\bar{l}} \tag{1.3}$$

where ε_s is the energy imparted to the volume by a single event and $\bar{l}$ is the mean chord length of that volume. For a convex volume, subject to a uniform isotropic radiation field, the mean chord length $\bar{l}$ can be found using Cauchy's theorem (Kellerer, 1971a).

$$\bar{l} = \frac{4V}{S} \tag{1.4}$$

where V is the volume of the object, and S is the surface area. In other volumes, $\bar{l}$ can be found from stochastic simulations of chord lengths in the volume.

For presentation of microdosimetric data, there are a few different ways to plot the data. The lineal energy frequency distribution, $f(y)$, is the probability density of y. The dose distribution, $d(y)$, is the lineal energy distribution f(y) multiplied by y, and divided by $\bar{y}_F$.

$$d(y) = \frac{y}{\bar{y}_F} f(y) \tag{1.5}$$

where $\bar{y}_F$ is the frequency-mean lineal energy, and represents the 1st moment of $f(y)$.

$$\bar{y}_F = \int_0^\infty y f(y)\, dy. \tag{1.6}$$

The dose-mean lineal energy, $\bar{y}_D$, is a non-stochastic quantity and represents the second moment of $f(y)$ divided by the first moment of $f(y)$:

$$\bar{y}_D = \int_0^\infty y d(y) dy = \frac{1}{\bar{y}_F} \int_0^\infty y^2 f(y) dy. \tag{1.7}$$

The most common way to plot microdosimetric data is y•d(y) vs. Log_{10} y. This format is advantageous because the area under the curve between any two values of lineal energy is proportional to the dose deposited by those events.

1.3 Dosimeters

1.3.1 Tissue Equivalent Proportional Counter (TEPC)

The TEPC, or Rossi counter (Rossi & Rosenzweig, 1955), has some distinct advantages for microdosimetric measurements. The walls of a TEPC may be constructed of tissue-substitute material and are filled with a tissue-substitute gas, usually methane or propane based, with an elemental composition very similar to human tissue (Farahmand, 2004). An anode wire runs through the center of the cavity and the wall of the cavity acts as the cathode (Figure 1.1). There is also typically a helical wire surrounding the central anode that serves to provide a more uniform electric field in the volume between the two wires.

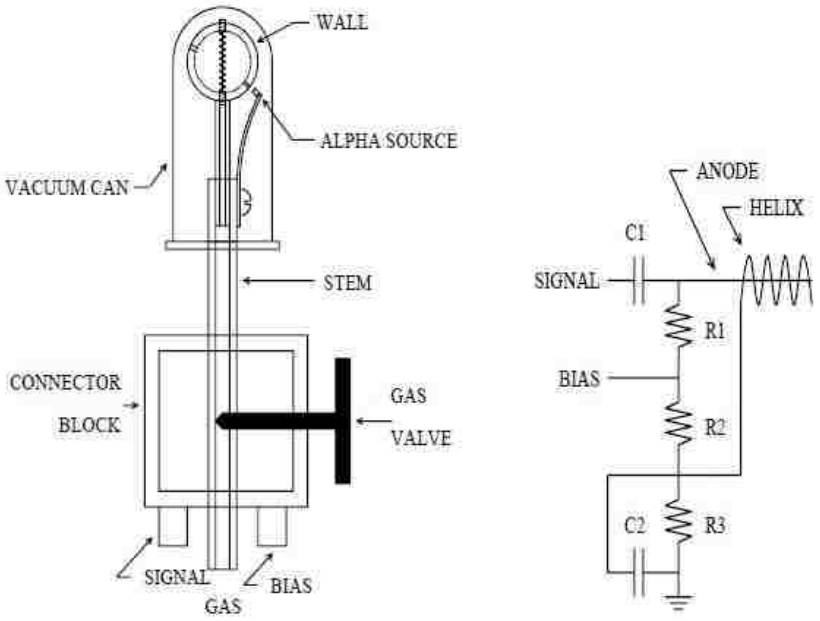

Figure 1.1: Mechanical schematic diagram and circuit diagram of Rossi counter (Newhauser, 1995).

The TEPC simulates a tissue volume much smaller than the physical size of its low pressure gas cavity. When radiation interacts with the filling medium of the detector, excitations and ionizations result. The high electric field between the central anode wire and the cathode wall (500-5000 V) enables secondary ionizations (charge multiplication in the gas cavity) to occur, proportional to the amount of primary ionizations (Farahmand, 2004). This property of gas multiplication allows the use of TEPCs in situations where the relatively few ion pairs created would not generate a sufficient signal with an ionization chamber, which operates at a much lower voltage (~300 V).

A charged particle crossing the volume of low-pressure tissue-substitute gas deposits the same amount of energy as the particle would if crossing a volume of tissue of microscopic diameter, if the following equation is satisfied: (Farahmand, 2004)

$$\left(\frac{1}{\rho}\frac{dE}{dx}\right)_t \rho_t \Delta x_t = \left(\frac{1}{\rho}\frac{dE}{dx}\right)_g \rho_g \Delta x_g \tag{1.8}$$

where $\left(\frac{1}{\rho}\frac{dE}{dx}\right)$ is the mass stopping power, ρ is the density, Δx is the distance traveled across the volume, and the subscripts *t* and *g* represent tissue and gas, respectively.

If the mass stopping powers of the gas and the tissue of interest are equivalent, then Equation 1.8 reduces to:

$$\Delta x_m = \frac{\rho_g}{\rho_m}\Delta x_g. \tag{1.9}$$

Thus, a TEPC can simulate a much smaller volume of unit density tissue. As an example, a 2.5 cm diameter sphere filled with tissue substitute gas at a pressure of 2.27 kPa will be equivalent to a 1 μm diameter sphere of unit density material in terms of energy deposited in the two volumes. Inherent in this conversion, however, is a scaling factor of

$2.5\ \mathrm{cm}\ /1\mathrm{x}10^{-4}\ \mathrm{cm}\ = 2.5x10^{4}$. This very large difference in physical size is an important source of uncertainty in absorbed dose and lineal energy.

Aside from the very large dimensional scaling factors necessary with TEPC measurements, there are some other clear drawbacks to this type of detector. Even though both the walls of the chamber and the filling gas are essentially tissue-equivalent, the two substances still have some differences in compositions and densities with respect to actual human cells. These discrepancies create distortions in the microdosimetric spectra that need to be taken into account. These effects are generally described as "wall effects." The higher density of the chamber wall causes more particles to scatter and increases the production of secondary and tertiary particles, thus imparting more energy to the sensitive volume than would occur in a homogeneous medium (Kellerer, 1971b). It is important to note that wall effects do not occur if the detector is of uniform density and if the sensitive volume of the detector is the same size as the tissue volume it was simulating.

The "delta ray effect" (Figure 1.2, a.) is when a charged particle enters the detector volume at the same time as one the delta rays it has created. The "re-entry effect" (Figure 1.2, b.) is when an electron passes through some portion of the detector volume but then re-enters the volume due to its circuitous path. The "V-effect" (Figure 1.2, c.) is caused by a nonelastic nuclear reaction which creates multiple nuclear fragments simultaneously, and the traversal of the detector volume by two or more of these fragments. The "scattering effect" (Figure 1.2, d.) is caused by an uncharged primary particle (e.g. photon or neutron) undergoing interactions which produce charged particles close enough together to enter the detector volume at the same time (ICRU, 1983).

There are some other disadvantages related to the large size of the low-pressure gas-filled TEPC. This large physical size seriously limits the spatial resolution of the measurements, and also hinders simulating an array of cells. Finally, in a high-intensity beam (i.e. a therapeutic beam) the TEPC suffers from sensitivity to pile-up effects due to the high fluence incident upon the large detection volume.

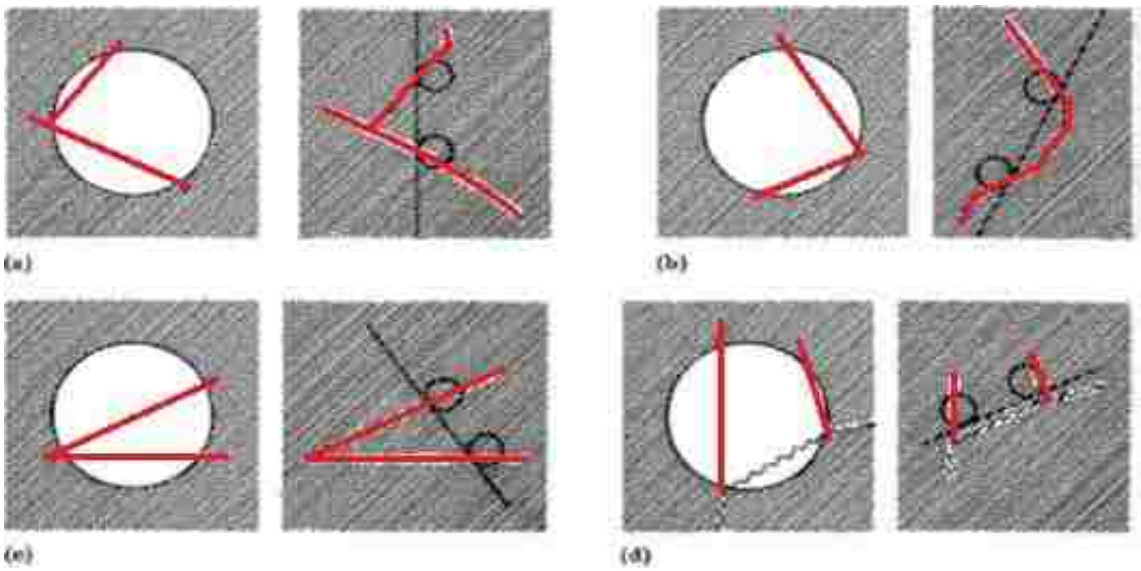

Figure 1.2: The four types of wall effects: (a) Delta Ray Effect (b) Re-Entry Effect (c) V-Effect (d) Scattering Effect. For each subset, the diagram on the left represents the experimental volume and the diagram on the right represents what would happen in a real, microscopic scenario. Adapted from (ICRU, 1983).

1.3.2 Silicon on Insulator (SOI) Devices

Semiconductors have useful properties for radiation detection purposes when n-type (doped with donor phosphorous atoms) and p-type (doped with acceptor boron atoms) materials are made to be in good thermodynamic contact with one another, allowing charge carriers to migrate across the junction (Knoll, 2000). Migration produces the depletion region (named for its very low mobile carrier density) at this interface as well as an electric field. As a result, the system acts like a high-resistivity parallel plate ionization chamber (Bradley, 2001). When ionizing radiation enters the depletion region

it will create electron-hole pairs which are then swept out of this region by the electric field (Knoll, 2000). The motion of these charge carriers creates the detector signal. Applying a reverse bias to the junction increases the size of the depletion region and improves charge collection.

While there are a number of materials that can be used to make semiconductor devices, one of the most common is silicon. The mean energy required to generate an electron-hole pair in silicon is 3.62 eV (Bertolini & Coche, 1968), which is about a tenth of the energy required for ionization in typical fill-gases used in proportional counters (Knoll, 2000). This lends a theoretical advantage to silicon detectors in terms of energy resolution. However, in practice, energy resolution is highly dependent on preamplifier noise levels (Bradley et al., 2001).

The ability to have the sensitive volume (henceforth referred to as SV) of the detector closely mimic the dimensions of the cell of interest is an advantage for SOI detectors. This virtually eliminates the wall effects inherent with a gas-filled TEPC in which the sensitive volume is thousands or tens of thousands times larger than the region of interest. Another clear advantage of this small size is the ability to create a detector with an array of SVs, akin to a group of cells in tissue.

To define the depth of the SV, SOI detectors utilize an insulating layer of silicon dioxide underneath the junctions (blue layer in Figure 1.3); this ensures that no charge is collected from underneath the SV. In addition to the insulating layer of SiO_2 underneath the active area of the detector, each SV is surrounded by a “guard ring” structure. The guard ring helps to reduce collection of charge from areas lateral to the sensitive volume or from adjacent SVs. This guard ring (yellow n-type area surrounding the SV in Figure

1.3) can be left floating, or biased with the same potential as the core electrode (Rozenfeld, 2013). Figure 1.4 shows the region within the silicon layer that would be the ideal SV; in reality the lower lateral edges of the SV near the SiO_2 layer will likely be somewhat blurred.

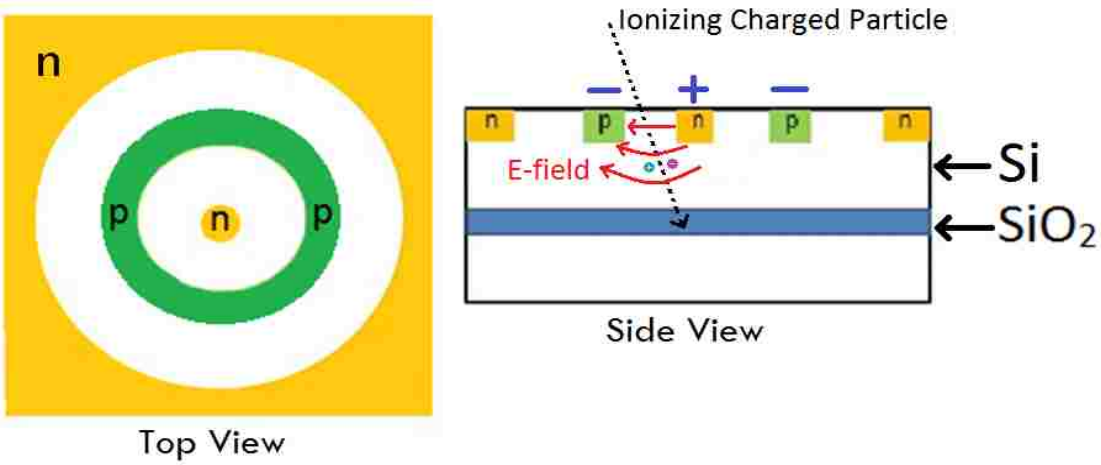

Figure 1.3: Top and side view of LSU SOI microdosimeter. Ionizing radiation creates electron-hole pairs in the intrinsic silicon. The electric field between the n- and p-type structures sweeps the electron-hole pairs out of the region, which generates a signal in the microdosimeter. Note the guard ring structure (large n-type area surrounding the SV) and the SiO2 insulating layer (blue area in figure on the right). (Adapted from B. Gila, personal communication, August 26, 2013)

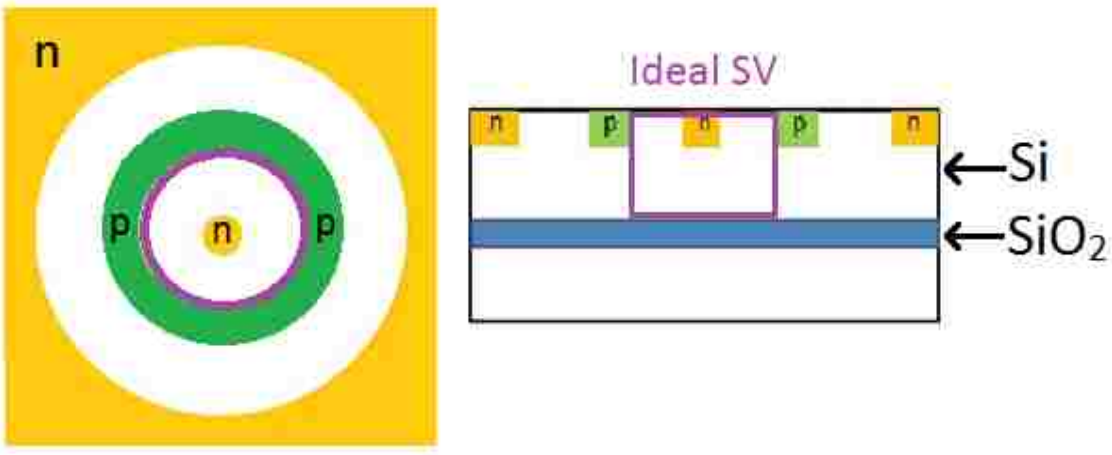

Figure 1.4: Top and side view of LSU SOI microdosimeter design showing outline of ideal SV region. (Adapted from B. Gila, personal communication, August 26, 2013)

Silicon detectors do, however, possess some disadvantages compared to TEPCs. One issue is that silicon is not directly tissue-equivalent, in terms of radiation interactions and energy deposition. To convert from absorbed dose in silicon to absorbed dose in tissue, a radiation species dependent absorbed dose conversion factor is required to account for range differences of ions in the materials. However, it has been demonstrated that 0.63 is a reasonable approximation for a wide range of ion types and energies (Bradley, 2000).

SOI detectors also tend to have noisier data compared to TEPCs. TEPCs are capable of resolving single ionization events as low as 0.05 keV/µm, whereas silicon detectors typically have a minimum resolvable energy deposition of 0.4 keV/µm or more (Bradley et al., 2001). Silicon detectors are susceptible to radiation damage effects that cumulate over time. The two types of radiation damage are bulk and surface effects (Wunstorf, 1997). The most basic bulk effect is the Frenkel defect which is when radiation interactions cause atoms of the semiconductor material to be displaced from their normal lattice locations (Knoll, 2000). These additional vacancies can trap charge carriers which leads to degradation in charge collection efficiency and energy resolution. Surface defects are mainly responsible for increased leakage current (Shiraishi, 1969) which also causes a loss of energy resolution. The approximate cumulative particle fluence thresholds at which radiation damage becomes an important consideration are listed in Table 1.1.

Table 1.1: Approximate threshold fluences for radiation damage to silicon (Pospisil & Granja, 2009).

Type of Radiation	Fluence (particles/cm^2)
Thermal neutrons	10^{14}
Fast neutrons	10^{12}
p, α, t, ions	10^{11}

1.4 Modeling Specific Cell Types

Previous SOI microdosimeters have used SVs of a size and shape similar to a generic human cell (Pisacane et al., 2011; Reinhard et al., 2005). In this work, we used SV sizes and shapes that mimicked specific human cells. Each SOI microdosimeter had four separate sections, with each section consisting of an array of SVs of a unique size and shape. Three of the arrays mimicked a specific type of cell, and the fourth replicated a design from the University of Wollongong (UOW), a collaborator on this project. Comparisons of detector response based on SV size and shape were facilitated by having all four SV designs on the same chip. The four shapes chosen and their rationale are described in the following sections.

1.4.1 Lens Epithelial Cell

There is a well-established link between ionizing radiation and the development of cataracts (Ainsbury et al., 2009; Otake & Schull, 1991). Ionizing radiation has been particularly linked to the formation of posterior subcapsular cataracts (PSCs) (Robman & Taylor, 2005). There are several distinct regions that make up the human lens (Figure 1.5): the lens capsule to isolate the lens from the vasculature; a single anterior layer of epithelial cells; and the elongated lens fiber cells (Augusteyn, 2010; Blakely, 2012). When

the actively dividing cells in the germinative region are damaged by radiation, they migrate to the posterior pole of the lens and can form a lens opacity (Evans et al., 1960).

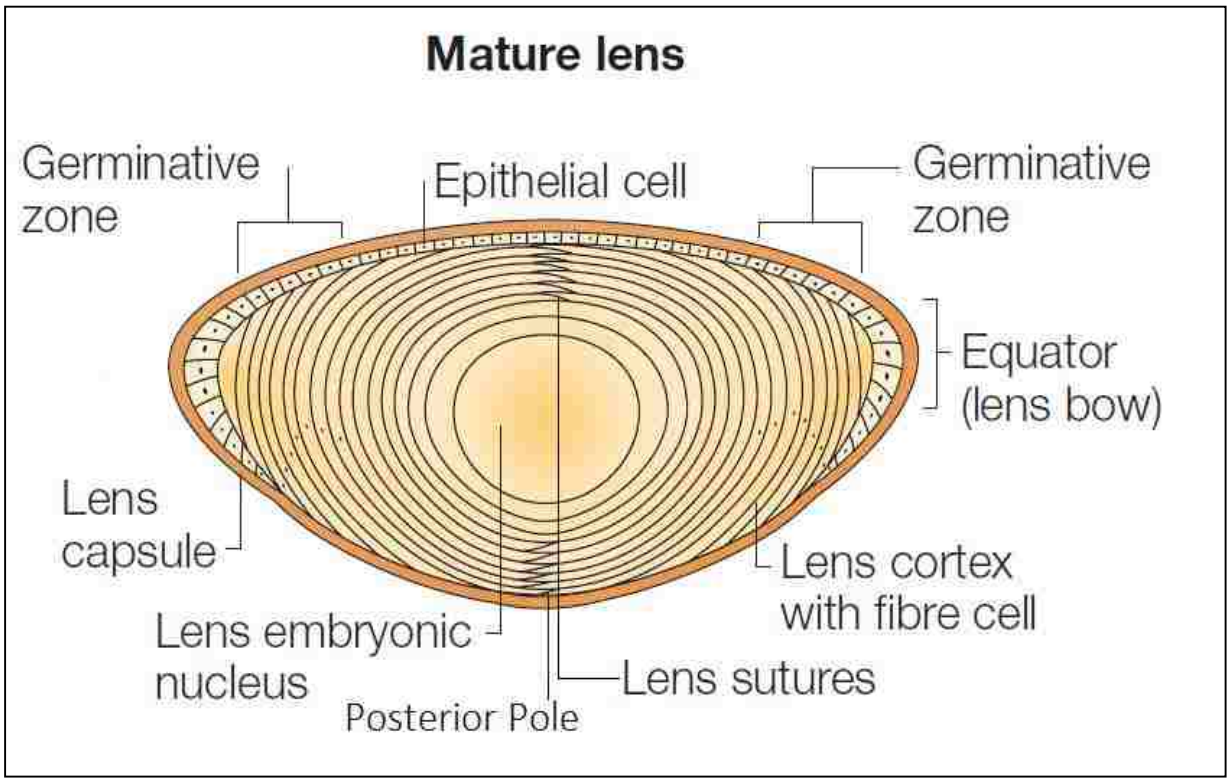

Figure 1.5: Detail of distinct regions of mature human lens. Adapted from (Graw, 2003).

Human lens epithelial cells are cuboidal or cylindrical in shape (Figure 1.6) and their size varies amongst individuals. Brown and Bron (1987) reported that 97% of the cells they measured had diameters from 9 to 17 µm. There is also a difference in size between cells grown in culture and cells *in vivo*. Lens epithelial cells grown in culture have an average diameter of about 30 µm (Cooper et al., 1990; Stewart et al., 1988). Cells *in vivo* have an average diameter from 12 or 13 µm (Brown & Bron, 1987; Masters

et al., 1997; Stewart et al., 1988) to 15 µm (Yanoff et al., 2009). Thickness estimates for lens epithelial cells range from 5 µm (Records, 1979) to 10 µm (Yanoff et al., 2009).

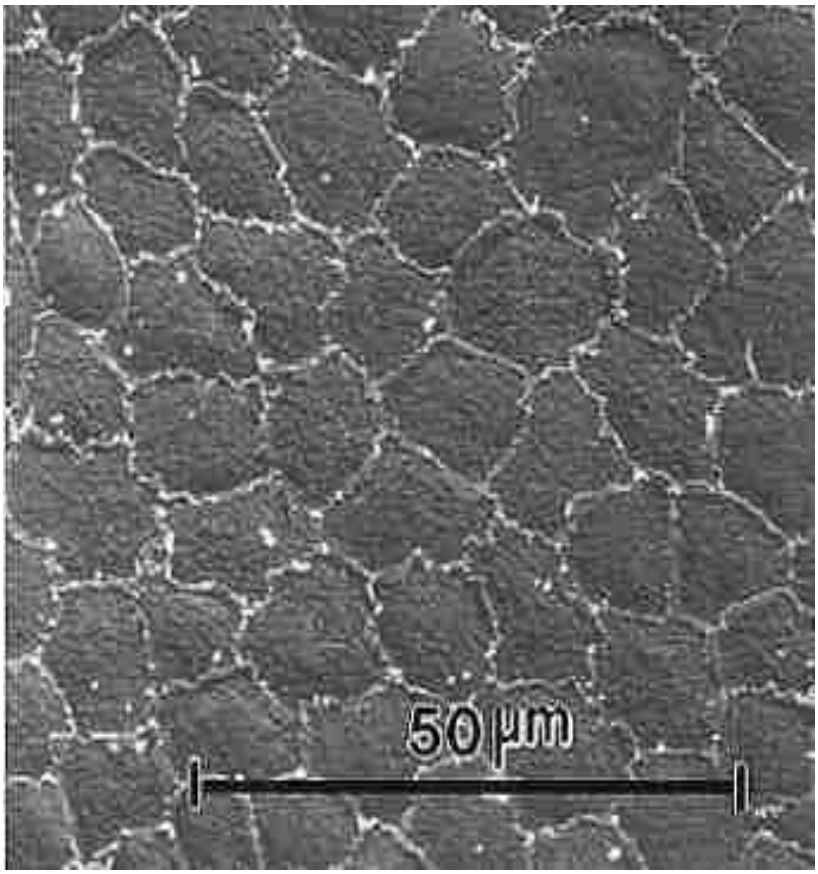

Figure 1.6: Scanning electron microscope micrograph of human lens epithelial cell layer. Adapted from (Masters et al., 1997).

1.4.2 Heart Endothelial Cell

Endothelial cells line all the blood vessels within the human body and form the interface between tissues and blood (Feng et al., 1999). Radiation damage to endothelial cells is a primary cause of secondary cardiac toxicities following radiation exposure (Baker et al., 2011; Yusuf et al., 2011). It is difficult to model endothelial cells because they elongate in response to fluid shear stress from blood flow, as seen in Figure 1.7

(Malek & Izumo, 1996; Sumagin et al., 2008). When endothelial cells are grown in culture they form a circular, randomly oriented cobblestone pattern (Malek & Izumo, 1996, Potter et al., 2012). *In vivo* endothelial cells are fusiform, or spindle shaped, and aligned in the direction of flow (Malek & Izumo, 1996) as seen in Figure 1.8, with an elongation ratio of about 2:1 (Potter et al., 2012). There is additional variability in cell size depending on location within the heart, and the size of the vessel in which the cell resides (Sumagin et al., 2008).

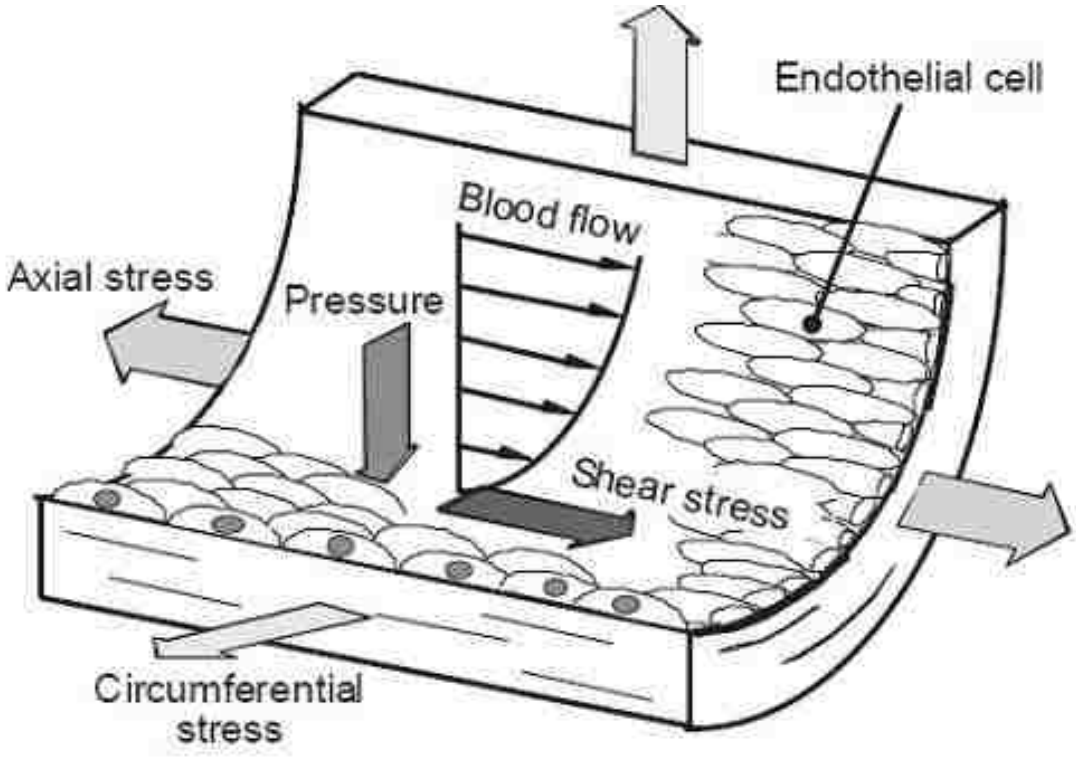

Figure 1.7: Endothelial cells lining a blood vessel. The cells are elongated in the direction of blood flow and shear stress (Ohashi & Sato, 2005).

There is not much quantitative information in the literature about the size of endothelial cells in the human heart. Much of the research has been performed on non-

human subjects such as rabbits and mice. To find a representative measurement, cell dimensions were acquired from multiple sources and an average size was determined. ATCC (http://atcc.org), a biological resource center and cell-line provider, quoted an average diameter of 20.7 µm for endothelial cells from a human aorta, 18.0 µm diameter for bovine heart endothelial cells, and 16.9 µm diameter for a bovine pulmonary artery endothelial cell (personal communication, July 17, 2013). Other sources showed a wide range of dimensions within the vasculature, ranging from 10 to 80 µm (McGeachie, 1998; Thiriet, 2007). Iliac artery endothelial cells were found to have an average length of 25.8 µm and an average width of 13.2 µm (Garipcan et al., 2011). The cell thickness was measured as 2.2 µm for *in vitro* cells and 1.2 for *in vivo* cells (Ohashi & Sato, 2005).

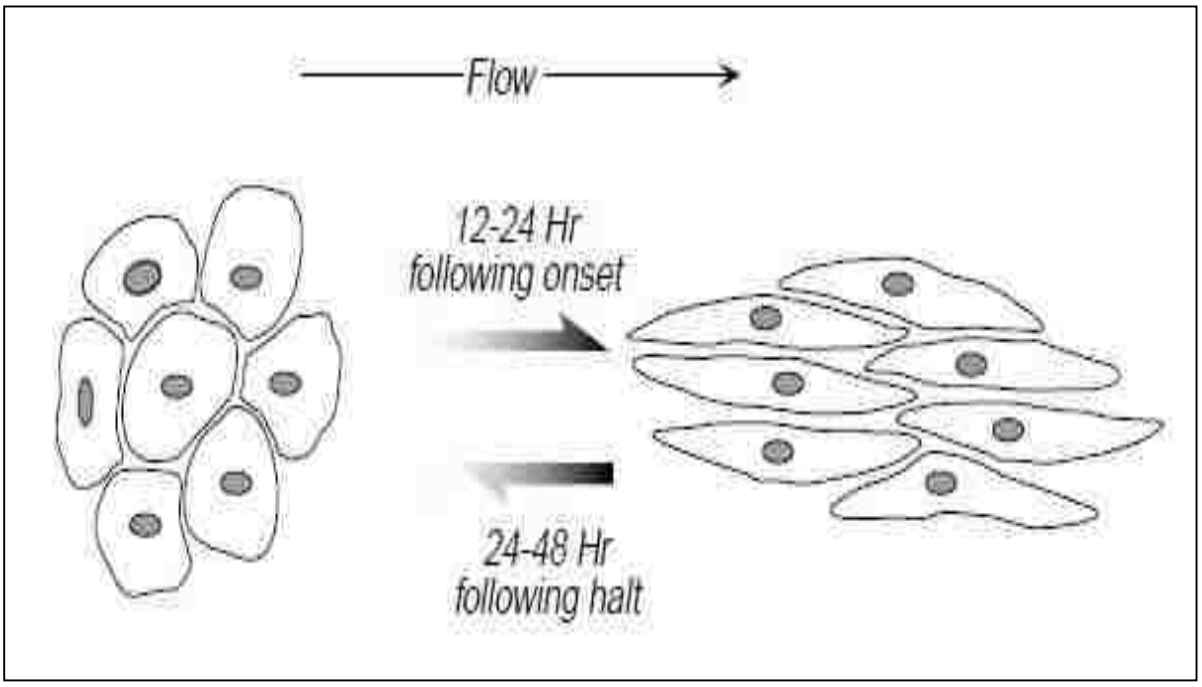

Figure 1.8: Schematic of endothelial cells' morphological response to flow and shear stress (Malek & Izumo, 1996). Endothelial cells in vitro maintain a circular, cobblestone pattern, whereas in vitro cells will elongate in the direction of blood flow.

1.4.3 Description of UOW Design

Collaborating on the MIDN project is the Centre for Medical Radiation Physics at UOW in Australia. To allow a direct comparison between LSU's detector and UOW's, the SVs in one of the arrays was identical to UOW's design of a cylinder 14.9 µm in diameter. Comparing detector responses based on the same SV helped to ensure proper calibration and that no defects occurred during construction of the devices.

1.5 New Detector Arrays

The chips were manufactured at the Nanoscale Research Facility at the University of Florida. The SV dimensions which were originally proposed had to be modified slightly to accommodate manufacturing constraints and a required amount of spacing, or pitch, between adjacent SVs. Table 1.2 lists the final dimensions and Figure 1.9 shows a depiction of the final array designs.

Table 1.2: Final SV dimensions.

Array Design	Shape	Dimensions (µm)	h (µm)
Lens Epithelial Cell	Cylinder	Diameter: 12.6	10
Heart Endothelial Cell *in vitro*	Cylinder	Diameter: 18.0	10
Heart Endothelial Cell *in vivo*	Ellipse	Major Axis: 24 Minor Axis: 12	10
UOW Design	Cylinder	Diameter: 14.6	10

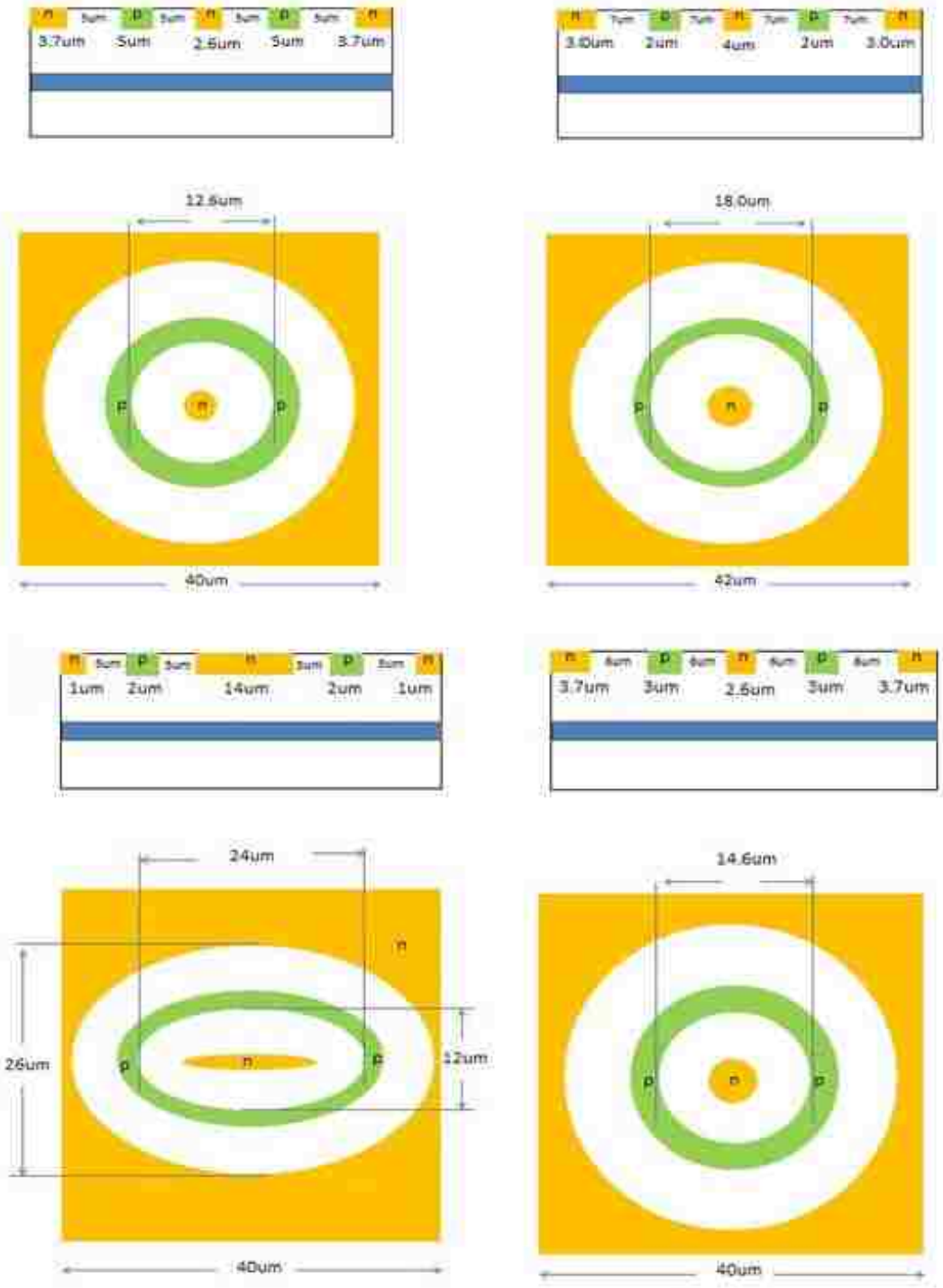

Figure 1.9: Final sensitive volume designs. Clockwise from upper left: Lens epithelial cell, heart endothelial cell in vitro, UOW cylinder, heart endothelial cell in vivo. (B. Gila, personal communication, August 26, 2013)

Due to miscommunications during the manufacturing process, the pin-outs for the n+ core and the p+ ring were switched. Instead of fabricating new chips, the decision was made to rewire the original chips. Unfortunately, some wires had to be crossed above the chip surface to achieve the desired wiring scheme (Figure 1.10). This is non-ideal because the wires can potentially shield some of the sensitive volumes, and the possibility exists of the wires sagging and shorting out, which would make the array non-functioning.

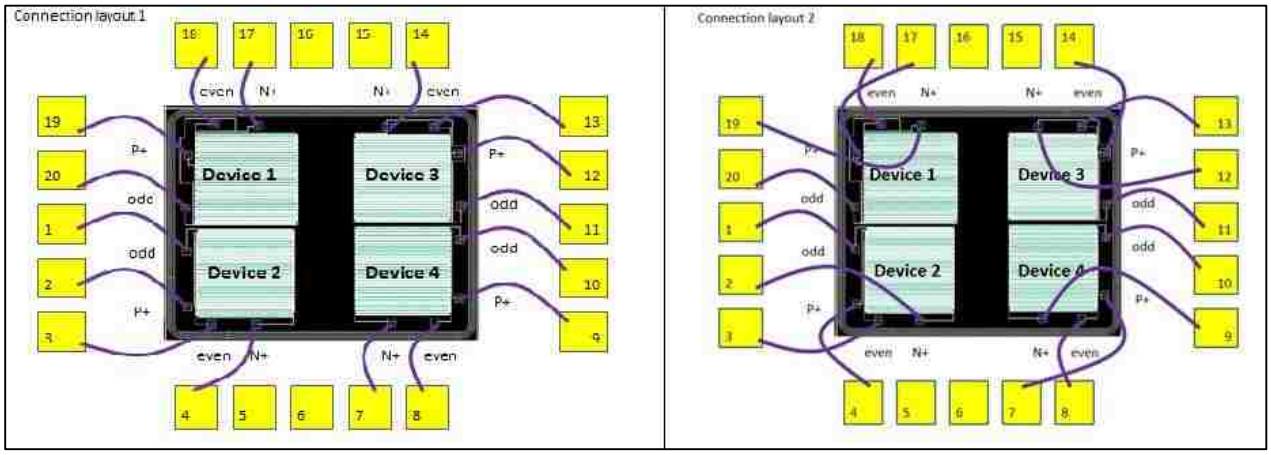

Figure 1.10: Revised pin-out configuration. Left: original wiring; Right: re-wired configuration.

1.6 qMIDN Device

The qMIDN device contains readout electronics for four independent microdosimeter devices. However, for this project, only one microdosimeter device was used at a time, and the output split to multiple gain settings to accommodate a wide range of lineal energy events. The arrays on the chip are selected for readout by placement of a jumper across the various junctions, J1 through J5 (Figure 1.11); note that the chips used in this project have only four arrays and J3 was not used. The junction J6 must be

bridged in order to acquire signal from the microdosimeter. Junction J7 is bridged when a test-input from a reference tail pulse generator is to be used.

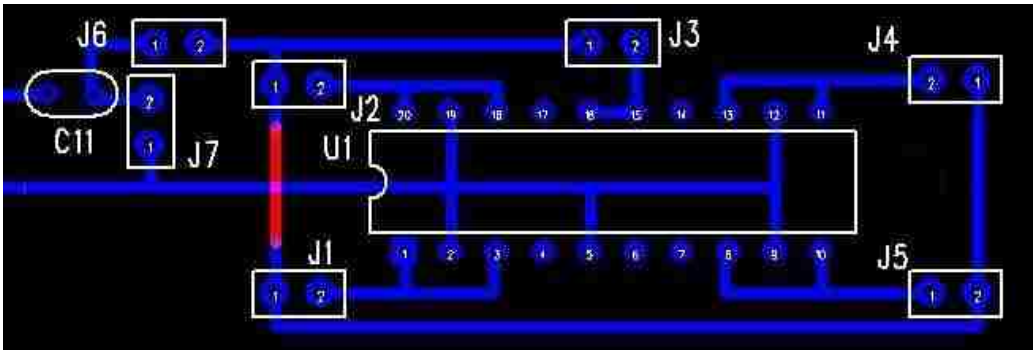

Figure 1.11: Placement of jumpers to select arrays. J1 selects the 12.5 µm cylinder array, J2 selects the 18 µm cylinder array, J3 not used, J4 selects the 14.5 µm cylinder array, J5 selects the 24 µm x 12 µm ellipse array (Ziegler, 2013).

Charge collected from the microdosimeter was capacitively coupled to an Amptek A250f charge-sensitive preamplifier, which has a fixed gain of 20 dB, and converted the incoming charge into a voltage pulse. This voltage pulse is then sent to an AD829 amplifier for inversion and pulse-shaping. The output of the amplifier is then sent to the qMorpho (Bridgeport Instruments, LLC, Austin, TX) device (Figure 1.12).

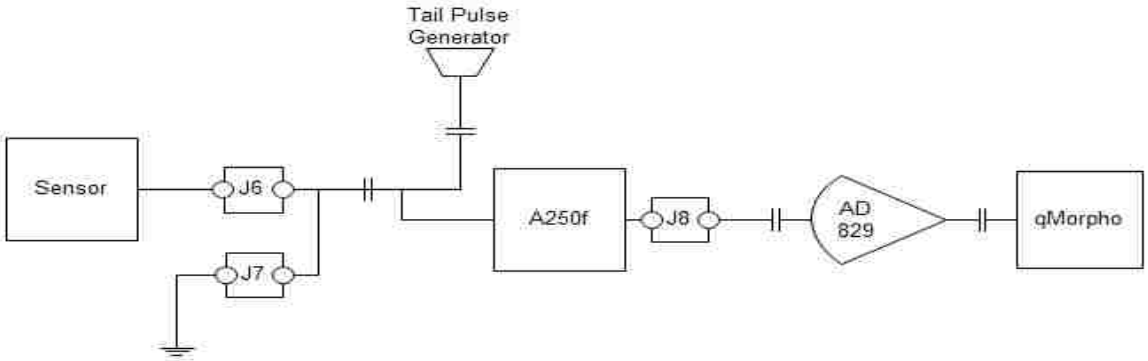

Figure 1.12: Simplified circuit diagram of signal collection and shaping components.

The qMorpho contains four multichannel analyzers (MCA) for pulse height analysis. The four MCAs are independent, though they share a common control and

command module. The signal in each MCA was first sent through a differential output OP-amp, where the gain was set by varying the transimpedance value (selected via the qMIDN software). The signal then encountered a waveform-digitizing analog-to-digital converter (ADC). The next step is the signal processing field-programmable gate array (FPGA) which analyzes the digitized signal and produces data which is picked up by the command and control FPGA. The experimental data was saved to a file on the attached laptop (connected via USB), which was read by the qMIDN software. The overall setup can be seen in Figure 1.13.

Power was supplied to the qMIDN via two 9V batteries inside the box, or by an external DC power supply with the wires run into the box. Use of the batteries has the advantage of fewer wires and flexibility in physical placement of the device, especially if the optional Wi-Fi capability is utilized. Using the external power supply is advantageous when long acquisition times are required, as the batteries become depleted in a relatively short amount of time.

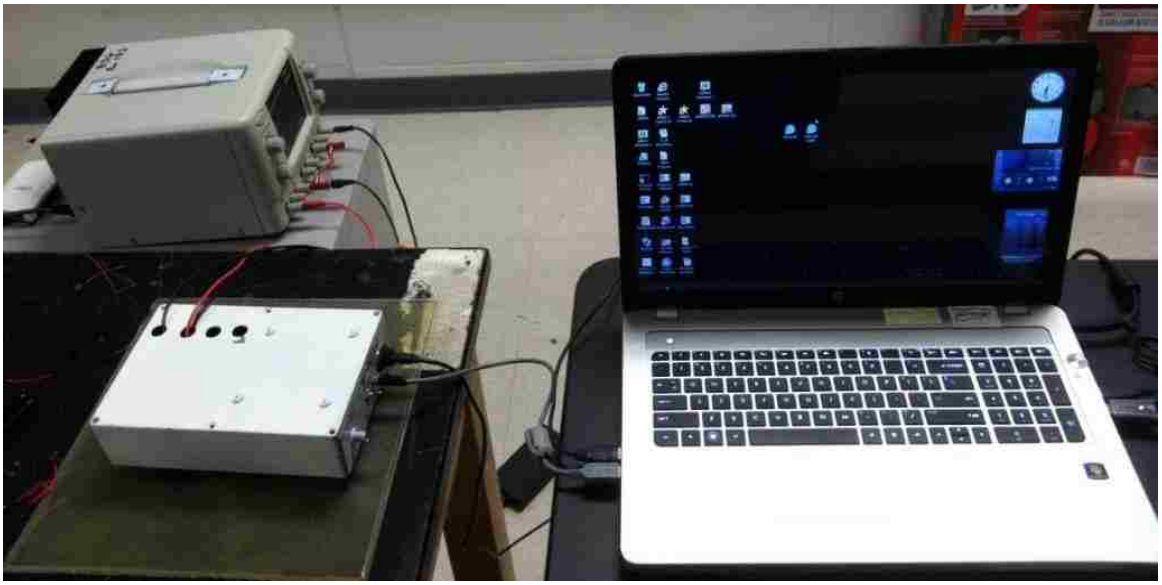

Figure 1.13: Overall layout of qMIDN experimental setup: DC power supply, qMIDN device, and laptop with control software.

1.7 Hypothesis and Specific Aims

The purpose of this research is to test the feasibility of a SOI microdosimeter with SVs in the shape and size of human cells. The idea has been proposed previously (Bradley et al., 2001; Pisacane et al., 2013), but to our knowledge no such devices have previously been built and characterized.

Hypothesis: With a silicon on insulator microdosimeter, whose sensitive volume closely models the physical dimensions of human cells, dose equivalent from a ^{239}PuBe neutron source can be determined with uncertainty less than 10%.

Aim 1: Quantify the uncertainty in lineal energy introduced by the calibration procedure from ^{241}Am alpha particle irradiation.

Aim 2: Measure absorbed dose to silicon from moderated ^{239}PuBe irradiation and quantify uncertainty in absorbed dose to silicon.

Aim 3: Convert absorbed dose to silicon to absorbed dose to tissue and dose equivalent to tissue. Quantify uncertainty in dose equivalent to tissue from moderated ^{239}PuBe irradiation.

2 METHODS AND MATERIALS

2.1 Specific Aim 1 - Quantify the uncertainty in lineal energy introduced by the calibration procedure from ^{241}Am alpha particle irradiation

2.1.1 Acquiring Alpha Particle Spectra and Converting to Microdosimetric Format

For the purposes of characterizing the response of the detector to charged particle irradiation and to calibrate the device to lineal energy and absorbed dose, studies were conducted using ^{241}Am sources, which decay by emission of alpha particles: 5.476 MeV (84.4%) and 5.433 MeV (13.6%). Two sources were utilized: a 0.1 μCi NIST-traceable source (Source 1), and a 0.65 μCi source (Source 2). Source 1 was the preferred source, owing to its NIST-traceability, but when it was unavailable for testing, Source 2 was utilized. Since the energies of the alpha particles emitted by Source 2 were not known accurately a priori, spectra were acquired with both sources using previously calibrated detectors. From this information, and the known energies of the alpha particles from Source 1, the energies of the alpha particles from Source 2 were determined. This knowledge of the sources' energy distribution was important to ensure proper calibration when using either source.

Figure 2.1 shows the differences in the energy spectra between the two ^{241}Am sources. These spectra were acquired in a vacuum chamber using silicon strip detectors in Dr. Jeff Blackmon's laboratory. As can be seen, Source 1 emits essentially mono-energetic alpha particles, whereas Source 2 has a much broader energy spectrum. This information was used to determine the average energy of the emitted alpha particles and to verify the activity of the Source 2. Note that the detectors used in this experiment were relatively thick (1 mm) so that all the alpha particles stopped and deposited all of their energy within the detector. Thus, alpha particles of higher energy will register at a higher

channel numbers; as opposed to the situation where all of the alpha particles were "crossers," and those possessing a higher energy would deposit less energy within the detector and would register at a lower channel number.

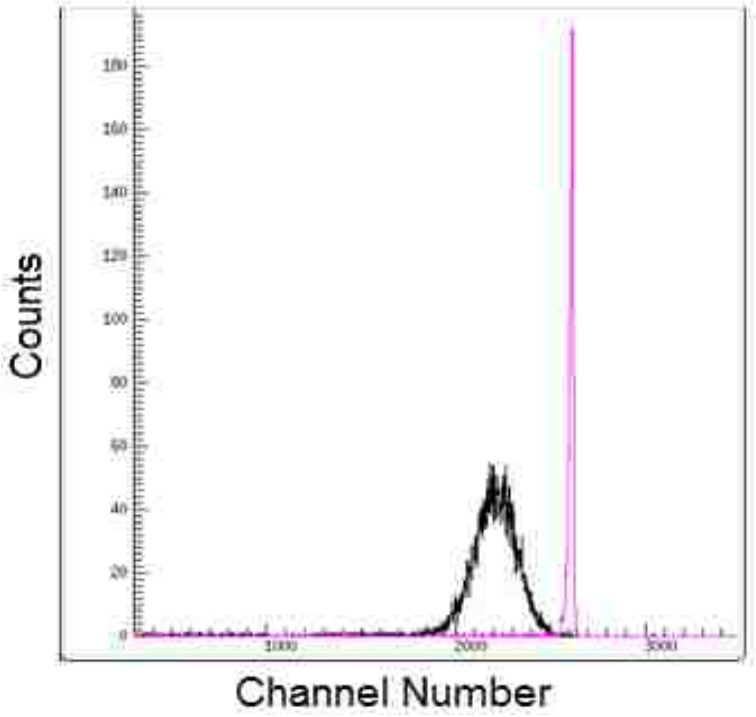

Figure 2.1: Comparison of energy spectra from the two ^{241}Am sources used in this work, in terms of counts versus channel number. Pink: Source 1, Black: Source 2. Spectra were acquired under vacuum using thick silicon strip detectors.

Bias voltage was supplied to the microdosimeters by connecting to the 6 V power supply for the circuit board. An inline potentiometer allowed for the application of varying amounts of bias voltage, up to 6 V maximum. As evidenced by the testing done by UOW with the same chips (Tran & Chartier, 2014), 6 V was sufficient to achieve full depletion of the sensitive volumes and to maximize charge collection efficiency. Acquiring spectra with increasing amounts of bias voltage shifted the position of alpha peak to higher channel numbers, since as the charge collection efficiency of the device improved (due to reduced recombination effects), the size of the pulses being recorded also increased.

This effect is demonstrated by Figure 2.2 and the corresponding peak position values shown in Table 2.1.

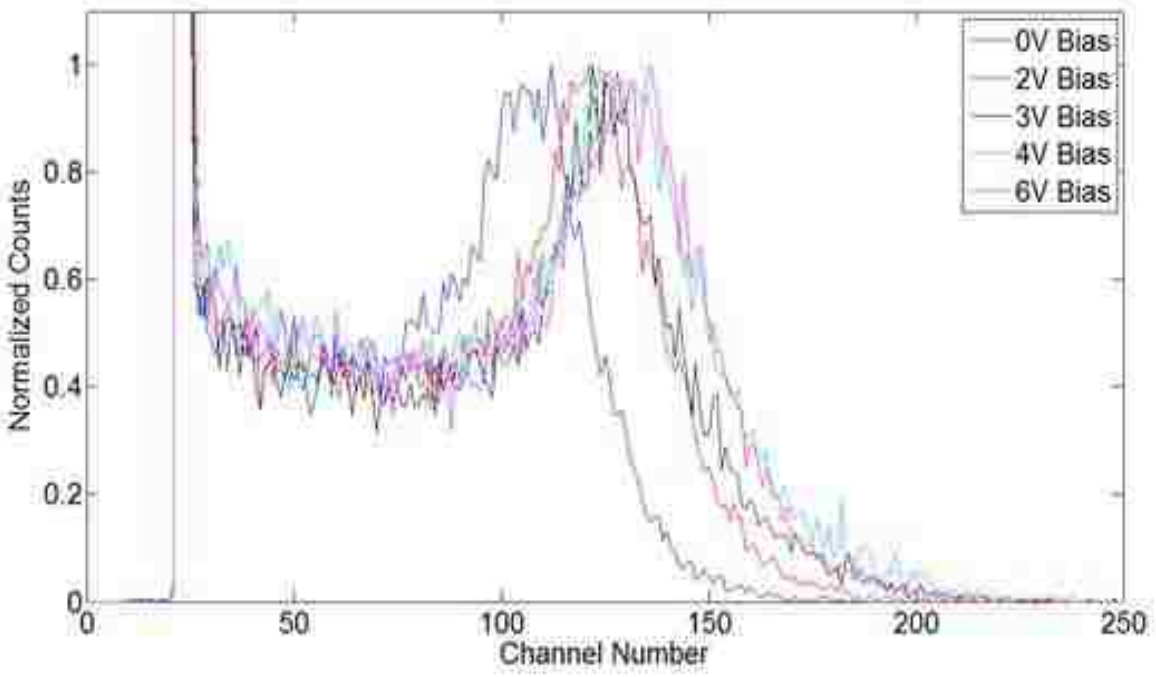

Figure 2.2: Shift in alpha peak position based upon the amount of bias voltage applied.

Table 2.1: Alpha peak channel numbers based on increasing amounts of bias voltage; 18 µm cylinder array.

Reverse Bias Voltage (V)	Position of Peak (Channel #)
0	107
2	122
3	125
4	129
6	130

A Matlab code was developed for this work to analyze the raw data from the multi-channel analyzers and convert them into the microdosimetric format. The code allows

for plotting the data in various forms: counts vs. channel number, counts vs. energy deposited, y•d(y) vs. y, etc. To convert channel number to energy deposited, the code combines data from an alpha particle calibration with information from the pulse generator calibration (described in more detail later). From a spectrum acquired with one of the ^{241}Am sources, the code extracts the position of the alpha particle peak by fitting a Gaussian curve to the peak region. The fitting is done in two steps. The first fit, which is performed over a user-selected region of the data, is used to find the centroid position and the sigma width parameter of the Gaussian curve. The second fit is performed over a region defined by the centroid from the first fit, plus and minus one sigma.

The amount of energy deposited in the SV represented by counts under the alpha peak is then calculated by the energy loss codes, taking into account the energy lost by the alpha particles while traveling through the air gap and SiO_2 layer atop the device. The energy deposition spectrum is then converted to lineal energy by dividing the energy deposited by the mean chord-length of the SV that was used. For final plotting of the data, the code follows the International Commission on Radiation Units and Measurements (ICRU) Report 36 (1983) recommendations of binning the data for graphical presentation.

2.1.2 Compare Observed Versus Expected Count Rates

To compare observed and expected count rates, the active diameter of the ^{241}Am source was determined. To assay the source, a collimator was constructed from a 3.2 mm (1/8”) thick copper sheet with a 1.6 mm (1/16”) hole drilled through it. This collimator was scanned over the surface of the source laterally and longitudinally in one millimeter steps, and the fluence measured at each position using a survey meter (Model 14C, Ludlum Measurements, Inc., Sweetwater, Texas) and a Ludlum Model 44-9 alpha, beta,

gamma “pancake” Geiger-Mueller detector. This value will also be important for the chord length and energy deposition Monte Carlo simulations.

Comparisons were made between the expected number of counts, based on the source activity and source-to-surface distance (SSD), and the observed number of counts, extracted from the experimental data. The expected number of counts was found by using the equation for fluence rate at a distance d from a disc source of radius r and activity A, or

$$\dot{\phi} = \frac{A}{4\pi r^2} ln(\frac{r^2+d^2}{d^2}). \quad (2.1)$$

Multiplying the fluence rate by size of the active area of the array gives the expected number of particles interacting with the detector per unit time. Assuming 100% collection efficiency, this gives the expected count rate. The observed number of counts will be determined from analyzing experimental spectra acquired with the microdosimeters.

2.1.3 Alpha Particle Monte Carlo Simulations

Since the alpha particle sources used were relatively large disc sources compared to the much smaller SVs (Figure 2.3), alpha particles traversed the SVs through many different chord lengths. The chord length the particle traversed through the SV directly affected the amount of energy deposited in the SV and consequently the shape of the recorded spectrum. It is therefore important to know and understand the shape of this chord length distribution.

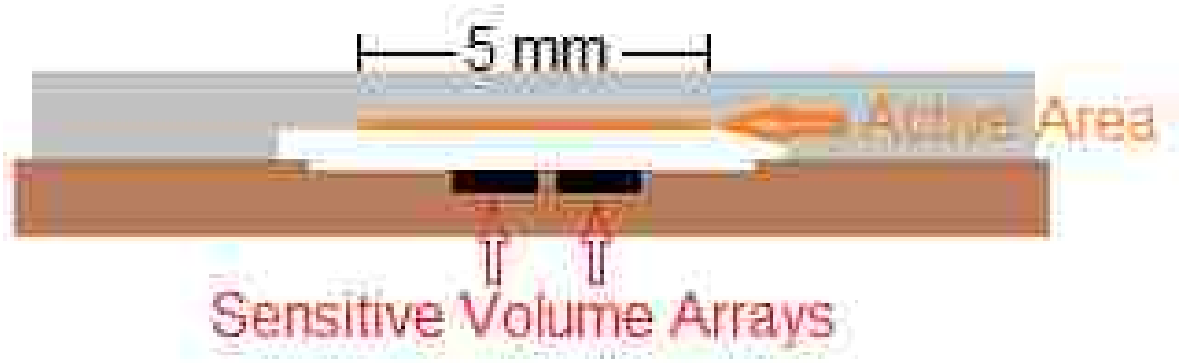

Figure 2.3: Schematic representation of ^{241}Am source atop the microdosimeter; side view.

To this end, a Monte Carlo (MC) simulation code was written for this project to simulate the experimental setup and to find the chord length and energy deposition distributions for each of the four SVs. The code was written in Matlab. The user-specified source and detector geometry (source dimensions, source energy spectrum, SSD, SV dimensions) and the number of particle histories. The simulation began by randomly selecting the alpha particle origin on the surface of the source. From this origin, the three-dimensional direction of the particle was randomly sampled (isotropic emission). If the particle's trajectory did not interact with any of the SVs, the history was ignored, but if the particle hit one of the SVs, the distance the particle traveled through the layers of air and SiO_2, and the chord length through the SV were recorded.

There are four categories of SV hits for "crosser" particles (Figure 2.4): 1. The particle enters through the top of the SV and exits through the bottom of the SV. 2. The particle enters through the top of the SV but exits through the side of the SV. 3. The particle enters through the side of the SV and exits through the bottom of the SV. 4. The particle enters through the side of the SV and exits through the other side of the SV.

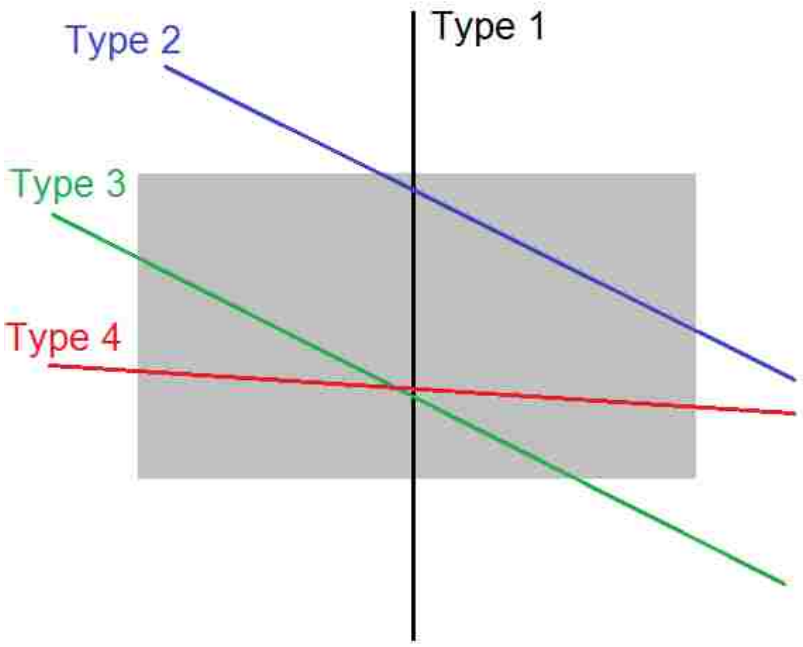

Figure 2.4: The four categories of crosser type particle chord lengths.

If the essentially monoenergetic Source 1 was being simulated, all the particles were assigned 5.486 MeV. If Source 2 was used, an energy was randomly sampled from the source's cumulative distribution function (CDF) (seen in Figure 2.5), which was calculated from the spectrum of alpha particle energies that the source emits due to self-absorption. The CDF, F(x), was generated such that a random number, ε, was sampled from a distribution, f(x), determined by the energy spectrum, or

$$F(x) = \int_{-\infty}^{x} f(x)dx. \tag{2.2}$$

In practice, a random number, γ, between 0 and 1 was generated and then the following equation is solved for ε (Dunn & Shultis, 2011):

$$\gamma = F(\varepsilon). \tag{2.3}$$

Figure 2.6 shows the energy spectrum from Source 2 as measured experimentally, and as modeled in the MC simulations.

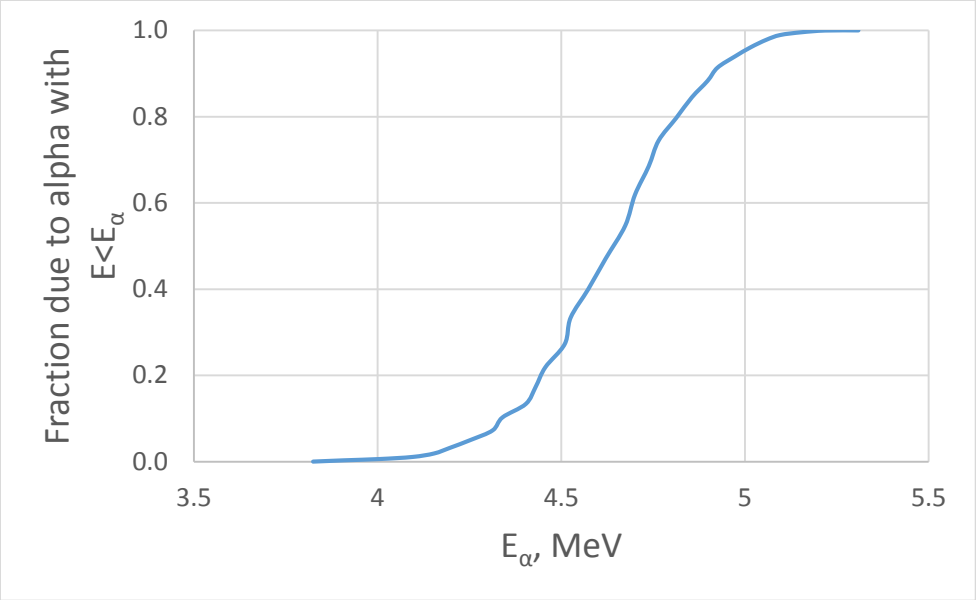

Figure 2.5: Cumulative distribution function calculated from Source 2 alpha particle energy spectrum.

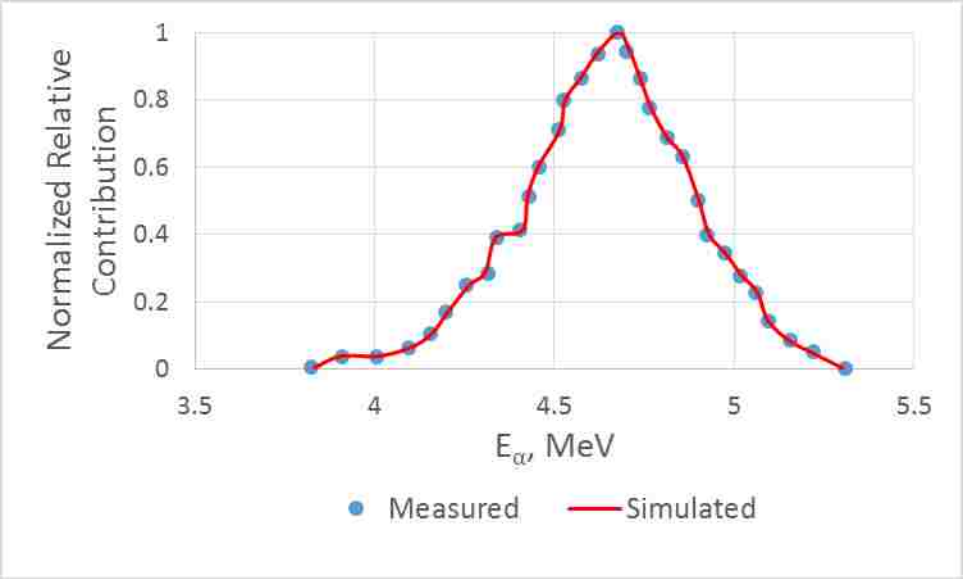

Figure 2.6: Energy spectrum of alpha particles emitted from Source 2 as measured and as modeled by simulation.

Based on the energy of each particle and the recorded distances traversed through each material, the amount of energy lost in the each layer was calculated using NIST ASTAR (http://physics.nist.gov/PhysRefData/Star/Text/ASTAR.html) stopping power and

range data. This process was repeated for each subsequent history, and the results tabulated into an energy deposition spectrum. The program additionally displayed the chord length distribution (total or broken down into crosser category), and y•d(y) spectrum.

2.1.4 Calibration Procedure

The calibration procedure was based on a standard pulse height calibration method, which relied on both an alpha particle calibration and a reference tail pulse generator (TPG) calibration. First, the microdosimeter is irradiated with an ^{241}Am source, of known energy, to acquire a pulse height distribution (Figure 2.7). Then using the Gaussian fitting procedure described in Section 2.1.1, the channel number of the alpha peak is found. From MC simulations of the calibration setup, it is known that the peak of the pulse height distribution represents alpha particles traveling predominantly through the 10 µm thickness of the SV; demonstrated by the sharp peak in the simulated chord length distribution seen in Figure 2.8.

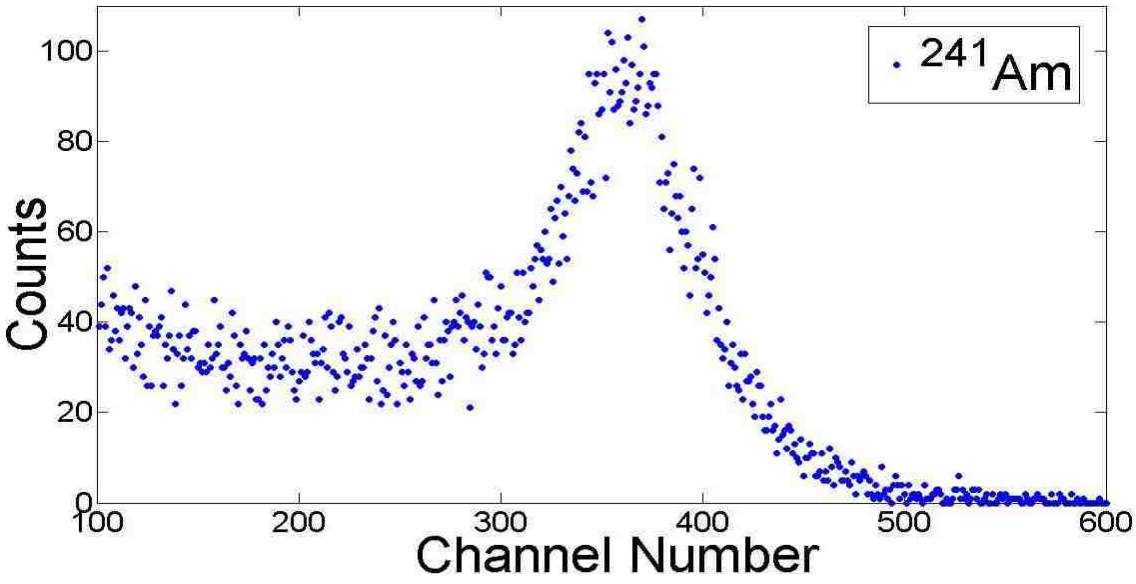

Figure 2.7: Pulse height distribution acquired with microdosimeter from ^{241}Am source.

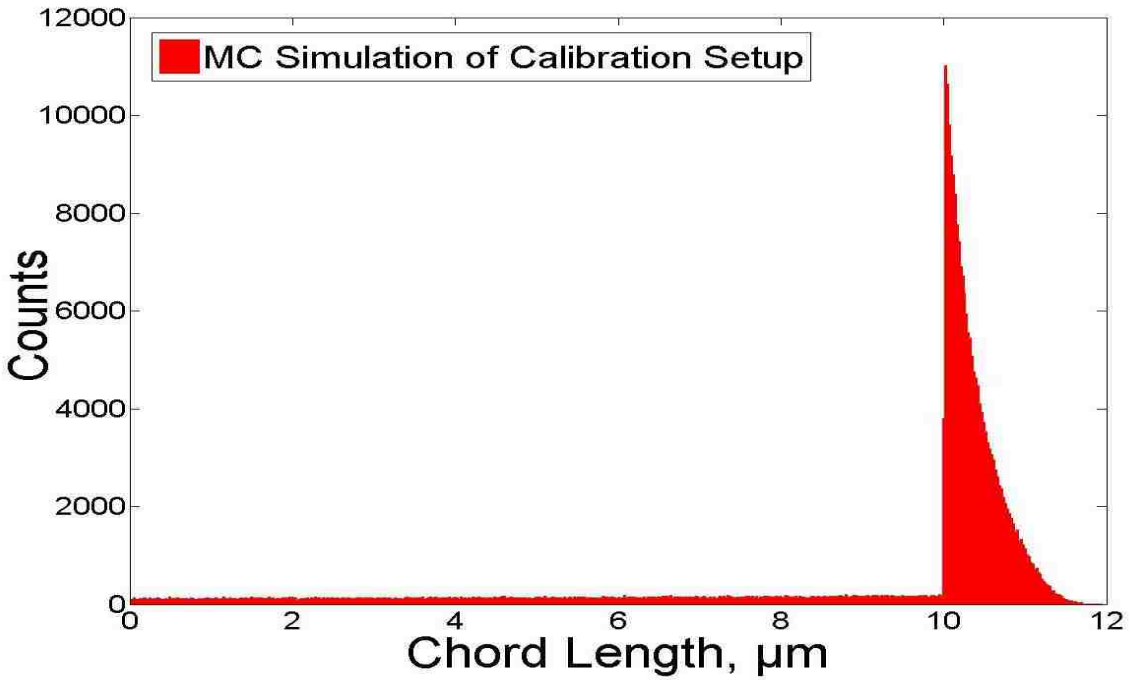

Figure 2.8: Simulated chord length distribution representative of the ^{241}Am calibration setup.

The expected energy deposition, $\bar{\varepsilon}_{ref}$, is then calculated using ASTAR stopping power data:

$$\bar{\varepsilon}_{ref} = \left(\frac{d\bar{E}}{\rho dx}\Delta\bar{x}\right) \tag{2.4}$$

where $\frac{d\bar{E}}{\rho dx}$ is the mass stopping power value for the mean energy of the alpha particle source, and $\Delta\bar{x}$ is the 10 μm thickness of the SV. The expected lineal energy, $\bar{y}_{ref}$, is then calculated by:

$$\bar{y}_{ref} = \frac{\bar{\varepsilon}_{ref}}{\bar{l}}. \tag{2.5}$$

At this point, a channel to energy conversion has been determined for only one particular channel. To extend the calibration to all possible channels the linearity of the detector response must be determined for the remaining channels. To do this, the TPG is used to input a series of test signals of varying amplitudes into the device electronics.

The amplitude of the test pulse was increased until the peak falls into approximately the maximum channel number (900) at the lowest gain setting. Using the bank of attenuator switches (2X, 5X, 10X, etc.), the amplitude of the pulse is then sequentially reduced and the new position of the peak noted for each attenuation setting. Ideally, the reduction in peak position will exactly match the attenuation value used. For example, using a 2X attenuator on a peak that resides in channel 900 should result in the peak now residing in channel 450. This process is repeated for each of the gain settings to generate a plot of pulse height versus channel number.

Following the same method as Newhauser (1995), a linear regression between the pulse height versus channel number data points is performed (Figure 2.9) to determine the slope, m, and y-intercept, b, such that a reference pulse height can be defined by the linear function:

$$P_{ref} = mh_{ref} + b. \tag{2.6}$$

where h_{ref} is the channel of the alpha particle peak found from the Gaussian fitting procedure.

Combining this integral linearity data with the alpha calibration data allows for defining a linear function for lineal energy in terms of channel number, h:

$$y(h) = \alpha + \beta h \tag{2.7}$$

where α and β are defined as follows:

$$\alpha = \frac{y_{ref}}{P_{ref}} b \tag{2.8}$$

$$\beta = \frac{y_{ref}}{P_{ref}} m. \tag{2.9}$$

For further explanation, a sample calibration worksheet can be found in the Appendix (Figure 6.2).

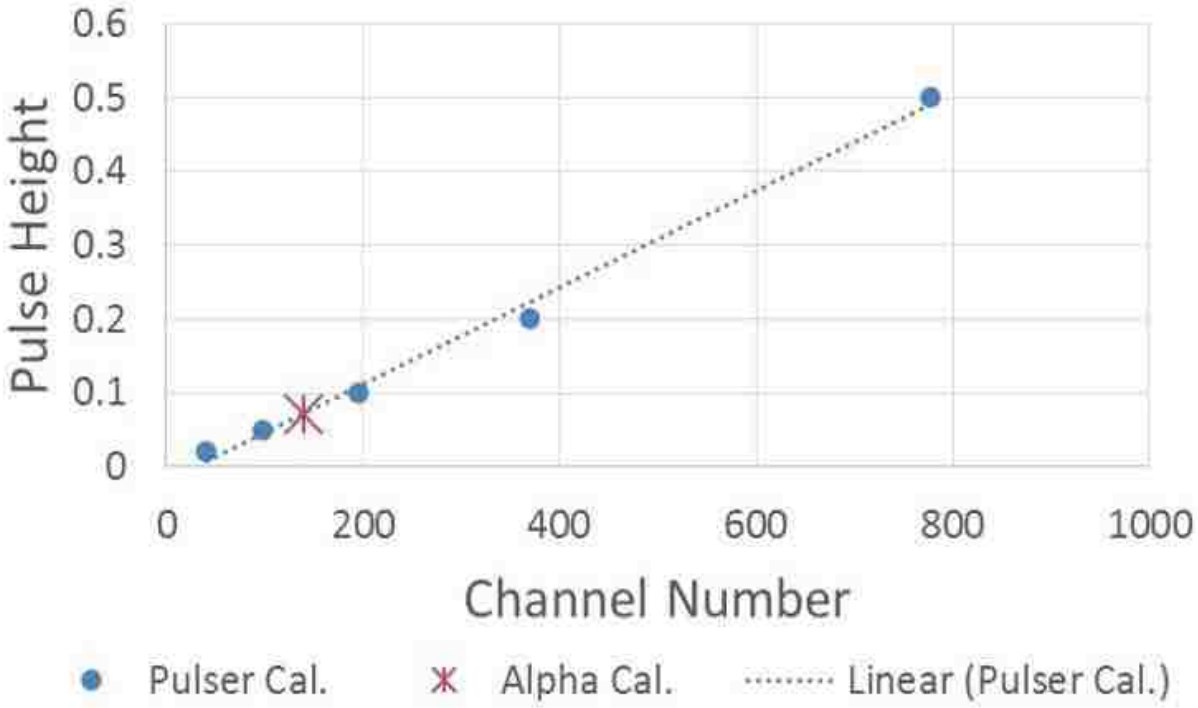

Figure 2.9: Plot of pulse height versus channel number generated with the reference tail pulse generator. Also shown are the results of the alpha calibration and the linear regression between the pulser calibration data points.

In addition to the integral linearity of the device, the response of the device in terms of differential linearity was analyzed using the TPG's built-in ramp generator function, which steadily increases the output of the pulse over a set period of time. The ideal result of which would be a steady output across all channel numbers. As seen in Figure 2.10, the device showed a linear response across the range of channels, aside from the noise peak evident in the lower channels.

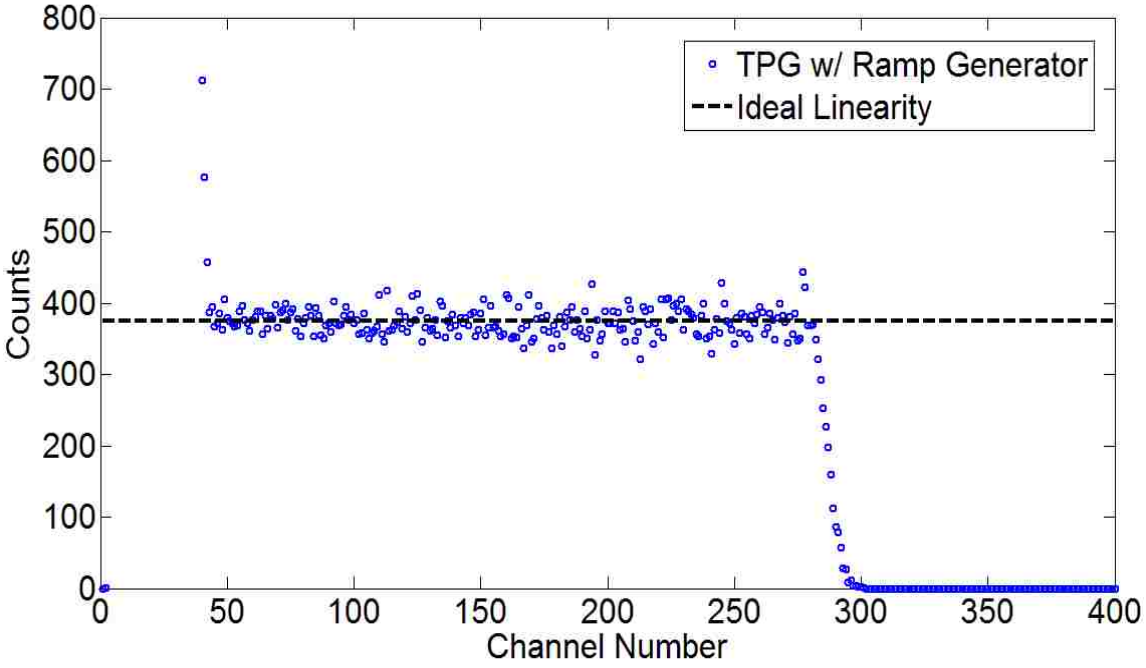

Figure 2.10: Testing the differential linearity of the device electronics.

2.2 Specific Aim 2 - Measure absorbed dose to silicon from moderated ^{239}PuBe irradiation and quantify uncertainty in absorbed dose to silicon

2.2.1 Assessment of SOI Chip Surface Conditions

Twenty individual microdosimeters, each mounted in a 20 pin dual in-line package (DIP), arrived from the University of Florida. Four of these were sent to UOW for characterization and initial testing; leaving sixteen for use in this project. The first step in identifying which of the microdosimeters were best suited for further testing was to acquire images of the chip surfaces to determine if any damage had been done during the manufacturing and/or rewiring process, or in initial handling and testing. Microscopic images of each chip were taken and analyzed for evidence of surface defects or damaged wires. This information was used to assess the overall mechanical condition of the surface of each chip.

2.2.2 Leakage Current Measurements and Depletion Width Considerations

The basic diode characteristics of the microdosimeters were characterized. To this end, measurements of leakage current versus bias voltage were performed for each array. A perfect diode would transmit zero current under reverse bias conditions and infinite current under forward bias conditions, though, in reality, some small amount of leakage current flows through reverse-biased diodes. Figure 2.11 shows a representative curve typical of the relationship between bias voltage and leakage current for silicon semiconductor diodes. An extremely well-functioning silicon microdosimeter will exhibit leakage current on the order of picoamps at a reverse bias voltage of 5 V (Hu, 2013; Ziebell et al., 2008).

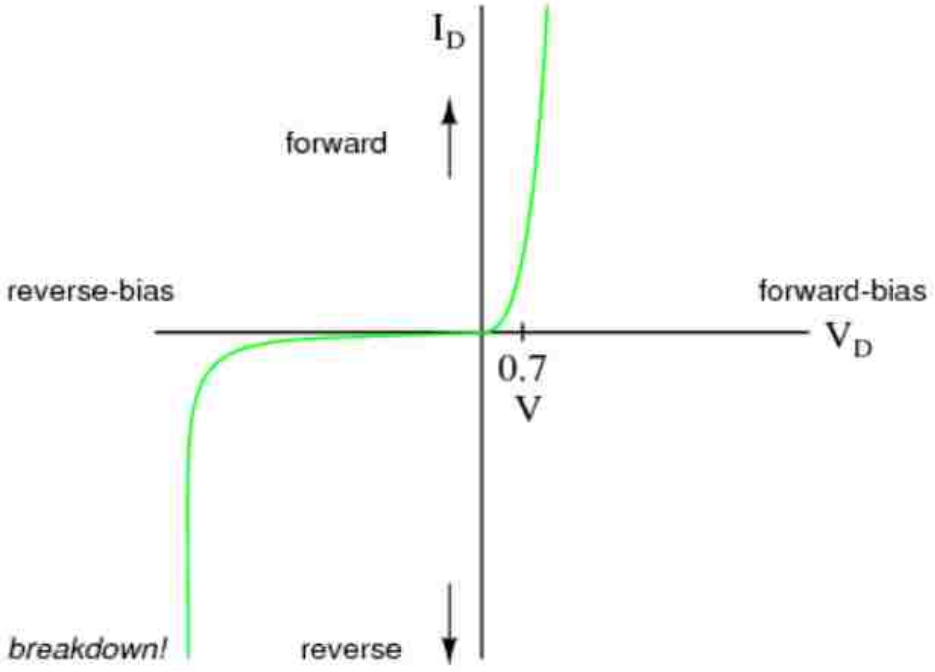

Figure 2.11: Typical silicon semiconductor diode curve (Hu, 2013).

Leakage current measurements were performed with the LSU and UOW microdosimeters in a light-tight box to eliminate any current from ambient light. Bias voltage was provided by an external DC power supply. Adding a 1 MΩ resistor in series

with the SV core and measuring the voltage across the resistor (taking the 10 MΩ input impedance of the meter itself into account) with a Mastech (Precision Mastech Enterprises Corporation, Hong Kong) digital multimeter allowed for calculation of the leakage current. Bias voltage was increased in 0.25 V steps and the leakage current calculated for each step, until the leakage current reached a value of 0.5 μA, which was chosen to keep down noise levels and to prevent any damage to the chips.

For an abrupt p-n junction (Figure 2.12), the width of the depletion region, w_d, is highly dependent on the amount of reverse bias voltage being applied to the junction and the doping concentrations of the n- and p- type layers, according to Equation 2.10 (Jaeger & Blalock, 2008):

$$w_d = \sqrt{\frac{2\varepsilon_s}{q}\left(\frac{1}{N_A} + \frac{1}{N_D}\right)(V_i + V_R)} \tag{2.10}$$

where ε_s is the dielectric permittivity of silicon, q is the charge of an electron, N_A and N_D are the acceptor and donor doping concentrations respectively, V_i is the inherent potential of the junction, and V_R is the applied reverse bias voltage. The inherent potential of the junction due to the doping concentrations, V_i, can be found from (Neudeck, 1989):

$$V_i = \frac{k\,T}{q} ln\left(\frac{N_A\,N_D}{n_i^2}\right) \tag{2.11}$$

where k is Boltzmann's constant, T is the temperature in Kelvin, and n_i is the intrinsic carrier density.

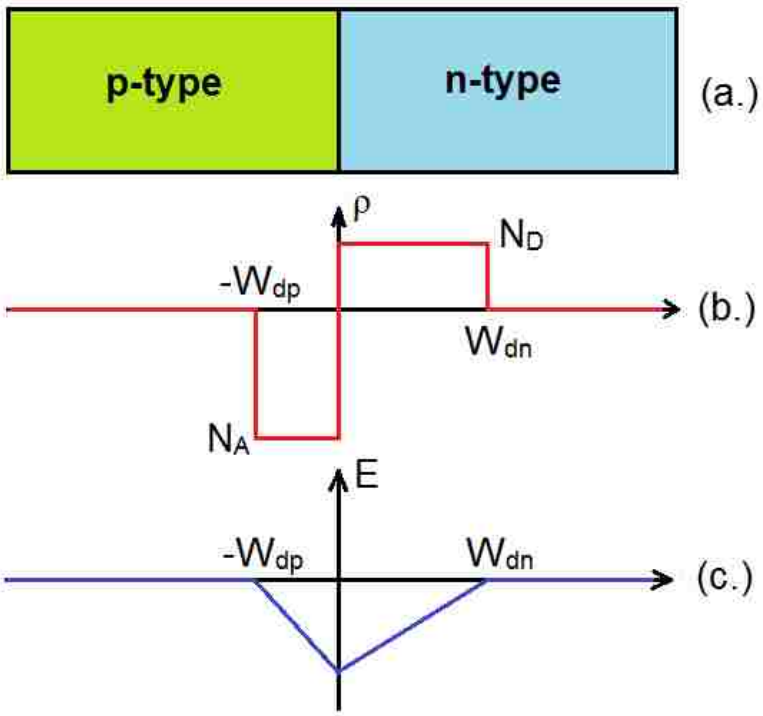

Figure 2.12: Diagram showing (a.) p-n junction, (b.) charge distribution, and (c.) electric field distribution in the depletion region. Adapted from (Ng, 2002).

The microdosimeters used in this project were not of the abrupt p-n junction type, but were constructed of p-i-n junctions (Figure 2.13), which have a layer of intrinsic, or un-doped, silicon between the n and p layers. These types of junctions are typically used when one wants to increase the width of the depletion region (Zeghbroeck, 2007). For a p-i-n junction, the width of the depletion region is found from (Zeghbroeck, 2007):

$$w_d = \sqrt{d^2 + \frac{2\,\varepsilon_s}{q}\frac{(N_A+N_D)}{N_A\,N_D}(V_i + V_R)} \tag{2.12}$$

where d is the width of the intrinsic silicon region. Since the doping concentrations used in the construction of the microdosimeters for this project were very high (p-type: 2 x 10^{20} $\frac{ions}{cm^3}$, n-type: 1 x 10^{19} $\frac{ions}{cm^3}$), the term on the right added very little to the d^2 term, which dominated the width of the depletion region.

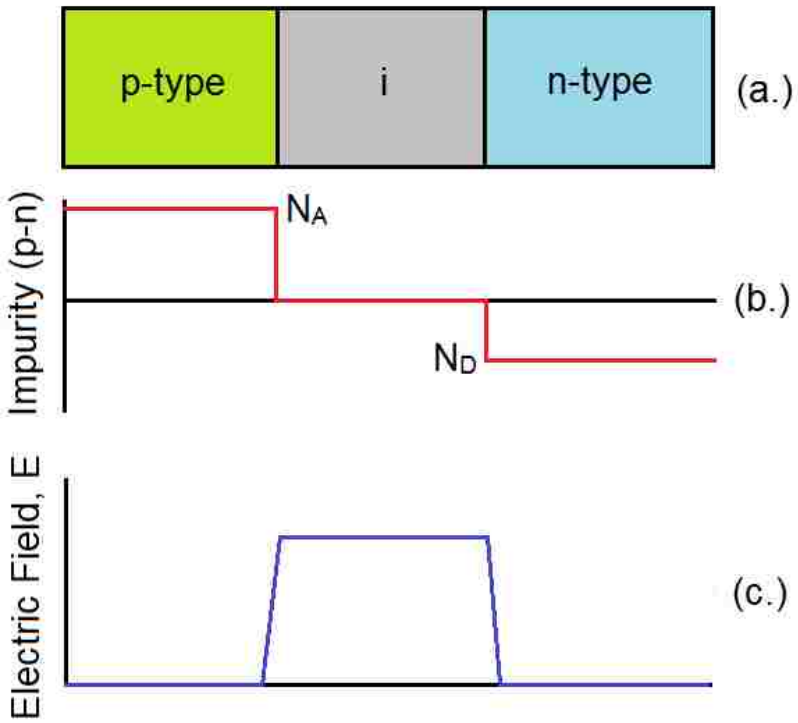

Figure 2.13: Diagram showing (a.) p-i-n junction, (b.) impurity profile, and (c.) electric field distribution. Adapted from (Ng, 2002).

2.2.3 Determining the Noise Threshold

Even when no radiation source is present, there is a certain amount of noise in the analog readout electronics, which produces a noise peak in the lower channels. This peak obscures any radiation-induced counts that may occur in those channels below the noise peak and thus increases the lower detectability limit of the device. The threshold level varied depending upon which chip was being used and the amount of bias voltage being applied.

To determine the extent of the noise, spectra were acquired with no radiation source present, using a selection of chips (chosen based upon minimum leakage currents) over a long period of time (24 to 48 hours). The chips that had the lowest leakage current and the lowest noise threshold were selected for further measurements.

2.2.4 Neutron Monte Carlo Simulations

Similar to the method described in Section 2.1.3, a MC code was written in Matlab to simulate the response of the device to neutron irradiation. The detector parameters remain the same as in the alpha particle code, but the source parameters were modified. Since the vast majority of detected events will be due to recoil protons or alpha particles produced in the converter layers, the converter was simulated in the code as a volume-source of particles.

The simulation began by randomly selecting x, y, and z coordinates within the volume encompassed by the source. Once the origin of the particle was defined, the particle's three-dimensional direction was then randomly selected. When simulating the boron converter, all alpha particles were assigned the same initial energy of 1.47 MeV (see Section 2.2.5. To define the initial energy of a proton from the tissue-substitute converter, first a neutron energy was randomly selected from the CDF (Figure 2.14), which was calculated from the neutron energy spectrum of the ^{239}PuBe source (Harvey, 2008), seen in Figure 2.15. This value represents the energy of a neutron emitted from the source which would have produced the recoil proton. Since recoil protons are produced in elastic, approximately hard-sphere collisions, the energy of the proton will be uniformly distributed from 0 up to the initial energy of the neutron. Thus, once the initial energy of the neutron is defined, the initial energy of the recoil proton is found by multiplying the neutron energy by a random number between 0 and 1.

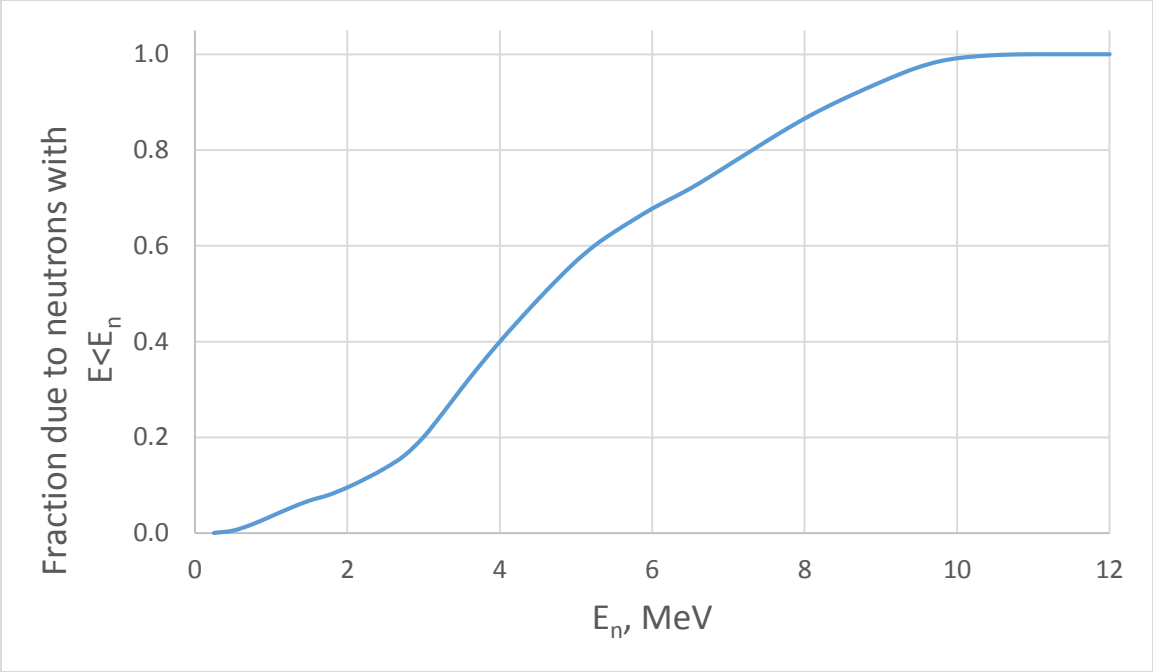

Figure 2.14: Cumulative distribution function calculated from the ^{239}PuBe neutron energy spectrum.

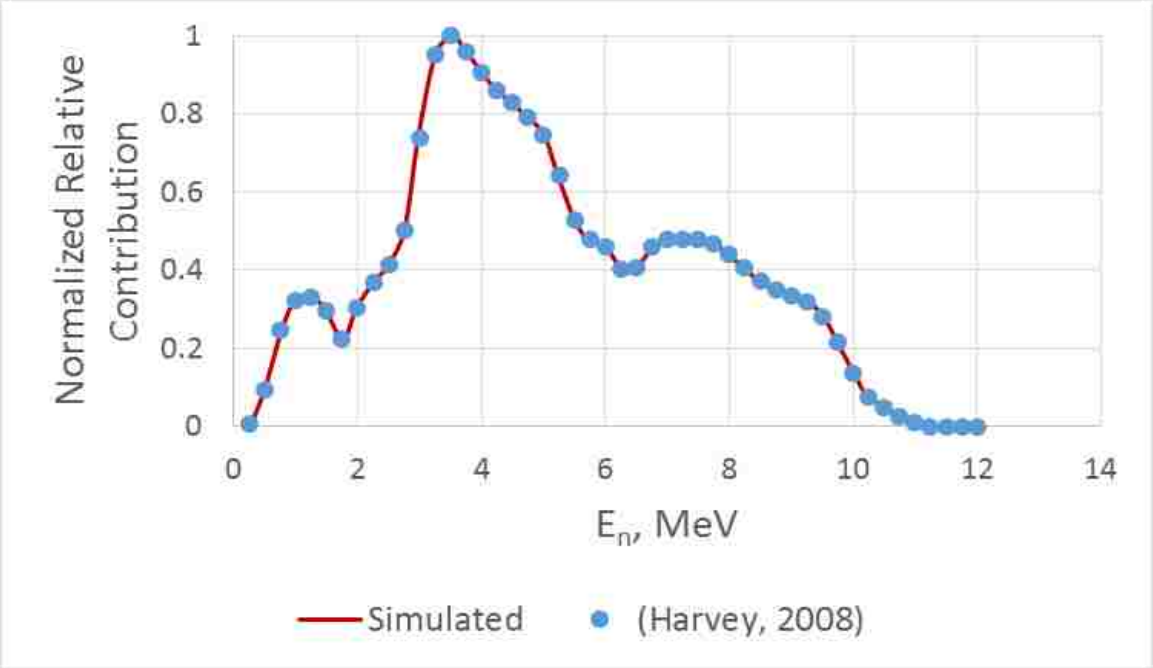

Figure 2.15: Neutron energy spectrum of ^{239}PuBe source

Since the source is a volume and not simply a surface, there will be some self-absorption within the source, depending on the initial position and direction of the protons. The path length that the proton traveled through the TE converter was found and the amount of energy lost along this path was calculated. This energy was then subtracted from the proton's initial energy, before it encountered the layer of air between the TE converter and the detector. The amount of energy lost in the air and SiO_2 layer atop the device were similarly calculated and subtracted from the proton energy before it encountered the silicon SV. If at any of these steps, the energy of the proton fell below a minimum threshold (1 keV), then the energy deposited for that history was set to zero. Finally, the chord length the proton travels through the SV was recorded for each history. Post processing of the data then calculates the energy deposition spectrum and microdosimetric y•d(y) vs y spectrum. Figure 2.16 provides a simplified illustration of the converter layer atop one SV, though in the actual simulation, all 1156 SVs were accounted for.

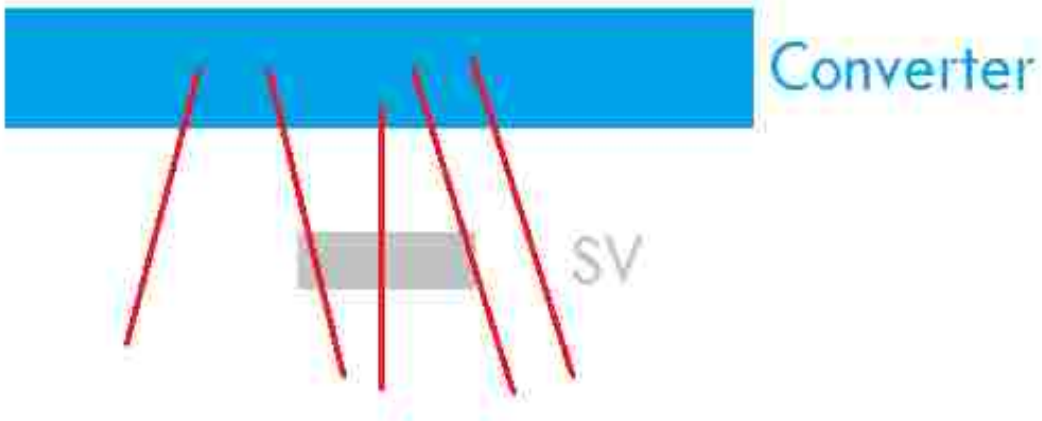

Figure 2.16: Cartoon illustrating MC simulation of the converter layer modeled as a volume source of charged particles.

2.2.5 Acquiring Neutron Spectra

While solid-state detectors respond to charged-particle irradiation, they can also generate signal in response to uncharged particles, including neutrons. However, the detection of these uncharged particles relies on the exploitation of nuclear reactions to generate charged particles as reaction products, which are subsequently detected (Pospisil & Granja, 2009). To satisfy the conditions of Bragg-Gray cavity theory, it is best if all particles being detected are “crossers” which are generated in the medium surrounding the detector, and not “starters,” “stoppers,” or “insiders” generated within the silicon detector itself. In this work, neutron irradiations were performed with a “converter” atop the device (Figure 2.17) to generate charged particles. Ideally, the thickness of this converter should be greater than the range of the secondary charged particles generated by the incoming radiation, to ensure charged particle equilibrium.

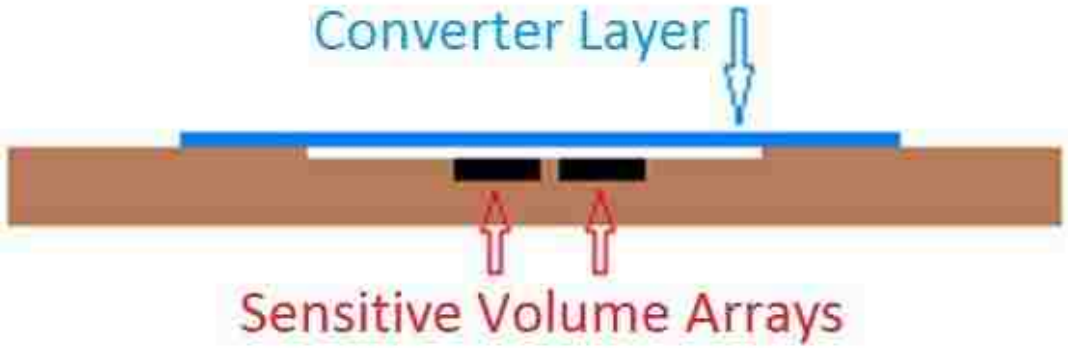

Figure 2.17: Schematic representation of converter layer atop device from side view.

For one of the experiments using the neutron source, a tissue-substitute converter was used to generate recoil protons which are much more likely than an incident neutron to interact in the sensitive volume and generate a signal. The tissue-substitute converter was constructed from 0.1 mm thick high-density polyethylene (HDPE). It has been shown that a bare SOI device can acquire microdosimetric spectra in a mixed gamma-neutron

radiation environment, and this information can be used to determine the relative contribution of silicon recoils and inelastic reaction products generated in the detector (Reinhard et al., 2005). The three isotopes contained in natural silicon (and their abundance percentages) are ^{28}Si (92.2%), ^{29}Si (4.7%), and ^{30}Si (3.1%) (Pospisil & Granja, 2009). The dominant processes by which neutrons can interact in the bare silicon layer are listed in Table 2.2.

Table 2.2: Interaction processes of neutrons in silicon. The rightmost column lists common energies of γ-rays or the threshold energy for slow and fast neutrons, respectively (Pospisil & Granja, 2009).

	Reaction	Eγ or E_n (MeV)
Slow Neutrons	^{28,29,30}Si(n,γ)	≈5-7
	^{28}Si(n,n)	-
Fast Neutrons	^{28}Si(n,α)^{25}Mg	2.8
	^{29}Si(n,α)^{26}Mg	0.04
	^{28}Si(n,p)^{28}Al	4.0
	^{29}Si(n,p)^{29}Al	3.0
	^{30}Si(n,n' γ)	1.8

As an alternative experimental setup, an additional converter was created, which consisted of a layer of epoxy topped with a thin layer of boron powder deposited at the surface (Figure 2.18). This boron converter was placed atop the device, in place of the tissue-substitute converter, to take advantage of the ^{10}B-thermal neutron reaction, which produced a 1.47 MeV alpha particle, a 0.84 MeV ^{7}Li ion, and a 0.48 MeV photon (Figure 2.19).

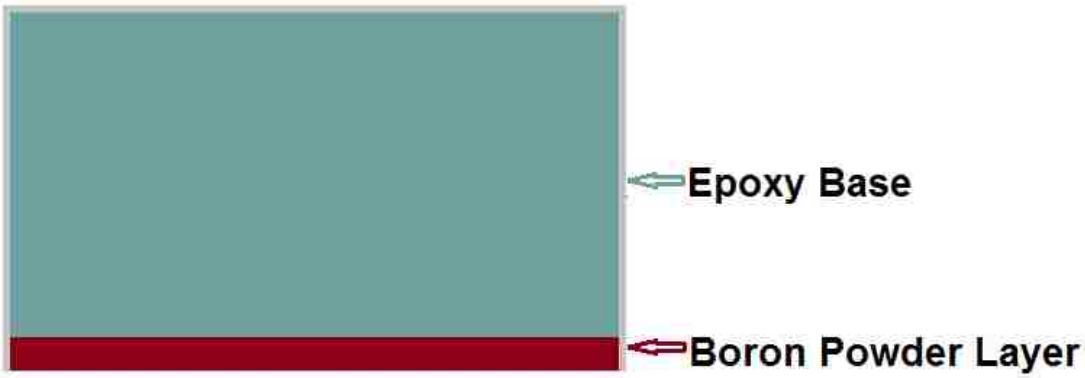

Figure 2.18: Side view of boron converter. (Not to scale)

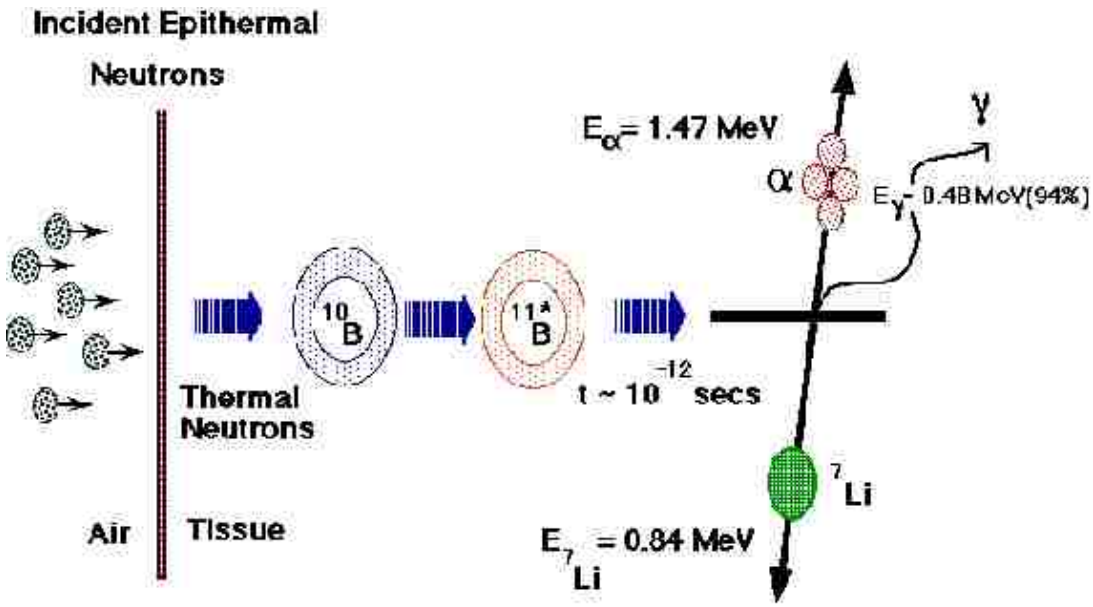

Figure 2.19: Illustration of ^{10}B thermal neutron capture reaction and byproducts ("The Basics of Boron Neutron Capture Therapy," 2005).

The ^{7}Li ion is not energetic enough to penetrate the air and SiO_2 layers above the SV, and the microdosimeter is not sensitive enough to detect the photon, but a proportion of the alpha particles (depending on their spatial origin within the boron layer and their direction of travel) will be able to reach the SVs and deposit some (crossers), or all (stoppers) of their energy within the detector.

Experimental data was collected from one microdosimeter with the output from the circuit board amplifier split and then further amplified using four separate amplifiers in the qMorpho, each applying a different amount of gain. Analyzing the spectra using multiple gains allows for the detection of a wider range of lineal energy events. Typical lineal energy ranges per gain are as follows: Gain 1: 60 to 6800 keV/μm, Gain 2: 50 to 1300 keV/μm, Gain 3: 25 to 500 keV/μm, and Gain 4: 7 to 160 keV/μm. After the spectra were acquired, they were combined using the in-house analysis code. Using the channel to energy conversion equations from the calibration, each spectrum was calibrated in terms of lineal energy. Subsequent data processing was performed using this combined spectrum.

To find the amount of dose delivered to the silicon microdosimeter, the amount of energy deposited per mass was calculated with the following equation:

$$D_{Si}\ (Gy) = \frac{\bar{y}_F\ (keV/\mu m) \bullet \bar{l}\ (\mu m) \bullet N}{M(kg)} k \tag{2.13}$$

where $\bar{y}_F$ is the frequency-mean lineal energy, $\bar{l}$ is the mean chord length for the SV, N is the total number of energy deposition events, M is the total mass of the active area, and k is a units conversion factor ($1.602x10^{-16}\frac{J}{keV}$).

2.2.6 Uncertainty Analysis

The following is a breakdown of the uncertainty calculations for frequency-mean lineal energy ($\bar{y}_F$), dose-mean lineal energy ($\bar{y}_D$), and absorbed dose to silicon (D_{Si}). To calculate the uncertainty in $\bar{y}_F$, consider the way that it is calculated numerically:

$$\bar{y}_F = \sum_i^n \left(y_i \bullet \frac{counts_i}{\sum counts}\right). \tag{2.14}$$

If we let S_i equal the quantity $\left(y_i \bullet \frac{counts_i}{\sum counts}\right)$, then the fractional uncertainty of S_i is found from

$$\frac{\Delta S_i}{S_i} = \sqrt{\left(\frac{\Delta counts_i}{counts_i}\right)^2 + \left(\frac{1}{\sqrt{N}}\right)^2} \tag{2.15}$$

where $counts_i$ is the number of counts per channel, and N is the total number of counts (the uncertainty in y is withheld for now, due to correlation). Then accounting for the summation of S_i,

$$\Delta S_{tot} = \sqrt{\sum_i^n (\Delta S_i)^2} \tag{2.16}$$

the fractional uncertainty in $\bar{y}_F$ is found by combining the uncertainty of S_{tot} and the uncertainty in y from the calibration procedure

$$\frac{\Delta \bar{y}_F}{\bar{y}_F} = \sqrt{\left(\frac{\Delta S_{tot}}{S_{tot}}\right)^2 + \left(\frac{\Delta y}{y}\right)^2}. \tag{2.17}$$

The uncertainty in $\bar{y}_D$ is calculated in a similar fashion. Starting again from the numerical formula:

$$\bar{y}_D = \sum_i^n \left(\frac{{y_i}^2}{\bar{y}_F} \bullet \frac{counts_i}{\sum counts}\right) \tag{2.18}$$

the fractional uncertainty in $\bar{y}_D$ is found from:

$$\frac{\Delta \bar{y}_D}{\bar{y}_D} = \sqrt{\left(\frac{\Delta S_{tot}}{S_{tot}}\right)^2 + 2\left(\frac{\Delta y}{y}\right)^2 + \left(\frac{\Delta \bar{y}_F}{\bar{y}_F}\right)^2}. \tag{2.19}$$

The overall uncertainty in the absorbed dose equation can then be found from:

$$\frac{\Delta D_{Si}}{D_{Si}} = \sqrt{\left(\frac{\Delta \bar{y}_F}{\bar{y}_F}\right)^2 + \left(\frac{1}{\sqrt{N}}\right)^2}. \tag{2.20}$$

2.3 Specific Aim 3 - Convert absorbed dose to silicon to absorbed dose to tissue and dose equivalent to tissue. Quantify uncertainty in dose equivalent to tissue from moderated ^{239}PuBe irradiation

2.3.1 Silicon to Tissue Absorbed Dose Conversion Factor

To convert from absorbed dose to silicon, D_{Si}, to absorbed dose to tissue, D_T, a conversion factor is necessary to account for the differences in mass stopping powers between the two materials. This is a corollary to using cavity theory to determine the dose in the wall of a gas-filled counter from the dose to the gas within the cavity; that is:

$$D_w = D_g r_{w,g} \tag{2.21}$$

where D_w is the dose to the wall, D_g is the dose to the gas, and $r_{w,g}$ is the ratio of mass stopping powers for the wall and the gas:

$$r_{w,g} = \frac{\bar{S}_w}{\bar{S}_g}. \tag{2.22}$$

In microdosimetry, a tissue-equivalent conversion factor of 0.63, as calculated by Bradley and Rosenfeld (1998), is often used. This factor was calculated by considering the ratio of mass stopping powers for silicon and ICRU striated muscle for the ions present in boron neutron capture therapy. Though Bradley and Rosenfeld note that this factor is weakly dependent on ion species and energy, Wroe and Rosenfeld (2007) demonstrate that using the value of 0.63 introduces errors of up to ± 15% for recoil protons over the energy range of 0.1 to 200 MeV.

In this work, the range of particle energies considered was much more narrow (0 to ~12 MeV for the tissue-substitute case's recoil protons and 0 to 1.47 MeV for the boron case's alpha particles). Instead of using the standard 0.63 value, unique absorbed dose conversion factors were calculated for each case, based on the energy spectra extracted from the MC simulations.

For each case, a fluence-weighted mass stopping power ratio for silicon and tissue was calculated:

$$r_{Si,T} = \frac{\sum \Phi(E)\left(\frac{dE}{\rho dx}\right)_{Si}}{\sum \Phi(E)\left(\frac{dE}{\rho dx}\right)_{T}} \tag{2.23}$$

where $\Phi(E)$ is the normalized relative contribution of each energy bin to the overall particle fluence, and $\frac{dE}{\rho dx}$ is the mass stopping power for each energy bin. Dose to tissue was then found from:

$$D_T = \frac{D_{Si}}{r_{Si,T}}. \tag{2.24}$$

2.3.2 Dose Equivalent Conversion

To account for the differences in biological effects of different types of radiation, a quantity called dose equivalent is used. This quantity is calculated by multiplying the absorbed dose in tissue by a quality factor, $\bar{Q}$:

$$H = D_T \int_0^\infty Q(y)d(y)dy = \bar{Q}D_T \tag{2.25}$$

where $Q(y)$ is calculated for each spectrum according to the definition provided by the ICRU, as a function of lineal energy (ICRU, 1986):

$$Q(y) = \frac{5510}{y}\left[1 - e^{-5x10^{-5}y^2 - 2x10^{-7}y^3}\right]. \tag{2.26}$$

Defining Q in terms of lineal energy is advantageous since it can then be measured with a microdosimeter, even in an unknown radiation field. Figure 2.20 shows $Q(y)$ on a log-log plot.

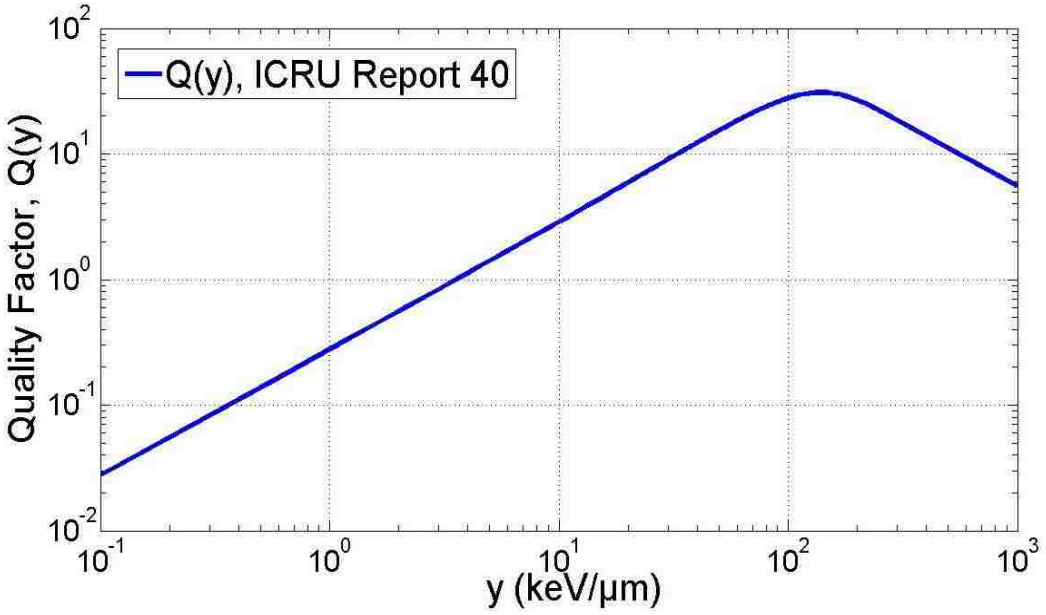

Figure 2.20: The quality factor, Q, as a function of lineal energy, as defined by ICRU Report 40 (1986).

2.3.3 Uncertainty Analysis

Since the quality factor, as defined by the ICRU, is a strict legal definition for radiation protection purposes, no uncertainty will be considered for the calculated $\bar{Q}$ values. However, uncertainty for the absorbed dose conversion factor, $r_{Si,T}$, will be calculated by considering the difference of each value of the stopping power ratio (per energy bin) to the value of the fluence weighted ratio:

$$\frac{\Delta r_{Si,T}}{r_{Si,T}} = \frac{\left|\left(\frac{\left(\frac{dE}{\rho dx}\right)_{Si}}{\left(\frac{dE}{\rho dx}\right)_{T}}\right) - r_{Si,T}\right|}{r_{Si,T}}. \tag{2.27}$$

The largest difference, as calculated above, will be used for the uncertainty in $r_{Si,T}$.

3 RESULTS

3.1 Specific Aim 1

3.1.1 Observed Versus Expected Count Rates

To properly compare observed versus expected count rates from Source 1, the activity profile across the source was measured. The measured activity profile of Source 1 (Figure 3.1) was equivalent in both the x and y directions. The source activity was found to have a gradual falloff as the radial distance from the center increased. Since the profile was equivalent in both x and y directions, the source activity profile was considered as a truncated cone in three-dimensional space. The volume of this truncated cone (the purple section in Figure 3.2) was found by subtracting the volume of the small cone on top from the volume of the overall cone, using the equation for the volume of a right circular cone:

$$V = \pi r^2 \frac{h}{3} \tag{3.1}$$

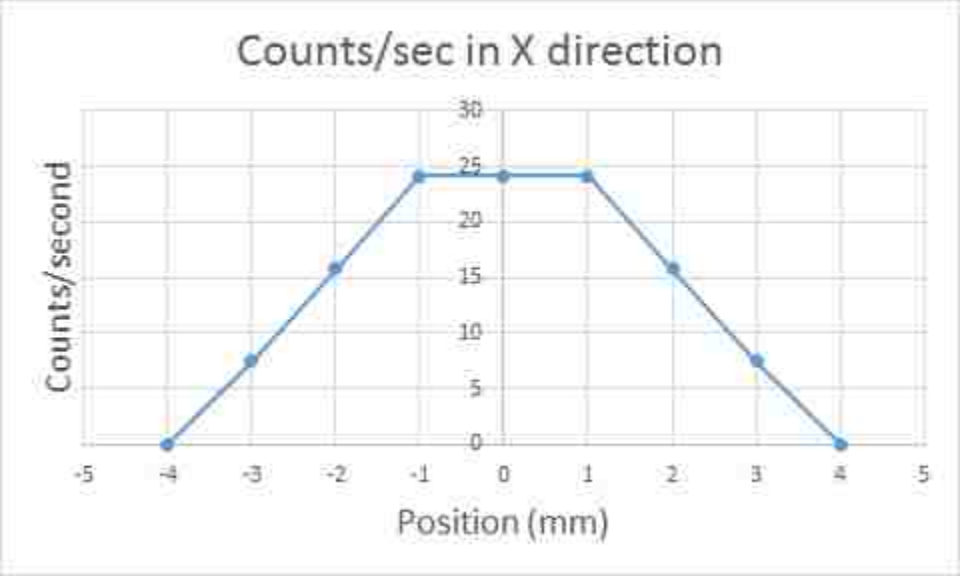

Figure 3.1: Measured activity profile across ^{241}Am source.

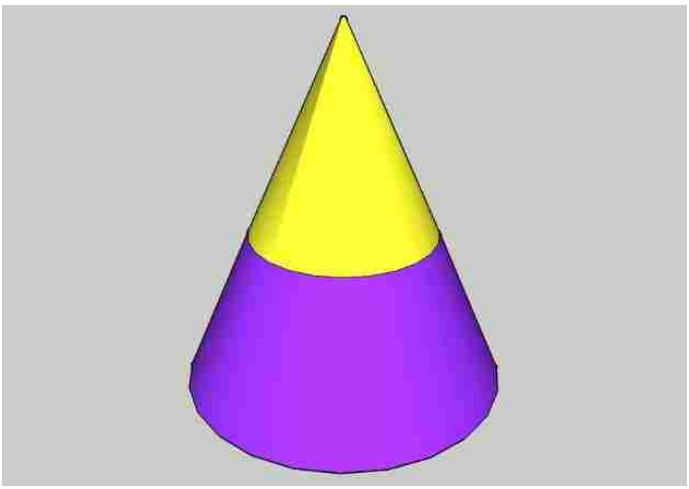

Figure 3.2: Depiction of truncated cone source profile.

The volume of the truncated cone was set equal to the volume of an equivalent cylinder, and the diameter of this cylinder was calculated from

$$d = 2 * \sqrt{\frac{V}{\pi * h}}. \quad (3.2)$$

The effective equivalent cylinder was found to have a diameter of 5.28 mm, which is close to the quoted 5 mm active diameter found on the source calibration certificate. This value was then used in the Monte Carlo simulations. This process was not performed on Source 2 since its small active area was nearly the same size as the collimation hole.

The experimental observed vs. expected count rate results, broken down by SV design, are seen in Figure 3.3. The reported values were averaged from repeated measurements with three different microdosimeters, to account for chip to chip variations. The level of agreement varies, depending on array design. However, all array designs

except the 12.6 µm cylinder representing the lens epithelial cell showed agreement with expected values within 10%.

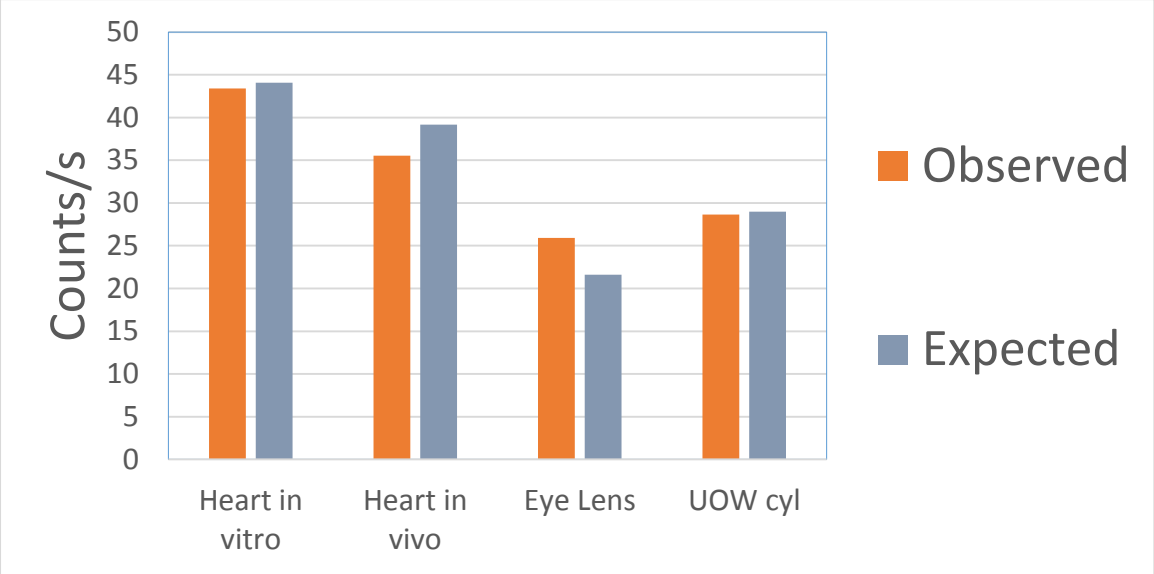

Figure 3.3: Observed versus expected count rates from alpha particle irradiation for each array design.

3.1.2 Monte Carlo Simulations

The results of the alpha particle Monte Carlo simulations revealed a strong dependence on the diameter of the source and on the SSD. The smaller the source diameter, and the further away the source, the more the source approximated a point-source and the more the chord length distribution narrowed about the dimension representative of the detector thickness (Figure 3.4). Energy deposition spectra for the 18 µm cylinder array under alpha particle irradiation with two different SSDs are shown in Figure 3.5. The majority of the events were from alpha particles traveling straight through the thickness of the detector. Events on the left side of the peak represented alpha particles that traversed a chord length less than the height of the detector, while events to the right of the peak were from chord lengths greater than the height of the

detector. Figure 3.6 shows the 3 mm SSD spectrum converted into the microdosimetric y•d(y) format.

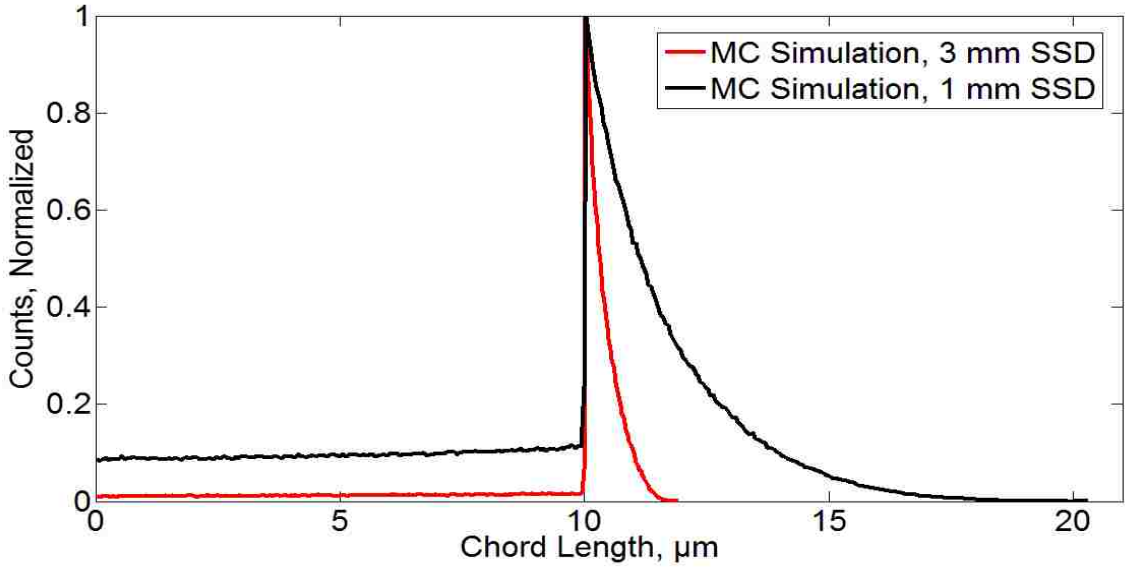

Figure 3.4: MC simulated chord length distribution for 18 µm cylinder under alpha particle irradiation, showing dependence on SSD.

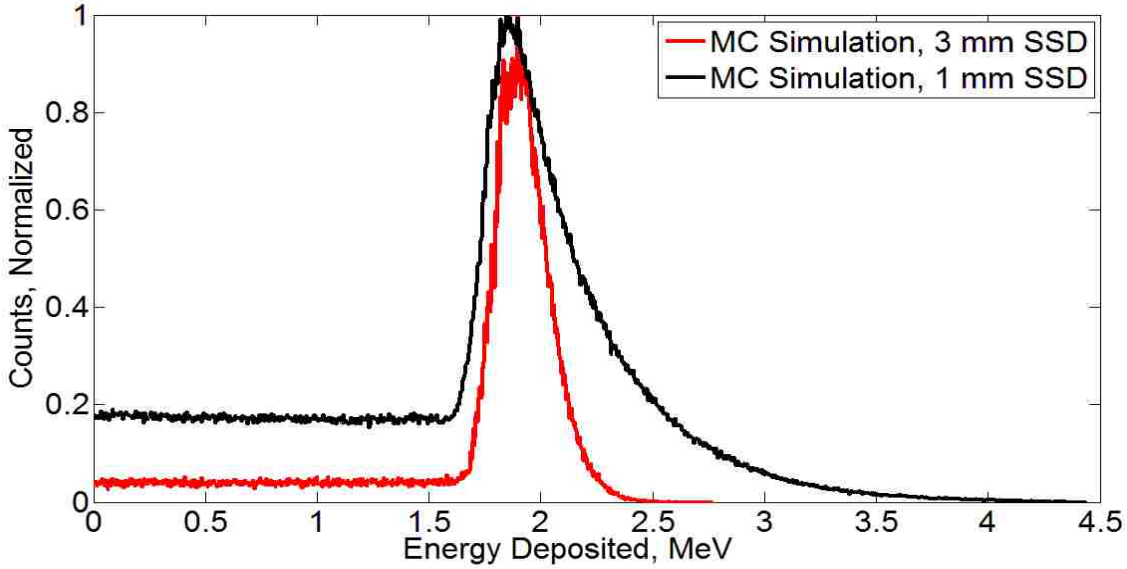

Figure 3.5: MC simulated energy deposition spectra for 18 µm cylinder under alpha particle irradiation, showing dependence on SSD.

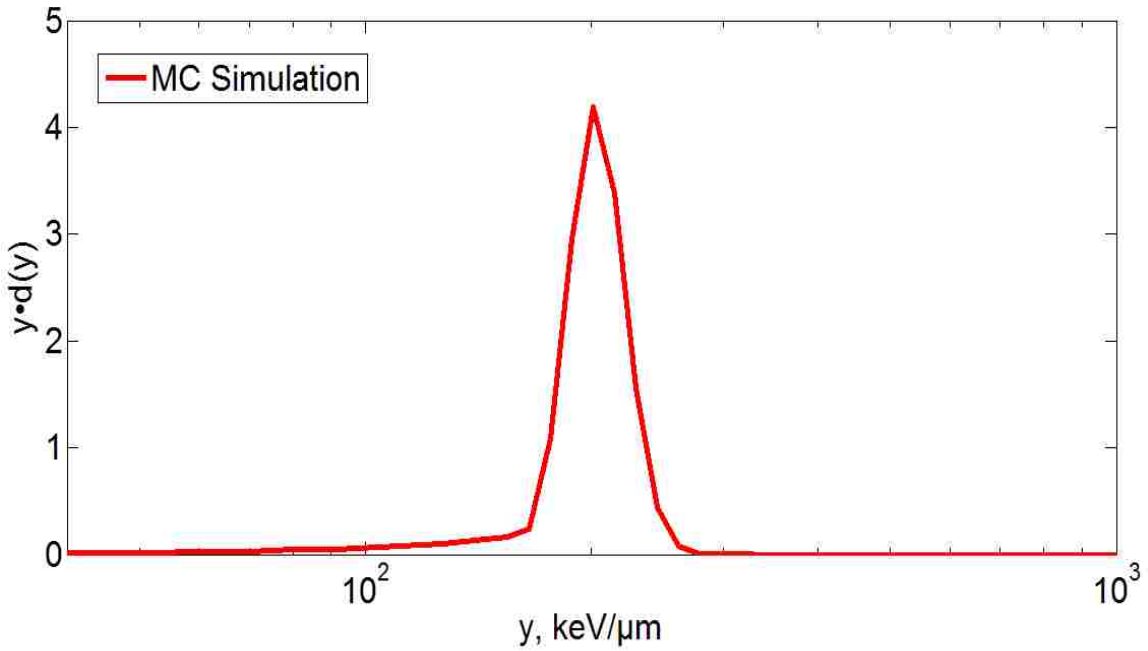

Figure 3.6: MC simulation y•d(y) vs. y from alpha particle irradiation for the 18 μm cylinder with 3 mm SSD.

3.1.3 Benchmarking of Monte Carlo Code

Since the MC code used for this project was an in-house program and had not been previously benchmarked against other codes, comparisons were made with well-established methods to test the accuracy of the model. The same experimental setup was modeled in the in-house code and in the GEANT4 Monte Carlo code (http://www.geant4.org/geant4). The simulated setup was a ^{239}PuBe irradiation using the boron converter. The results are plotted in Figure 3.7. Spectra were normalized so that the total area under each of the curves was equal to one.

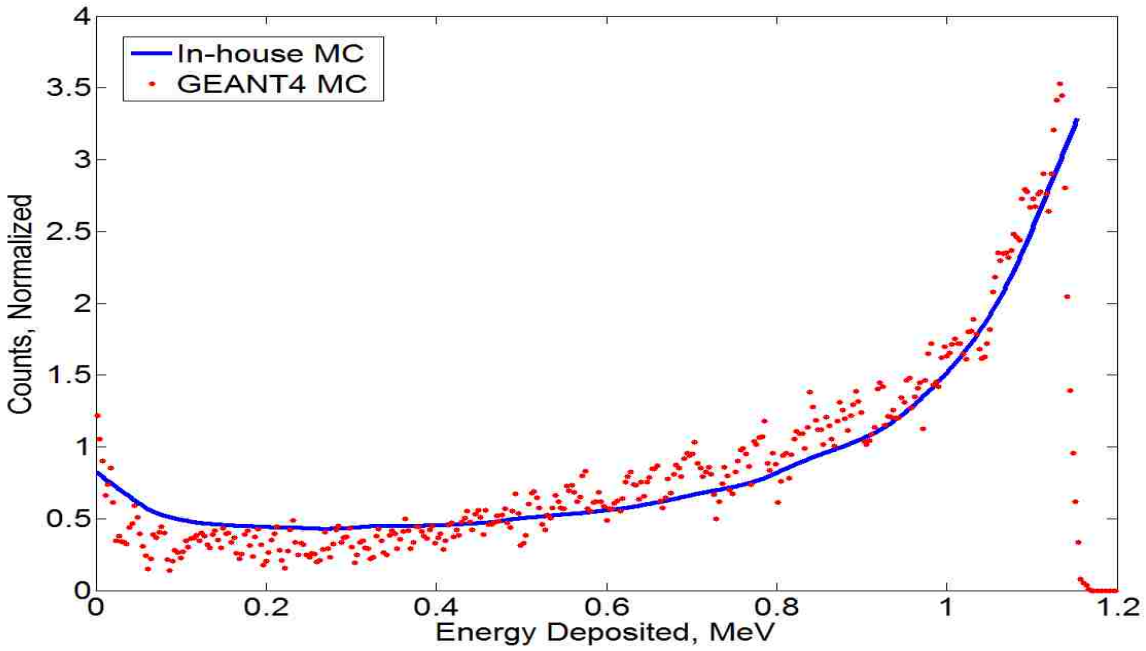

Figure 3.7: MC simulations with boron converter (alpha particles emitted solely from surface of converter).

The in-house code was also compared with a derived analytical solution for the chord length distribution in the extreme case of an infinite slab of height h subjected to an external isotropic radiation source. The analytical solution to the chord length distribution for this geometry was derived to be:

$$c(l) = 0 \qquad \text{for} \qquad l < h \tag{3.3}$$

$$c(l) = \frac{h}{l^2} \qquad \text{for} \qquad l \geq h. \tag{3.4}$$

The analytical and simulated results are plotted in Figure 3.8. The fluctuations in events increases with chord length because of their decreasing frequency of occurrence, but the analytical and simulated results matched well.

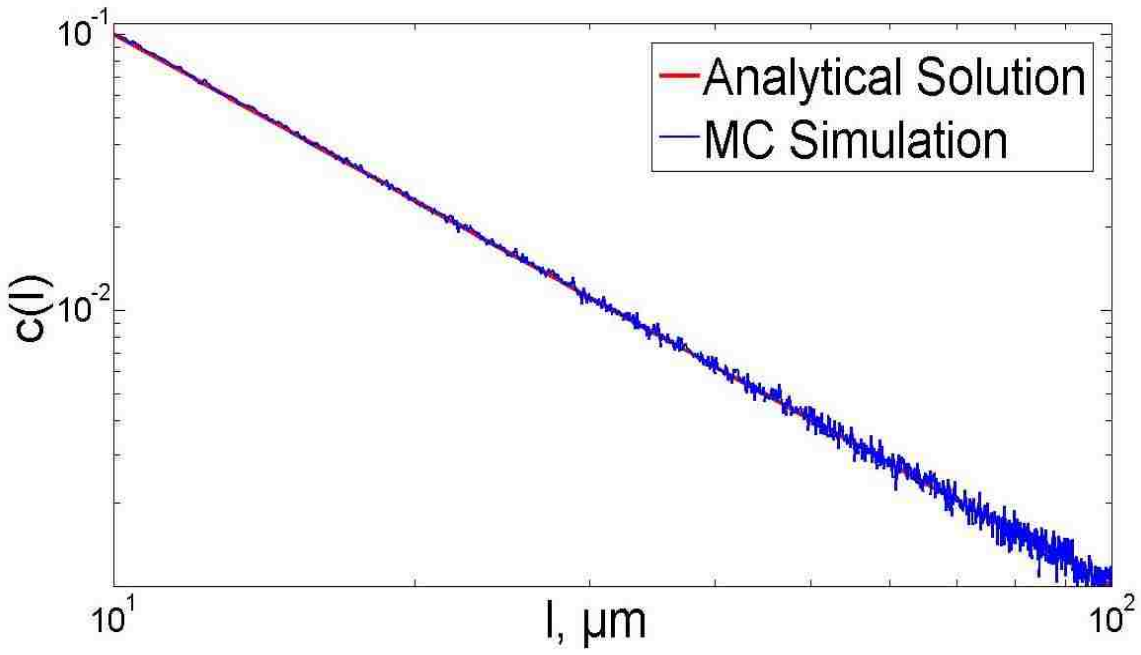

Figure 3.8: MC simulation and analytical chord length distribution for infinite slab SV under isotropic radiation.

Finally, the in-house code was compared with results from the Transport of Ions in Matter (TRIM) Monte Carlo code (http://www.srim.org). The simulation modeled the energy loss of 1.47 MeV alpha particles traveling through varying thicknesses of boron, to simulate alpha particles being generated by neutrons throughout the boron converter. Each alpha particle then traveled through 1 mm of air and 0.35 μm of SiO_2 before encountering the SV. The energy deposited in the SV was then tallied and converted to lineal energy. Table 3.1 lists the results, which were in good agreement except for the 3 μm thick boron case. However, 3 μm was very close to the end of range for these alpha particles, which is where uncertainties in stopping powers are at their highest (ICRU, 1993). Otherwise, the fluctuation in percent difference was due to slight discrepancies between the stopping power data set used in the TRIM code and the ASTAR stopping power data set used in the in-house code.

Table 3.1: Comparison of energy deposition predicted by the in-house and TRIM MC codes.

	Energy Deposited in SV, keV/μm		
Thickness of boron layer, μm	In-house code	TRIM	% Diff
3	0.30	0.606	50.5%
2.9	1.40	1.33	5.3%
2.85	2.11	1.97	7.1%
2.8	2.93	2.69	8.9%
2.75	3.85	3.63	6.1%
2.7	4.86	4.62	5.2%
2.65	5.97	5.67	5.3%
2.6	7.18	6.88	4.4%
2.5	9.83	9.52	3.3%
2	27.77	27.3	1.7%
1.5	50.34	50.1	0.5%
1	74.65	74.7	0.1%
0.5	99.03	98.8	0.2%
0	121.85	122.2	0.3%

3.1.4 Alpha Spectrum Acquisition

An example of an ^{241}Am energy deposition spectrum acquired with the 18 μm cylinder array can be seen in Figure 3.9. The overall shape of this distribution differed slightly from the Monte Carlo simulations seen in Section 3.1.2, but did agree well with a

spectrum previously acquired at UOW with a SOI detector of a similar size, seen in Figure 3.10 (Hu, 2013).

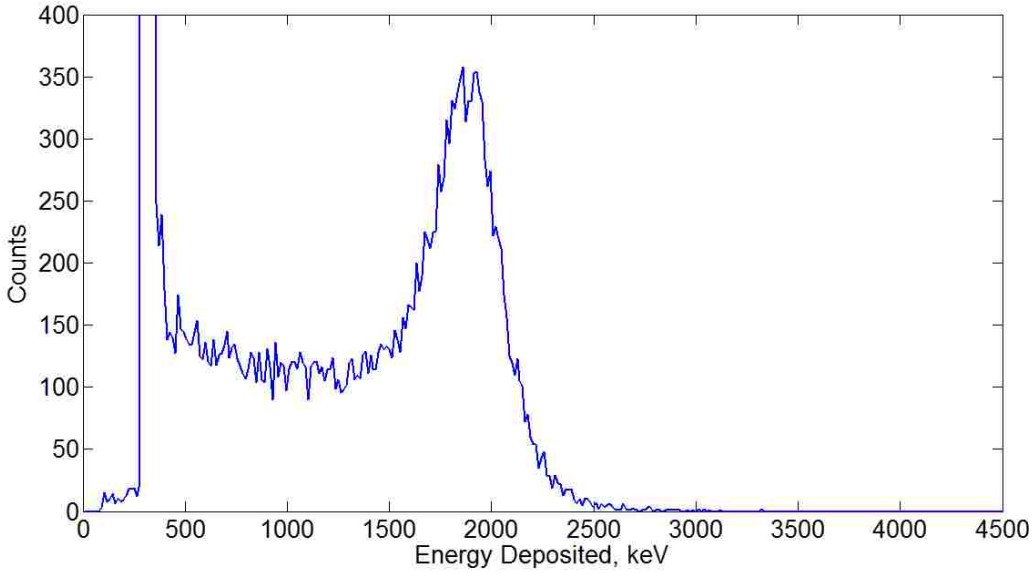

Figure 3.9: ^{241}Am spectrum acquired with the array of 18 µm cylinders in air and with a floating guard ring.

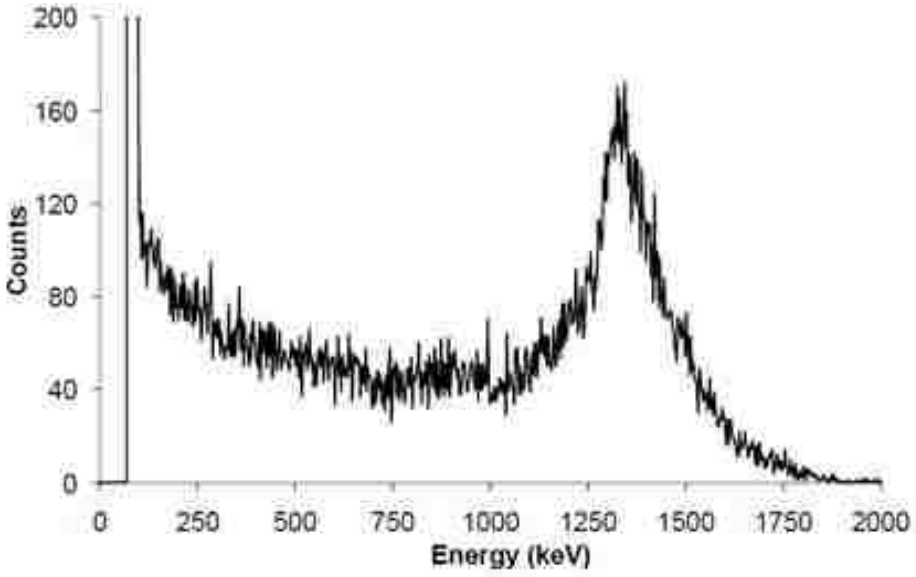

Figure 3.10: ^{241}Am spectrum acquired with a 10 µm thick SOI detector under vacuum conditions, with a grounded guard ring. Adapted from (Hu, 2013).

Figure 3.11 plots the microdosimetric y•d(y) vs. y spectrum, as acquired with the 18 µm cylinder SV array. Extrapolation was used for data points below the noise cutoff (Schrewe et al., 1989). The peak centroid was found by the Gaussian fitting procedure described in Section 2.2.4. Also shown in the figure are the calculated proton and alpha edge values, to demonstrate the energy regimes of the different particles.

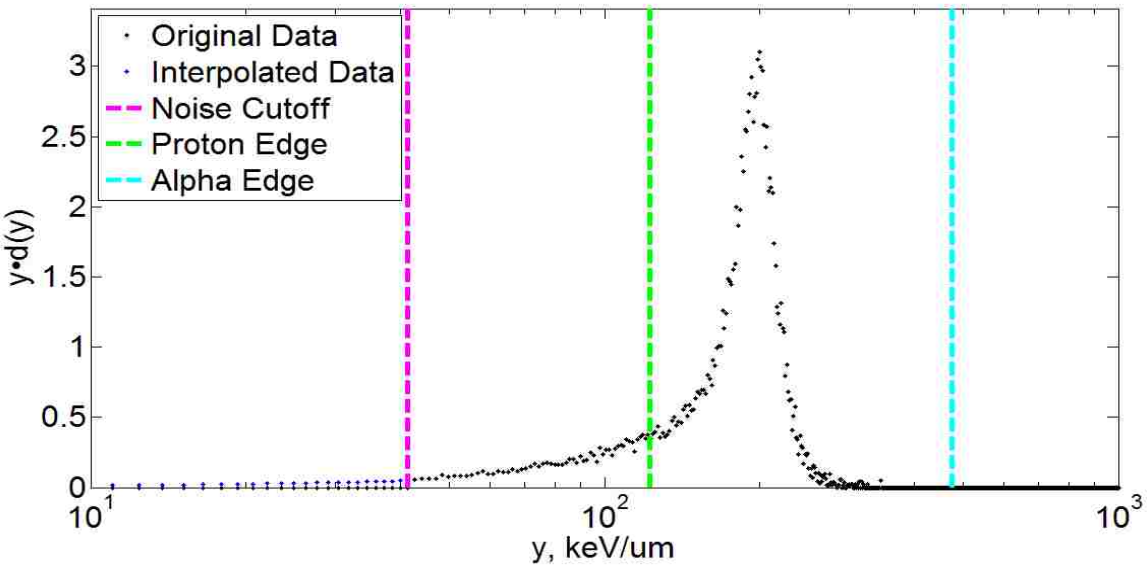

Figure 3.11: Measured microdosimetric alpha particle spectrum acquired with the 18 µm cylinder SV array using Source 2.

3.1.5 Comparing Monte Carlo and Experimental Spectra

When the experimental and the MC data were overlaid, the positions of the alpha particle peaks matched well. The main differences were in the width of the peak, and the peak-to-tail ratio on the left hand side. The broader experimental peak, compared to the matching MC simulation with 3 mm SSD, was likely due to fluctuations in the sensitivity of the 1156 SVs in the array. That is, due to manufacturing variations, each SV exhibited a slightly different response to the same amount of deposited energy. The increase in low energy noise seen on the left side of the peak was likely a result of the guard ring

structure being left “floating” and not biased, which resulted in charge-sharing between SVs across the device and an increase in the amount of low-energy depositions (Tran & Chartier, 2014; Hu, 2013).

Additional simulations were run, with the SSD shortened to 1 mm, to test if the peak-to-tail ratio discrepancy was due to experimental errors in estimating the SSD, or if the discrepancy was due to geometrical errors in the MC code. The results of varying the SSD in the MC simulations are seen in Figure 3.12. Each spectra was normalized to its peak height. When a 1 mm SSD was simulated, the peak positions still matched well, and low-energy events registering on the left side of the peak (from chord-lengths shorter than the SV thickness) were in better agreement with the experimental data. However, the higher-energy tail on the right side of the peak (from chord-lengths longer than the SV thickness) extended farther. This longer energy tail was to be expected, since a shorter SSD allowed the alpha particles to enter the SV at larger angles - resulting in longer chord-lengths being traversed by the alpha particles and subsequently higher energy deposition events.

In the y•d(y) distributions seen in Figure 3.13, the trends were the same as in the energy deposition spectra. The positions of the peaks matched well for all three curves, but the peak to tail ratios differed, with the experimental data showing a higher proportion of low-energy events than either of the MC simulations. The 1 mm SSD simulation again showed a higher proportion of high-energy events.

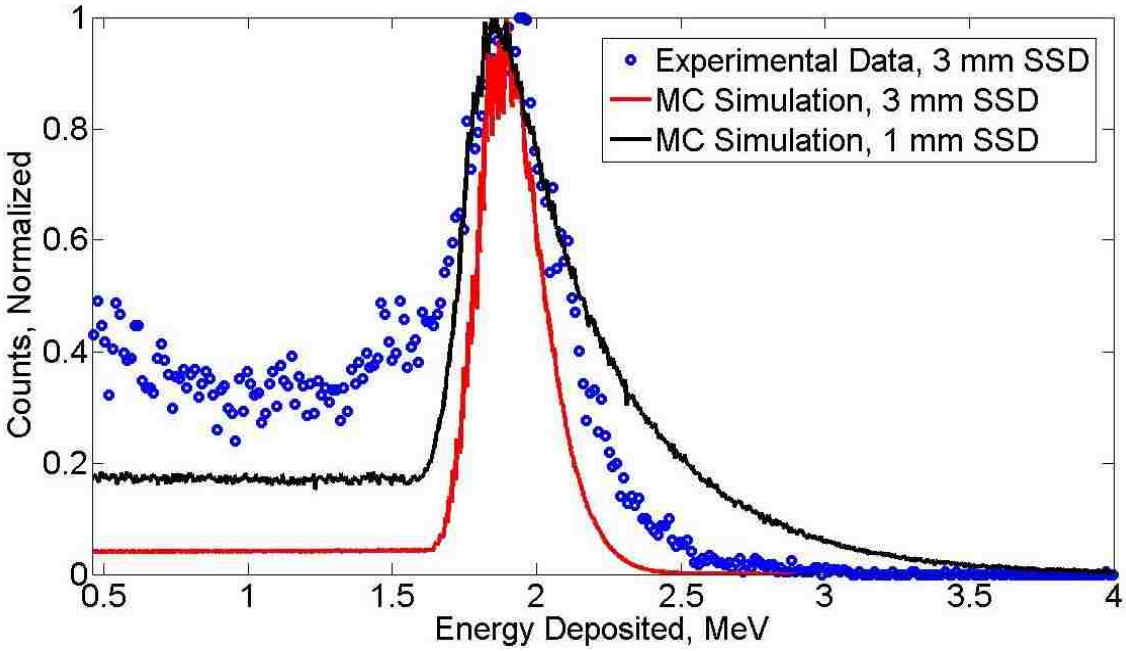

Figure 3.12: Energy deposition spectra for Experimental data, MC simulation with 3 mm SSD, and MC simulation with 1 mm SSD.

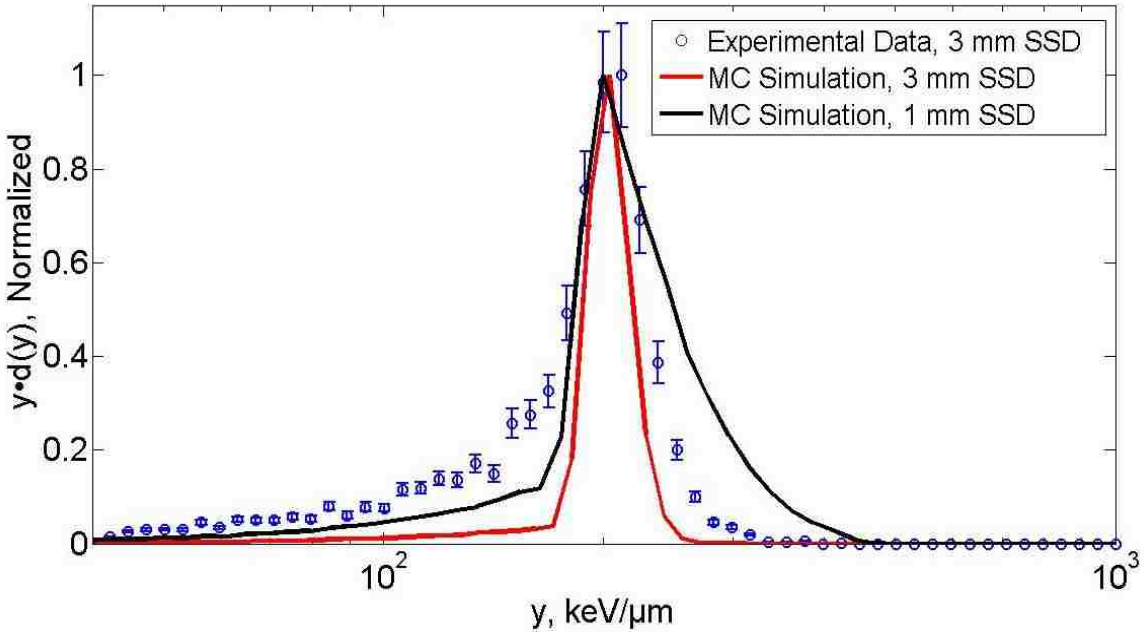

Figure 3.13: y•d(y) vs y spectra for Experimental data, MC simulation with 3 mm SSD, and MC simulation with 1 mm SSD.

To investigate the impact of variations in the sensitivity of SVs in an array, the geometric chord length for each particle history was lengthened or shortened by a normally distributed amount, with the standard deviation equal to ± 5% or ± 10%. As seen in Figure 3.14, the alpha particle simulations were very sensitive to the chord length variations. As the maximum amount of variation was increased, the corresponding simulated peak became increasingly wider, as expected. Increasing the variation brought the width of the simulated peak into better agreement with the experimental peak. Neither of the modified simulations produced total agreement in the overall shapes of the spectra, with a higher proportion of low-energy events consistently seen in the experimental peak. Experimentally, it makes sense that the alpha particle response would be very sensitive to chord length variations, since the emission of alpha particles from the source was fairly directional and the detector response varied depending upon the angle of incidence of the alpha particles.

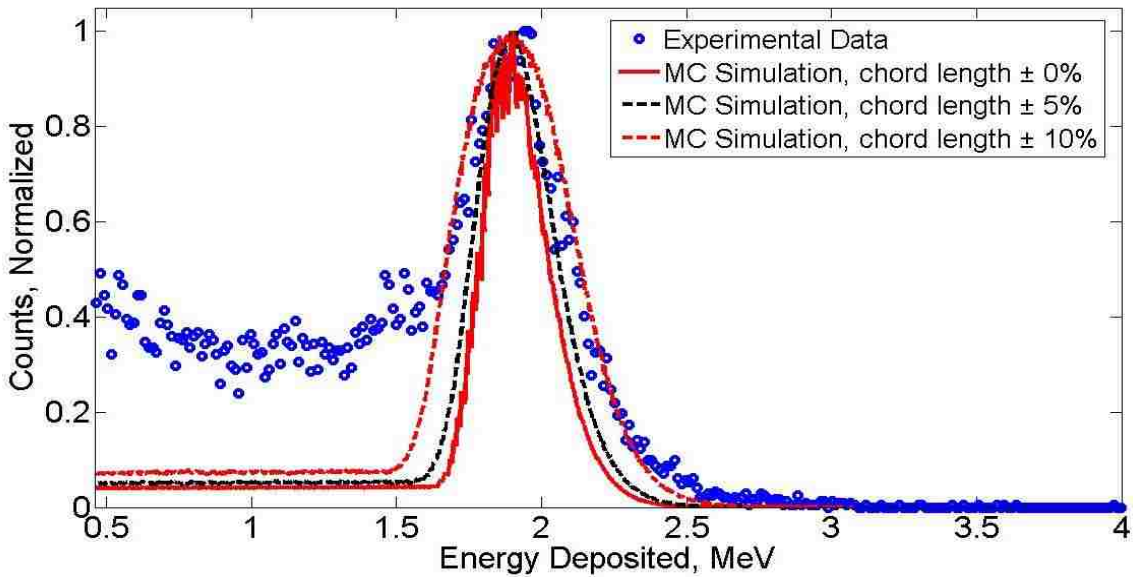

Figure 3.14: Effect of varying the chord lengths in the alpha particle simulations, in terms of energy deposition.

Also investigated was how varying the chord lengths in the simulations would affect the y•d(y) distributions. It was found that the y•d(y) spectra were slightly less sensitive to the variations, though the spectra still became increasingly wider as the maximum amount of variation was increased (Figure 3.15). As was the case with the energy deposition spectra, even though modifying the chord lengths brought the width of the peaks into better agreement, neither of the modified y•d(y) spectra matched the experimental spectra in the low lineal energy region.

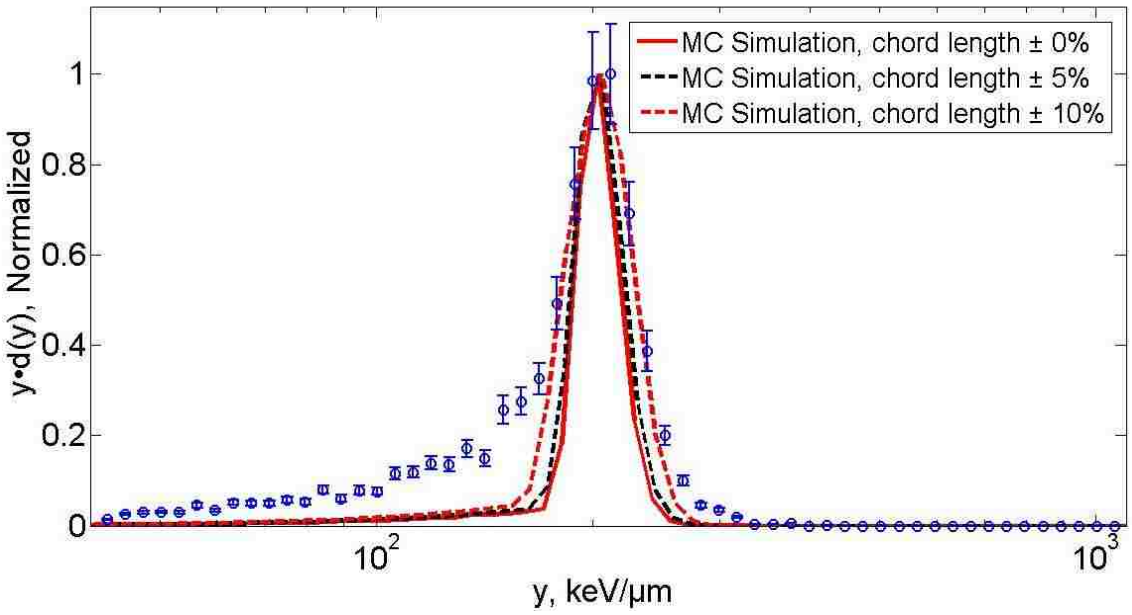

Figure 3.15: Effect of varying the chord lengths in the alpha particle simulations, in terms of y•d(y).

3.1.6 Uncertainty of Calibration Procedure

The main sources of uncertainty involved in the calibration to lineal energy are: stopping power value uncertainty, sensitive volume manufacturing tolerances, and fluctuations in the channel of the alpha peak. The measurement of the energy of the alpha particles emitted from the two sources used, as described in Section 2.1.1, is estimated to have an uncertainty of 2% due to calibration fluctuations. Adding or

subtracting this 2% from the calculated mean source energies results in a 2.5% discrepancy when looking up ASTAR stopping power values. The silicon wafer used in the construction of the microdosimeters was specified as having a thickness of 10 ± 0.5 μm. This 5% uncertainty is likely conservative, but was included in the uncertainty analysis. Analyzing repeated alpha calibration measurements revealed that the channel number of the acquired alpha particle spectra fluctuated by ± 2%. Propagating these uncertainties, as well as the uncertainties of the α and β calibration coefficients, in quadrature resulted in a total calibration uncertainty of 6.1% (Table 3.2).

Table 3.2: Experimental calibration uncertainty values.

Uncertainty	Value
Stopping Power Values	2.5%
SV thickness	5.0%
Reference Channel	2.0%
Total	6.1%

3.2 Specific Aim 2

3.2.1 Chip Surface Images

Microscopic images of each chip were analyzed to assess their physical surface conditions. A wide range of chip surface conditions were observed under the microscope, with some of the chips showing rather extensive scratches, while others were relatively free of surface damage (Figure 3.16). The source of the damage is not clear; it may have occurred during the original manufacturing process, during shipping, during the re-wiring process, or was just due to their being handled and used in the lab. Regardless of the

origin of the damage, this information about the physical conditions of each chip was taken into account when selecting chips to be used for experimentation.

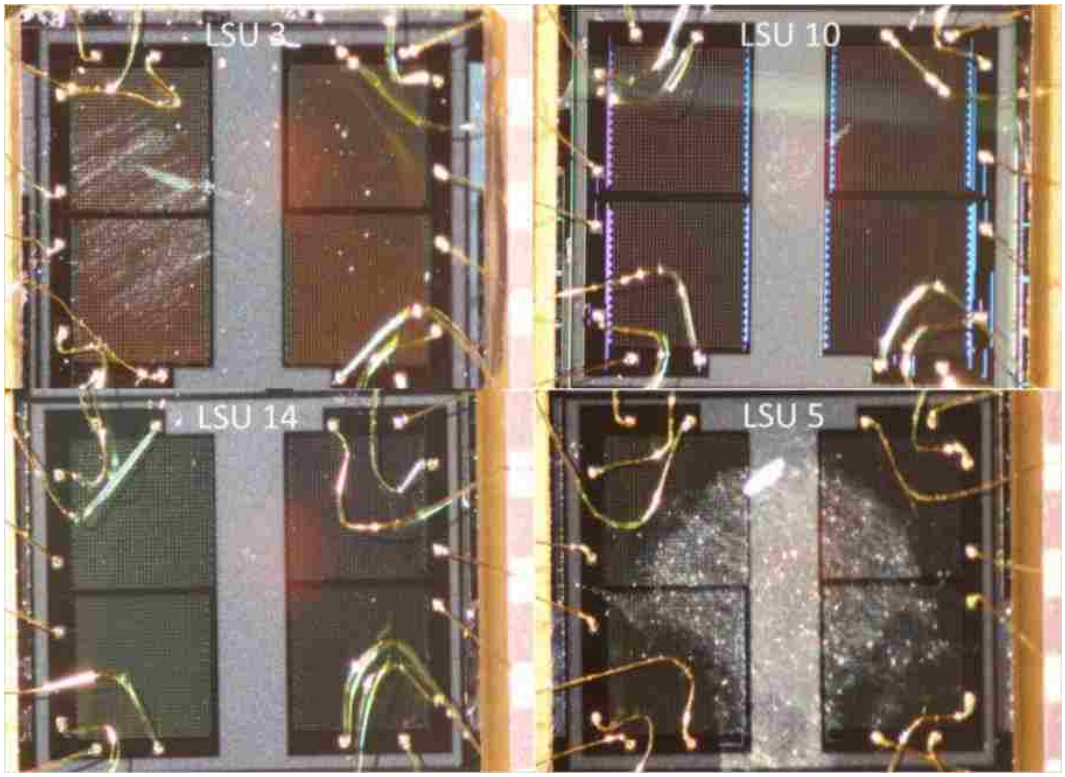

Figure 3.16: Representative chip surface images showing range of surface conditions (scratches, dents, etc.).

3.2.2 Leakage Current Measurements

In addition to the chips created for this project, several chips were acquired from UOW for comparison. Figure 3.17 shows representative leakage current versus bias voltage plots for both sets of chips. Variations between array designs were expected, due to size and shape differences, but chip to chip variations for the same array design were also observed. We attributed these to manufacturing variations, surface defects, and other factors. There are a few trends apparent in the data. Overall, for a given amount of reverse bias voltage, the LSU chips exhibited much higher leakage current than the UOW chips. This was likely due to differences in the underlying silicon wafers.

The manufacturing specifications for the LSU chips called for the use of a high-resistivity silicon wafer with resistance of 10 kΩ•cm, which would be equivalent to that used in the manufacturing of the UOW chips. However, the specified wafer could not be sourced within the short timeline of the supporting grant, and a lower-resistivity silicon wafer with resistance of 1 kΩ•cm was substituted. The lower resistance wafer apparently resulted in more leakage current at all bias voltages considered.

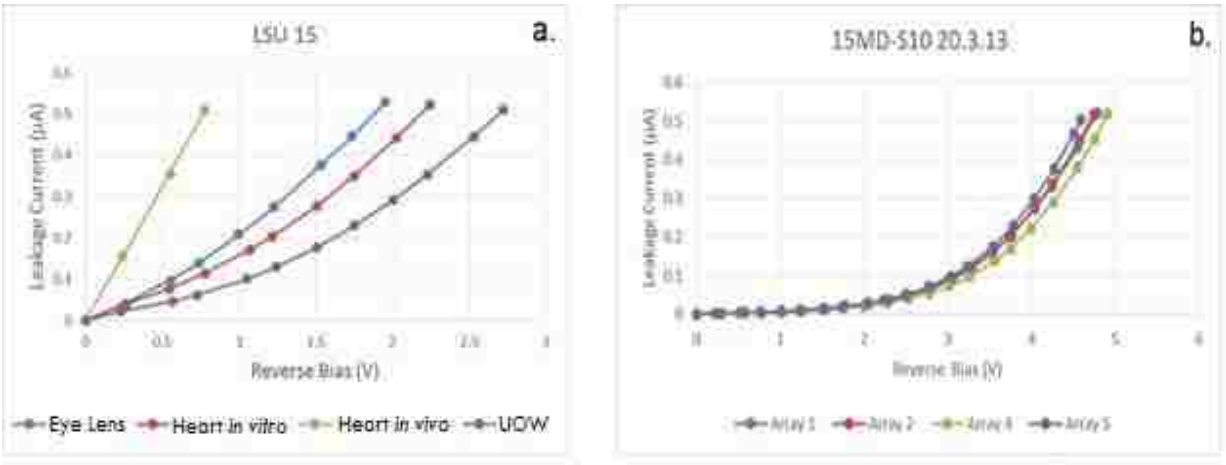

Figure 3.17: Representative plots of leakage current measurements with a. LSU chips and b. UOW chips.

Also evident in the LSU chips were leakage-current patterns from one array design to another. The arrays on the UOW chip were all populated with the same SV design, which led to consistent leakage current values for each array. Whereas the LSU chips, with different SV designs, showed much more variability between arrays. The average leakage current values are listed in Table 3.3 (the full table of values can be found in Table 6.1 in the Appendix). The array with the smallest SV, the 12.6 μm cylindrical SV that represented the lens epithelial cell, tolerated the highest bias voltage.

The general trend with the cylindrical SVs is that a smaller SV can be biased to a higher voltage before exceeding the 0.5 μA leakage current threshold. However, the

elliptical SV, which represented the heart endothelial cell *in vivo*, reached the leakage current threshold at a lower bias voltage than all the other SVs even though its area was smaller than the 18 µm cylindrical SV. This may be due to the basic shape of the elliptical SV. The elliptical structure was designed so that the spacing between the n and p rings was uniform, but charge may still tend to collect at the points of the ellipse farthest from the center (B. Gila, personal communication, Mar. 21, 2014). Also, the footprint of the elliptical SV was relatively large and did not leave much room for error in terms of spacing of the n-type and p-type structures. Thus, a small shift in the relative position of the n-type and p-type structures might have a much larger effect with the elliptical SV as compared to the cylindrical SVs.

Table 3.3: Bias voltages per array design to reach 0.5 µA leakage current threshold. Measurements were performed on multiple chips and the results averaged to determine the "Average Max. Bias Voltage" for each array.

Array Design	12.6 µm cylinder	14.6 µm cylinder	18 µm cylinder	24 µm x 12 µm ellipse
2D Area of one SV (μm^2)	124.7	167.4	254.5	226.2
Average Max. Bias Voltage (V)	3.4	2.5	1.8	1.1

3.2.3 Circuit Board Modifications

After initial testing, it was discovered that the RC time constants on the circuit board for the AD 829 buffer amplifier were mismatched and did not provide significant shaping of the pulse from the A250f preamplifier. The time constant, τ, is defined as:

$$\tau = RC \tag{3.5}$$

with *R* being the resistance in ohms, and *C* the capacitance in farads. To correct this, capacitors C2 and C12 (Figure 6.1 in Appendix) were changed from 4.7pF and 0.1 µF,

respectively, to 1 nF. This change allowed for matched RC time constants of ~1μs and provided the desired amount of pulse shaping.

Another modification was the creation of a "splitter" (Figure 3.18) so that the signal output from one SV array could be split into multiple amplifiers, each applying a different amount of gain. This was necessary for the neutron measurements, where the dynamic range of lineal energy events typically spans three to four decades.

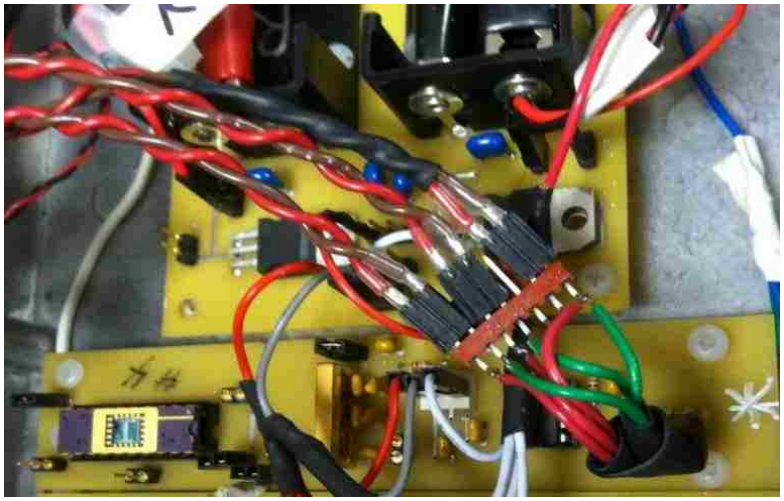

Figure 3.18: Splitter to separate microdosimeter output into multiple independent linear amplifiers to enable simultaneous acquisition of events spanning three to four decades of lineal energy.

The original design of the circuit board did not reverse bias the SVs. To accommodate this, 10 MΩ resistors were added in series with the SV n-type cores, and these were then connected to the output of a potentiometer which allowed for the application of bias voltage from ~0.2 V to 6 V.

During initial testing, random fluctuations in the signal from the device led to the discovery of a damaged data wire connection from the qMorpho to the USB cable connecting the computer to the microdosimeter. There were also grounding issues, since the GND connection in the USB cable between the MCA and the computer was not being

utilized. A new USB connector was fashioned, providing a secure connection for the data wires and the GND wire. Also, the USB shield wire surrounding the data wires was connected to the aluminum box containing the microdosimeter.

3.2.4 Noise Considerations

The external AC to DC power adapter of the laptop computer was found to contribute a large amount to the low-energy noise peak seen in the pulse height spectra. Unplugging the power supply and running the computer solely on the internal battery reduced the number of noise counts by up to one order of magnitude, depending on which gain setting was being used. Operating the system in this fashion was useful for short-term acquisitions, such as with the alpha particle sources. However, long-term acquisitions, such as with the neutron source, required the external power supply, as the internal battery power was exhausted within two to three hours.

3.2.5 Preliminary Results from UOW Testing

Four of the microdosimeters were sent to UOW for characterization and initial testing. The diode characteristics of the microdosimeters were analyzed with current-voltage (I-V) and capacitance-voltage (C-V) techniques. The I-V technique quantified the amount of leakage current that flowed through each array by applying a reverse bias voltage to the SVs and measuring the current (Model 237, Keithley Instruments, Inc., Cleveland, Ohio). The bias voltage was increased until the leakage current reached a threshold of 0.5 μA to prevent damage to the junctions. The C-V test quantified the capacitance values of each array and was performed in a similar manner using a capacitance meter (Model 7200, Boonton Electronics, Parsippany, New Jersey). The full results of both techniques can be found in the Appendix.

The results of UOW's I-V and C-V tests demonstrated overall poor performance from the chips in terms of their basic diode characteristics. As can be seen in Table 3.4, the leakage current threshold value of 0.5 µA was reached at less than 2 V on twelve out of sixteen total arrays. Two of the arrays were found to be inoperable, and another two arrays had acceptable, but still high, leakage current of 170 nA at 10 V. The C-V measurements were fairly similar across the chips, with typical capacitance values of 10-20 pF seen over the range of operating voltages.

Table 3.4: Table of limiting bias voltages for each LSU chip based on I-V measurements performed at UOW (Tran & Chartier, 2014).

Chip	Device	Array	Limiting Voltage (V)	Chip	Device	Array	Limiting Voltage (V)
LSU1	1	Odd	2	LSU2	1	Odd	4.5
	1	Even	2		1	Even	1.5
	2	Odd	7.5		2	Odd	5
	2	Even	7		2	Even	6.5
	3	Odd	7		3	Odd	6
	3	Even	6.5		3	Even	6.5
	4	Odd	4		4	Odd	3
	4	Even	4		4	Even	2.5
LSU6	1	Odd	6	LSU7	1	Odd	2
	1	Even	8		1	Even	3
	2	Odd	10		2	Odd	-
	2	Even	10		2	Even	-
	3	Odd	4		3	Odd	1
	3	Even	4.5		3	Even	0.5
	4	Odd	0.5		4	Odd	0.5
	4	Even	0.5		4	Even	0.5

The researchers at UOW also noted a range of surface damage visible on the devices, as seen in Figure 3.19. The surfaces of the chips showed significant damage from scratches, dents, and solder splatter. This surface damage may have contributed to the poor diode performance of the chips.

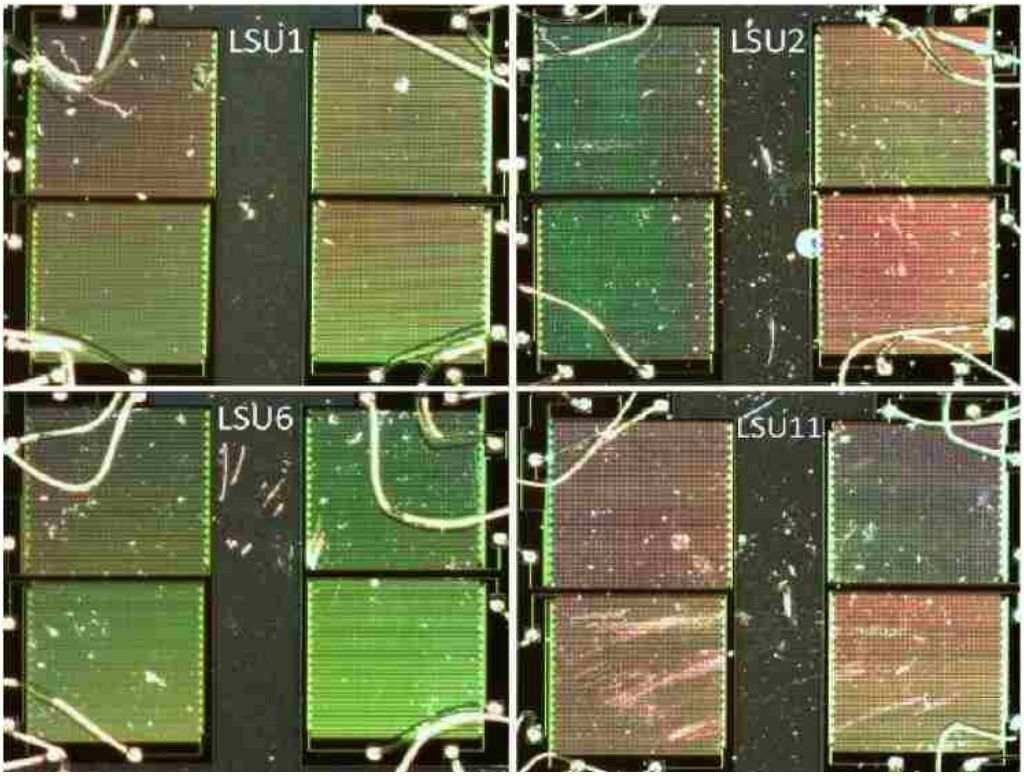

Figure 3.19: Image showing surface conditions observed on the four LSU chips sent to UOW for testing (Tran & Chartier, 2014).

Based upon these tests, the “LSU 6” chip was chosen for further testing with alpha spectroscopy using bias voltages of 0 V, 4 V, 6 V, and 8 V. It was found that the number of observed counts was very low, and that there was a large amount of low energy noise between the electronics noise peak and the alpha peak. Figure 3.20 shows an alpha particle spectrum acquired with the heart endothelial cell *in vitro* SV using 6 V of bias voltage; “odd” and “even” refer to the numbered rows of SVs.

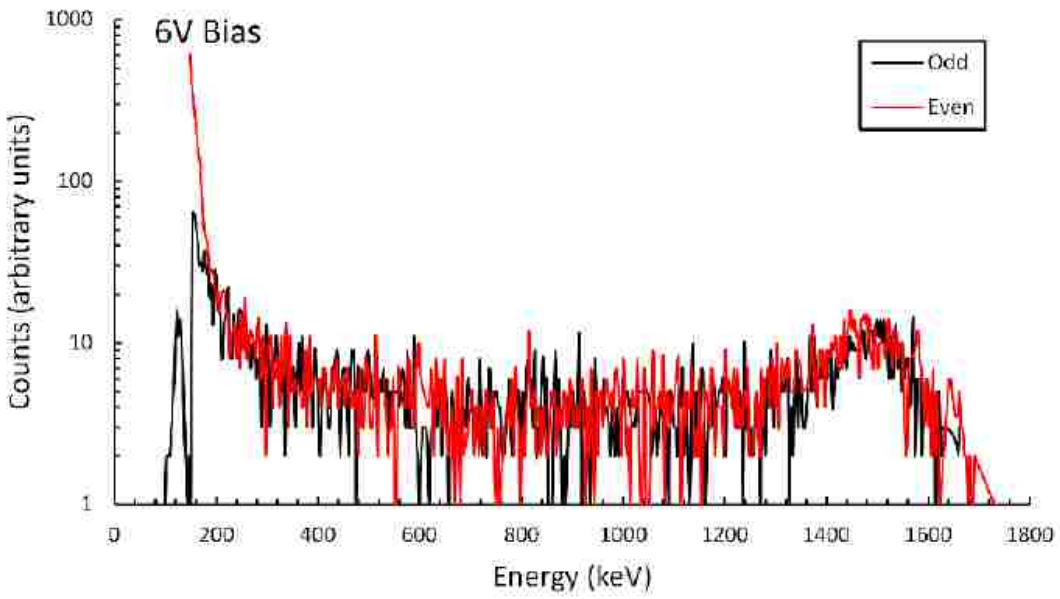

Figure 3.20: ^{241}Am spectrum acquired at UOW with the 18 µm cylindrical array on "LSU 6" with a bias voltage of 6 V (Tran & Chartier, 2014).

3.2.6 Monte Carlo Uncertainties

The calculation of lineal energy in the MC simulations contained two main sources of uncertainty. The first is the underlying uncertainty in the stopping power data used to determine energy deposition. The second is the uncertainty in the SV thickness due to the manufacturing tolerances (the same as affected the experimental calibration). Stopping power uncertainties for the protons in the tissue-substitute case were estimated at 2.0% (ICRU, 1993). The stopping power uncertainties for the alpha particles in the boron case are higher, at 5%, due to the much lower energies possessed by the alpha particles when they enter the SV (<1 MeV), and the subsequent rise in uncertainty for this low-energy region (ICRU, 1993). Total uncertainty for MC simulation of lineal energy is calculated to be 5.4% for the tissue-substitute case, and 7.1% for the boron case (Table 3.5).

Table 3.5: Uncertainties inherent in Monte Carlo calculations of lineal energy for the tissue-substitute and boron converters.

Uncertainty	Value	
	Tissue-Substitute	Boron
Stopping Power Values	2.0%	5.0%
SV Thickness	5.0%	5.0%
Total	5.4%	7.1%

3.2.7 Uncertainty of Absorbed Dose to Silicon

The uncertainties in the calculation of absorbed dose to silicon are chiefly governed by uncertainty in the frequency-mean lineal energy for each spectrum, and the total number of energy deposition events. The uncertainty in frequency-mean lineal energy was found by propagating uncertainties in the values of lineal energy and in the probability density of lineal energy, f(y) (Section 2.2.6). Due to the relatively low number of counts seen experimentally, the uncertainty from the total number of energy deposition events affected the experimental spectra much more than the MC simulations.

The total uncertainties in absorbed dose to silicon (Table 3.6) are calculated to be 6.7% and 5.4% for the tissue-substitute experimental and MC spectra, respectively. For the boron case, the total uncertainties are calculated to be 7.3% and 7.1% for the experimental and MC spectra, respectively.

Table 3.6: Uncertainties in absorbed dose to silicon for the tissue-substitute and boron converters (experimental as well as simulated).

Uncertainty	Value			
	Tissue-Substitute		Boron	
	EXP	MC	EXP	MC
$\bar{y}_F$	6.5%	5.4%	6.9%	7.1%
Number of Events	1.7%	0.4%	2.5%	0.3%
Total	6.7%	5.4%	7.3%	7.1%

3.2.8 Neutron Spectrum Acquisitions

Initial attempts at acquiring a neutron spectrum from the ^{239}PuBe source were hampered by a very low observed count rate, owing to the relatively low activity of the source (2 Ci) and the very small active area of the microdosimeters. To increase the neutron fluence across the device, subsequent attempts involved surrounding the source and the detector with jugs of water (Figure 3.21) to moderate some of the neutrons and to increase neutron albedo towards the device.

With the modified experimental setup, the count rate was still insufficient. As an additional measure to overcome this, calibrated spectra from multiple experiments were combined to improve the counting statistics. Even with these techniques in place, the count rate was still too low for all but the heart endothelial cell shaped SV. So this SV array was the only one used for all further neutron experiments.

Figure 3.21: Experimental setup for increasing the number of detected events when using the ^{239}PuBe neutron source. Detector and source are in middle layer surrounded by ring of water jugs.

Figure 3.22 shows a comparison of the combined experimental spectra (total acquisition time of 83.3 hours) and the corresponding MC simulations. Extrapolation was used for points at low lineal energies due to the electronics noise threshold. The displayed experimental spectrum excludes a few single-count events which appeared at higher lineal energies, above the proton edge. These were excluded in order to make a direct comparison with the MC simulation, which only considers recoil protons, not heavier reaction products, such as alpha particles. Generally good agreement is seen between the two spectra, though the experimental peak shows a slightly higher proportion of lower lineal energy events. Table 3.7 reports results of the two spectra on the basis of frequency-mean lineal energy, dose-mean lineal energy, and absorbed dose to silicon. The percent difference reported for $\bar{y}_F$ fell slightly outside of the combined experimental and MC uncertainties, however the percent differences for $\bar{y}_D$ and D_{Si} were within the combined uncertainties.

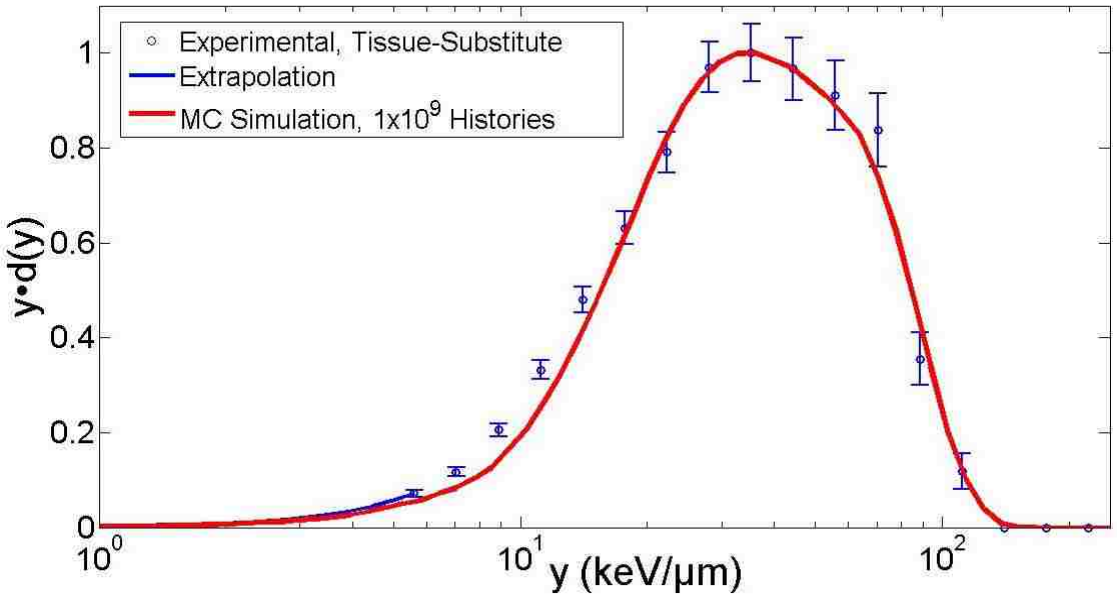

Figure 3.22: Comparison of simulation and experimental data acquired from ^{239}PuBe irradiations using the tissue-substitute converter.

Table 3.7: Values for $\bar{y}_F$, $\bar{y}_D$, and D_{Si} for ^{239}PuBe irradiations using the tissue-substitute converter.

	$\bar{y}_F$ (keV/µm)	Uncert.	$\bar{y}_D$ (keV/µm)	Uncert.	D_{Si} (mGy)	Uncert.
EXP	22.1 ± 1.4	6.5%	38.1 ± 2.7	7.0%	16.9 ± 1.1	6.7%
MC	24.3 ± 1.3	5.4%	39.1 ± 2.2	5.5%	18.5 ± 1.0	5.4%
% Diff.	9.1%		2.6%		8.6%	

Microdosimetric spectra acquired with the boron converter also had a low count rate, so spectra from multiple experiments (total time of 95.5 hours) were combined to produce the microdosimetric spectrum seen in Figure 3.23. The ^{239}PuBe source predominantly emits fast neutrons (defined as having an energy greater than 10 keV), but the surrounding layer of water served to moderate and "thermalize" some of the emitted neutrons, so that they could interact with the boron atoms.

The results from the MC simulation of the boron converter are also plotted for comparison. The two spectra show reasonable agreement in overall shape, though the experimental spectrum again shows a slightly higher proportion of lower lineal energy events. Table 3.8 reports results of the two spectra on the basis of frequency-mean lineal energy, dose-mean lineal energy, and absorbed dose to silicon. All of the percent differences reported were within the combined uncertainties.

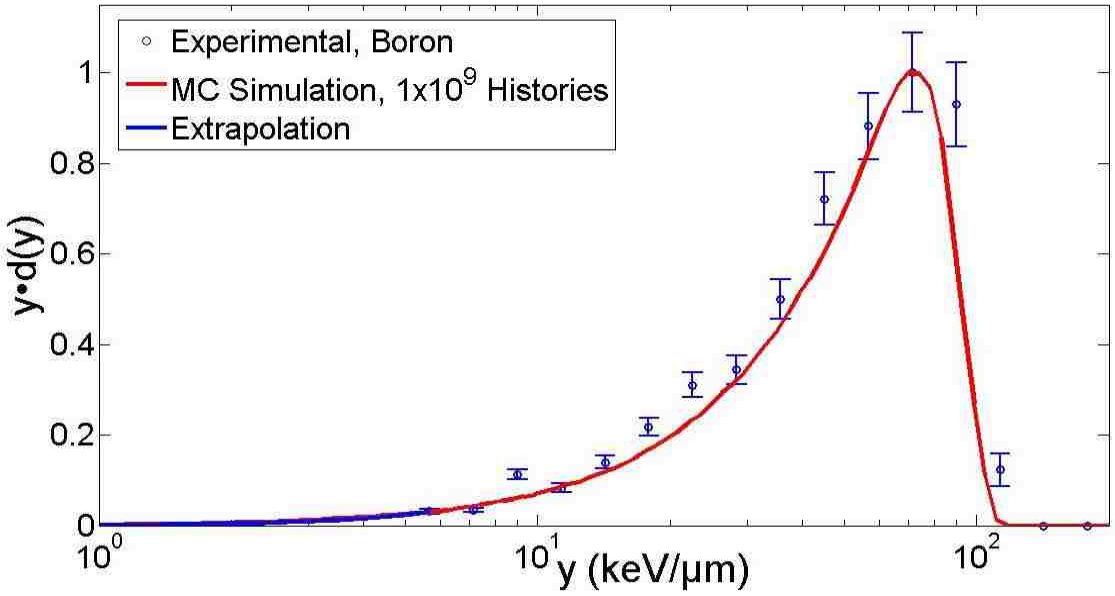

Figure 3.23: Comparison of simulation and experimental data acquired with ^{239}PuBe neutron source with boron converter atop the microdosimeter.

Table 3.8: Values for $\bar{y}_F$, $\bar{y}_D$, and D_{Si} for ^{239}PuBe irradiations using the boron converter.

	$\bar{y}_F$ (keV/µm)	Uncert.	$\bar{y}_D$ (keV/µm)	Uncert.	D_{Si} (mGy)	Uncert.
EXP	30.7 ± 2.1	6.9%	53.3 ± 4.0	7.5%	11.4 ± 0.8	7.3%
MC	29.5 ± 2.1	7.1%	51.3 ± 3.6	7.1%	11.0 ± 0.8	7.1%
% Diff.	4.1%		3.9%		3.6%	

3.2.9 Effect of Noise Threshold

Extrapolation was used to extend the experimental data sets down to low lineal energies - that is, below the typical lower detectability limit of 7.3 keV/µm. However, the effect of the noise threshold was still assessed to judge the relative importance of these low lineal energy events to the overall spectrum. Overlaying the cumulative dose information obtained from the Monte Carlo simulations of the neutron irradiations and the experimental noise threshold gave the fraction of absorbed dose that was missed due to the lower detectability limit. As shown in Figure 3.24, this fraction was found to be 0.026, or 2.6%, of the total dose.

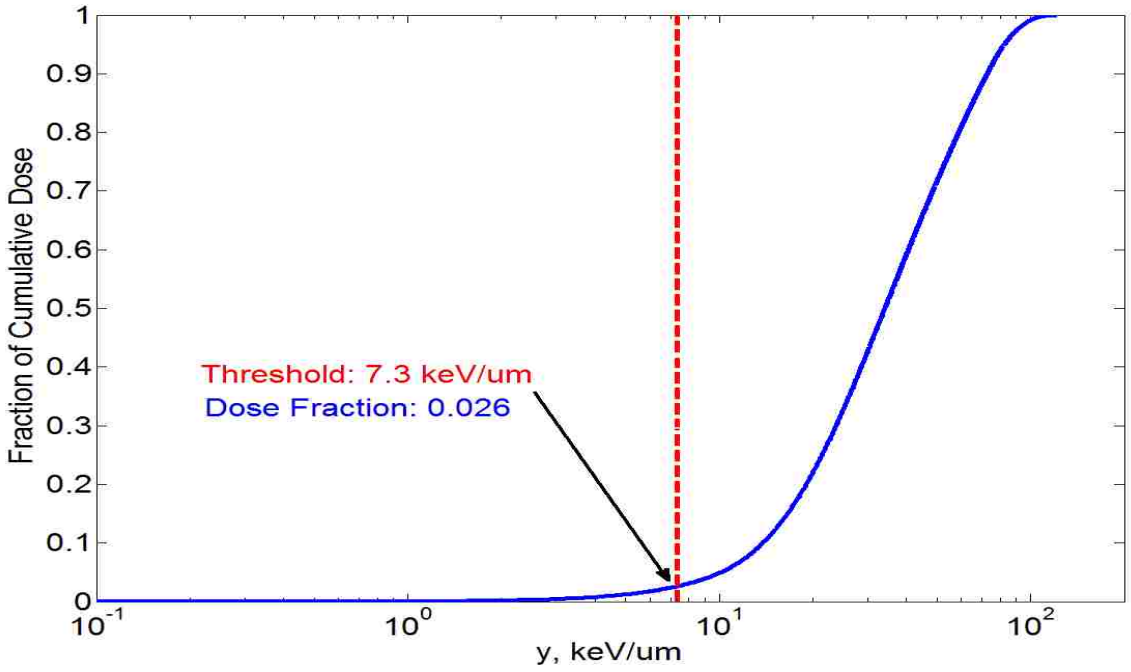

Figure 3.24: Effect of noise threshold in terms of fraction of cumulative absorbed dose for neutron irradiations using the tissue-substitute converter.

3.2.10 Effect of Chord Length Variations

As with the alpha particle simulations (Section 3.1.5), the effect of varying the chord lengths through the SV was also investigated for the neutron experiments. This was achieved by modifying the chord length for each particle history by a normally distributed amount. Figure 3.25 shows the results of the modified tissue-equivalent y•d(y) spectra. The results show that the y•d(y) spectra were fairly insensitive to mean chord length variations, with the spectra still matching well up to a variation of ± 25%. Table 3.9 shows how the modified spectra compare to the unmodified spectrum in terms of $\bar{y}_D$, $\bar{y}_F$, and D_{Si}.

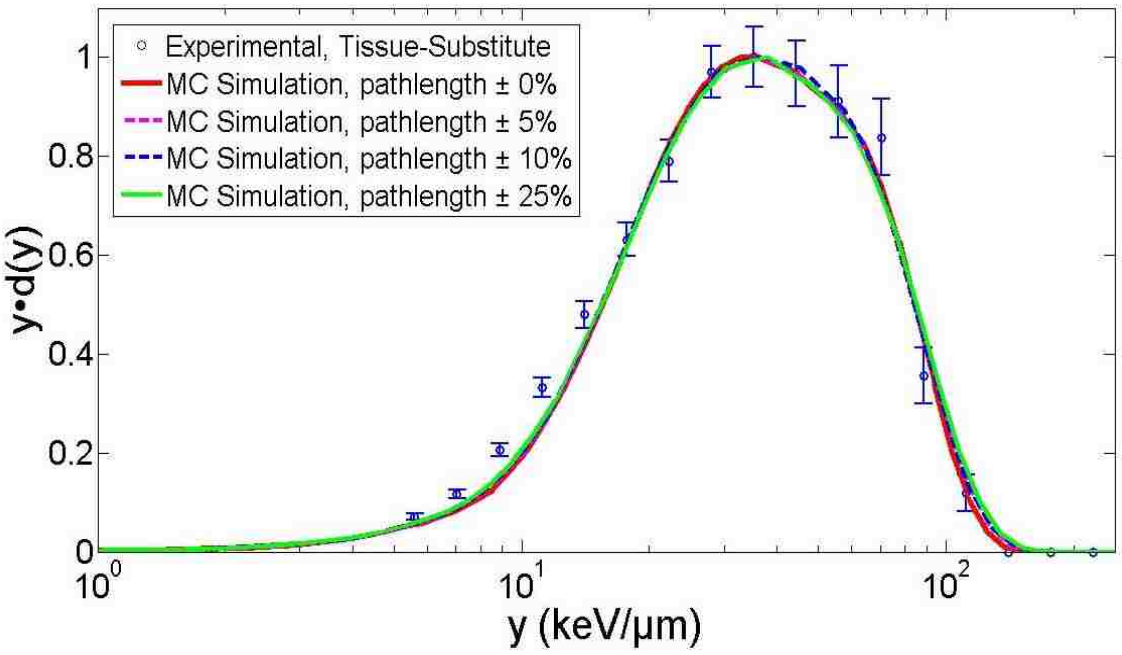

Figure 3.25: Effect of varying the chord lengths in the neutron simulations with the tissue-substitute converter.

Table 3.9: Values for $\bar{y}_D$, $\bar{y}_F$, and D_{Si} for the modified tissue-substitute converter simulations.

	$\bar{y}_F$ (keV/µm)	$\bar{y}_D$ (keV/µm)	D_{Si} (mGy)
MC ± 0 %	24.3 ± 1.3	39.1 ± 2.2	18.5 ± 1.0
MC ± 5 %	24.3 ± 1.3	39.2 ± 2.2	18.5 ± 1.0
%Diff	0.0%	0.3%	0.0%
MC ± 10 %	24.3 ± 1.3	39.1 ± 2.2	18.5 ± 1.0
%Diff	0.0%	0.0%	0.0%
MC ± 25 %	24.2 ± 1.3	39.5 ± 2.2	18.4 ± 1.0
%Diff	0.4%	1.0%	0.5%

The effect of a non-uniform response from each of the sensitive volumes was also investigated for the boron converter experiment. This was accomplished by modifying the simulated chord lengths for each particle history in the same manner as was used for the other setups. Figure 3.26 shows the results of the modified y•d(y) spectra when using the boron converter. The modified boron y•d(y) spectra were more sensitive to the chord length variations than the modified tissue-substitute spectra. However, they were much less sensitive than the modified alpha particle spectra. The left hand side of the simulated and experimental peaks were in better agreement with the modified chord lengths, but agreement on the right hand side did not improve. Table 3.10 shows the results in terms of $\bar{y}_D$, $\bar{y}_F$, and D_{Si}.

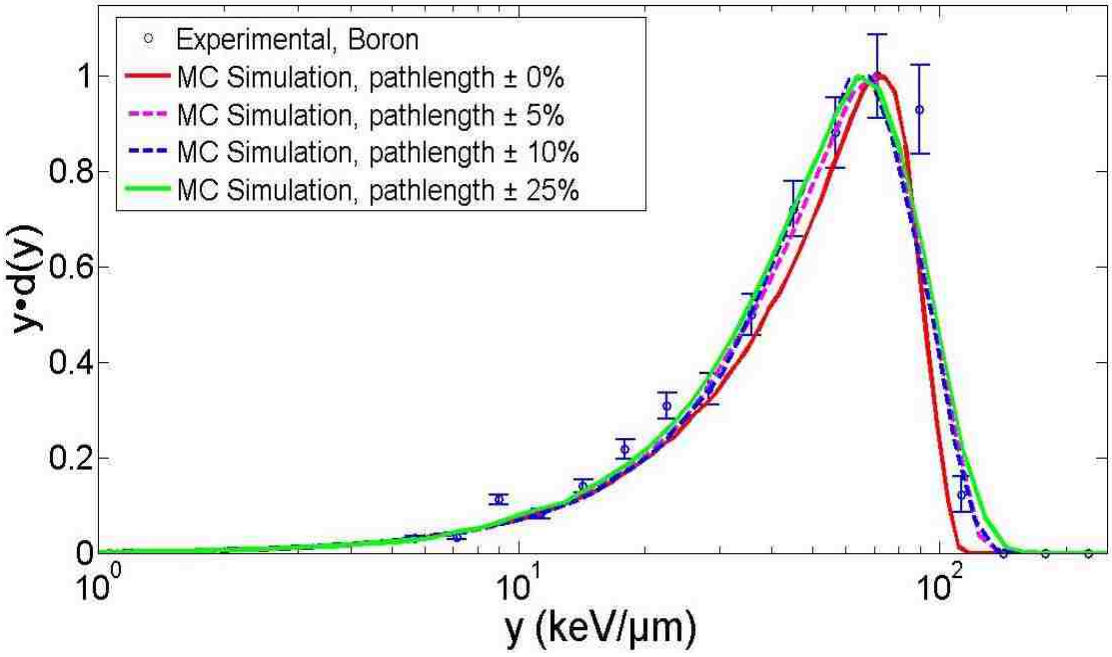

Figure 3.26: Effect of varying the chord lengths for the neutron simulations with the Boron converter.

Table 3.10: Values for $\bar{y}_D$, $\bar{y}_F$, and D_{Si} for the modified boron converter simulations.

	$\bar{y}_F$ (keV/µm)	$\bar{y}_D$ (keV/µm)	D_{Si} (mGy)
MC ± 0 %	29.5 ± 1.5	51.3 ± 2.6	11.5 ± 0.6
MC ± 5 %	31.4 ± 2.2	52.5 ± 3.7	11.7 ± 0.8
%Diff	6.4%	2.3%	1.7%
MC ± 10 %	31.4 ± 2.2	52.8 ± 3.7	11.7 ± 0.8
%Diff	6.4%	2.9%	1.7%
MC ± 25 %	31.3 ± 2.2	53.0 ± 3.8	11.6 ± 0.8
%Diff	6.1%	3.3%	0.9%

3.3 Specific Aim 3

3.3.1 Silicon to Tissue Absorbed Dose Conversion Factor

An absorbed dose conversion factor, $r_{Si,T,}$ was calculated independently for the tissue-substitute and the boron converter cases, using the particle energy spectra extracted from the MC simulations. The "slowing-down" energy spectra were used, which represents the energies of the particles after traversing any intervening materials (the converter itself, air gap, and SiO_2 layer atop the microdosimeter), but before entering the SV. Even over the narrow range of energies in each spectrum, the mass stopping power values for each material varied by a large amount, as seen in Figure 3.27 for the alpha particles emitted from the boron converter.

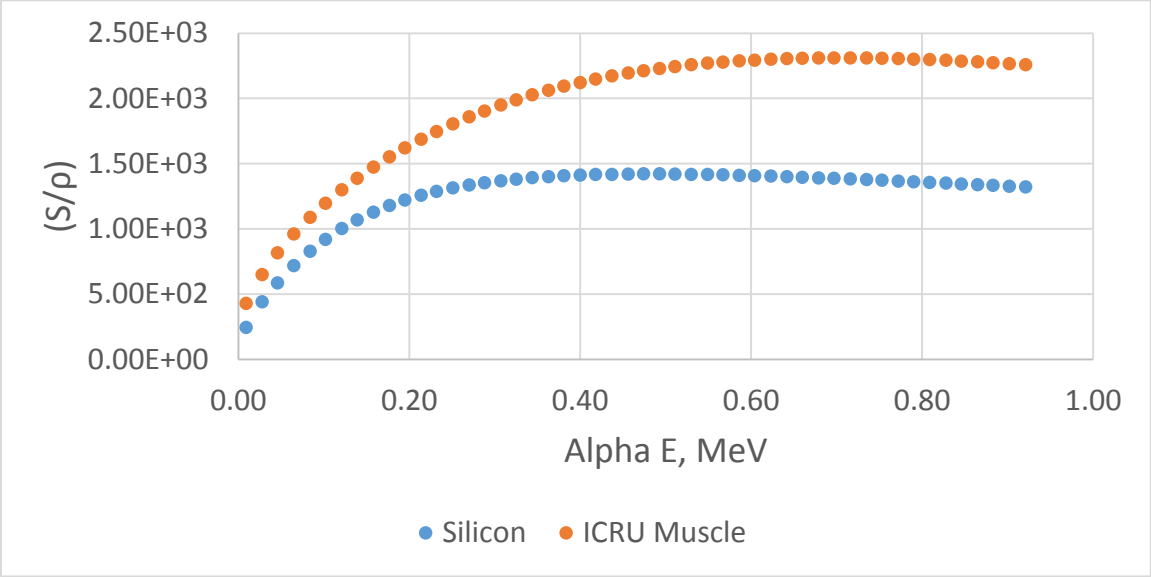

Figure 3.27: Mass stopping power values for silicon and ICRU muscle per energy bin for the alpha particles emitted from the boron converter. Note that this is the "slowing-down" spectrum of energies – taking into account energy loss in the materials upstream of the SVs.

To determine an absorbed dose conversion factor representative of the majority of the particles in each spectra, a reduced spectrum of particle energies was considered, which represented the mean of the spectrum, plus or minus one sigma (Figure 3.28). Only stopping power values from within this reduced spectrum were considered when calculating the absorbed dose conversion factor. The uncertainty in $r_{Si,T}$ was calculated as the maximum deviation (within the reduced spectrum) from the fluence-weighted ratio. Table 3.11 lists the energy, mass stopping power, and ratio values for the full and reduced spectra in the boron converter case; the same process was repeated for the protons in the tissue-substitute case. The calculated values of $r_{Si,T}$ for the tissue-substitute and boron cases are reported in Table 3.12, along with the corresponding uncertainty values.

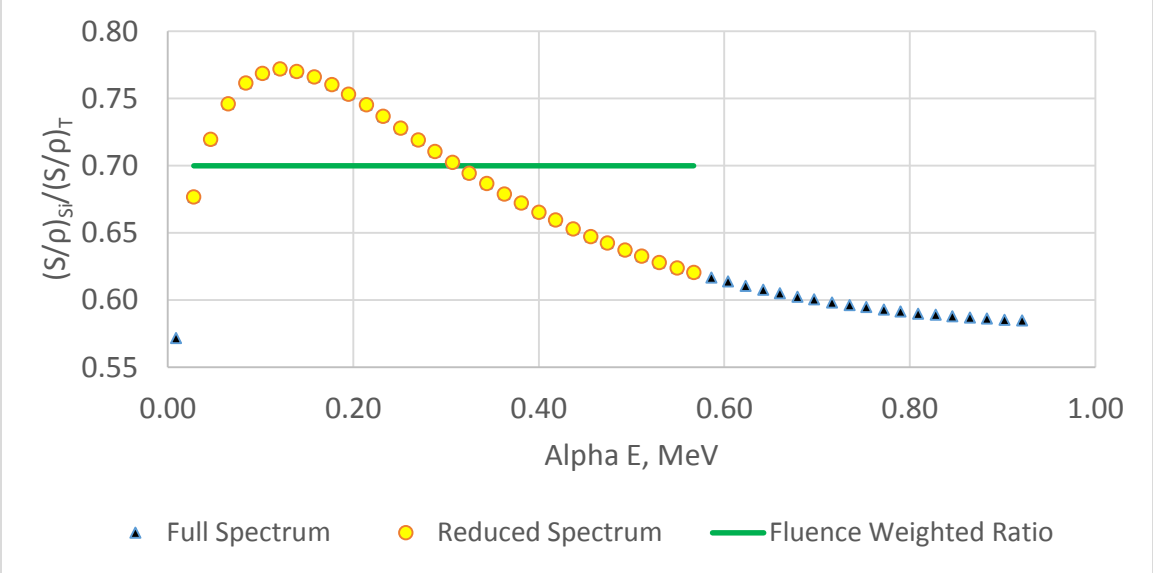

Figure 3.28: Variation of silicon-to-tissue stopping power ratio with respect to alpha particle energy.

Table 3.11: Stopping power values of alpha particles in ICRU Muscle and Silicon. The particle energies considered represents the slowing-down spectrum of alpha particles from the boron converter, before entering the SVs of the microdosimeter. Yellow shading represents the "reduced spectrum," as shown in Figure 3.28.

	Silicon	ICRU Muscle, Striated		
Kinetic Energy, (MeV)	Mass Stopping Power (MeV cm^2/g)	Mass Stopping Power (MeV cm^2/g)	Stopping Power Ratio $(S/\rho)_{Si}/(S/\rho)_T$	%Diff from $r_{Si,T}$
0.01	245	428.5	0.57	18.6%
0.03	440.2	650.5	0.68	2.9%
0.05	586.8	815.5	0.72	2.9%
0.07	717.6	961.9	0.75	7.1%
0.08	829.2	1089	0.76	8.6%
0.10	920.2	1197	0.77	10.0%
0.12	1003	1299	0.77	10.0%
0.14	1069	1388	0.77	10.0%
0.16	1129	1474	0.77	10.0%
0.18	1180	1552	0.76	8.6%
0.20	1221	1621	0.75	7.1%
0.21	1258	1688	0.75	7.1%
0.23	1287	1747	0.74	5.7%
0.25	1314	1805	0.73	4.3%
0.27	1336	1858	0.72	2.9%
0.29	1353	1904	0.71	1.4%
0.31	1369	1949	0.70	0.0%
0.33	1381	1989	0.69	1.4%
0.34	1392	2027	0.69	1.4%
0.36	1400	2062	0.68	2.9%
0.38	1407	2093	0.67	4.3%
0.40	1412	2122	0.67	4.3%
0.42	1416	2147	0.66	5.7%
0.44	1418	2172	0.65	7.1%
0.46	1420	2194	0.65	7.1%
0.47	1421	2212	0.64	8.6%
0.49	1421	2230	0.64	8.6%
0.51	1420	2244	0.63	10.0%
0.53	1418	2258	0.63	10.0%
0.55	1416	2270	0.62	11.4%
0.57	1414	2279	0.62	11.4%
0.59	1411	2288	0.62	11.4%

(Table 3.11 continued)

	Silicon	ICRU Muscle, Striated		
Kinetic Energy, (MeV)	Mass Stopping Power (MeV cm^2/g)	Mass Stopping Power (MeV cm^2/g)	Stopping Power Ratio $(S/\rho)_{Si}/(S/\rho)_T$	%Diff from $r_{Si,T}$
0.60	1408	2294	0.61	12.9%
0.62	1404	2300	0.61	12.9%
0.64	1400	2304	0.61	12.9%
0.66	1396	2307	0.61	12.9%
0.68	1391	2309	0.60	14.3%
0.70	1387	2310	0.60	14.3%
0.72	1382	2310	0.60	14.3%
0.74	1377	2309	0.60	14.3%
0.75	1372	2307	0.59	15.7%
0.77	1366	2304	0.59	15.7%
0.79	1361	2301	0.59	15.7%
0.81	1355	2297	0.59	15.7%
0.83	1350	2292	0.59	15.7%
0.85	1344	2286	0.59	15.7%
0.87	1338	2280	0.59	15.7%
0.88	1333	2274	0.59	15.7%
0.90	1327	2267	0.59	15.7%
0.92	1321	2259	0.58	17.1%

Table 3.12: Absorbed dose conversion factor values for tissue-substitute and boron cases, with uncertainties.

	$r_{Si,T}$	Uncert.
Tissue-Substitute EXP	0.71 ± 0.03	4.2%
Tissue-Substitute MC		
Boron EXP	0.70 ± 0.08	11.4%
Boron MC		

Applying the absorbed dose conversion factors from Table 3.12 to the values of absorbed dose to silicon reported in Section 3.2.8 gives the calculated values of absorbed

dose to tissue reported in Table 3.13 (tissue-substitute case) and Table 3.14 (boron case). The percent differences for both cases were within the combined uncertainties. The reported uncertainties were calculated by propagating the uncertainties in absorbed dose to silicon and the uncertainties in the absorbed dose conversion factor.

Table 3.13: Experimental and simulated absorbed dose to tissue values for the tissue-substitute case.

	D_T (mGy)	Uncert.
TE EXP	24.5 ± 1.9	7.9%
TE MC	26.8 ± 1.8	6.9%
% Diff	8.6%	

Table 3.14: Experimental and simulated absorbed dose to tissue values for the boron case.

	D_T (mGy)	Uncert.
Boron EXP	18.1 ± 2.2	13.5%
Boron MC	17.5 ± 2.2	13.4%
%Diff	3.4%	

3.3.2 Dose Equivalent Conversion

The average quality factor value for each spectrum, $\bar{Q}$, was calculated using the equation defined by the ICRU (1986). The values of the average quality factor for each experimental and simulated case are reported in Table 3.15. Conversion from absorbed dose to tissue to dose equivalent was then accomplished by multiplying each value of absorbed dose to tissue by the corresponding average quality factor value. The calculated values of dose equivalent are reported in Table 3.16 (tissue-substitute case)

and Table 3.17 (boron case). The reported dose equivalent values for each case were within the uncertainties. Note that the reported uncertainties are the same as for the respective absorbed dose to tissue values, since no additional uncertainties in the quality factor were considered.

Table 3.15: Values of $\bar{Q}$, as calculated from the experimental and simulated spectra.

	$\bar{Q}$
Tissue-Substitute EXP	11.4
Tissue-Substitute MC	11.7
Boron EXP	15.8
Boron MC	15.4

Table 3.16: Experimental and simulated dose equivalent values for the tissue-substitute case.

	H (mSv)	Uncert.
Tissue-Substitute EXP	279.3 ± 23.2	7.9%
Tissue-Substitute MC	313.6 ± 21.6	6.9%
% Diff	10.9%	

Table 3.17: Experimental and simulated dose equivalent values for the boron case.

	H (mSv)	Uncert.
Boron EXP	286.0 ± 38.6	13.5%
Boron MC	269.5 ± 36.1	13.4%
% Diff	6.1%	

4 DISCUSSION

4.1 Summary of Results

This study tested the feasibility of using silicon on insulator microdosimeters which mimic the size and shape of particular cells within the human body. The microdosimeters were first analyzed in terms of their physical surface conditions and basic diode characteristics, to select the best candidates for further measurements. Using the microdosimeters, spectra were acquired with two ^{241}Am alpha particle sources and a ^{239}PuBe neutron source. The neutron source experiments were performed with two different converter layers placed atop the microdosimeter: a tissue-substitute converter made from high-density polyethylene, and a boron converter made from epoxy and a thin layer of boron powder. For each of the two converters, measurements were made of lineal energy and absorbed dose to silicon. Absorbed dose to silicon was then converter to absorbed dose to tissue using an absorbed dose conversion factor - calculated based on the ratio of stopping power values for silicon and tissue. Dose equivalent was then determined, using an average quality factor calculated for each spectrum on the basis of the ICRU definition (1986). The uncertainties at each step were quantified to determine if the overall uncertainty in dose equivalent would be less than 10%, as hypothesized.

The experimental data was also compared with Monte Carlo simulation data, using an in-house code. To test the accuracy of the in-house code, it was compared with GEANT4 simulations, data from the TRIM code, and results derived analytically for an infinite slab geometry. Generally good agreement was seen between the experimental and simulated data. However, the experimental data consistently displayed a higher proportion of low lineal energy events compared to the simulations.

4.2 Response to Hypothesis

With the tissue-substitute converter placed atop the cell-shaped microdosimeters, dose equivalent was determined with 7.9% uncertainty, which supported the hypothesis. However, with the boron converter, the hypothesis was not supported, with dose equivalent determined with 13.5% uncertainty. These uncertainty values are comparable to a typical TEPC uncertainty, which varies from ~6% (Burmeister et al., 2001) up to 10-15% (Autischer et al., 2005; Tarzia & Rashidifard, 2013).

4.3 Recommendations

There were some compromises made in the manufacturing of the silicon microdosimeters used in this project, due to the tight time constraints of the supporting grant. These compromises were: 1. Use of a silicon wafer with lower than specified resistivity – leading to elevated levels of leakage current across the microdosimeters, and 2. Re-wiring of the chips in the package – leading to obstruction of some of the SVs and increasing the potential of shorting out an array and creating a non-functioning microdosimeter. Correcting these issues in the next generation of cell-shaped microdosimeters should significantly improve their performance. Further testing should also be performed to better understand the charge collection characteristics of the unique SV shapes.

Another limiting factor was the very small active area of each array. Since each array was constructed with a different SV design, signal was only collected from one array at a time. This limited the observed count rate and required long acquisition times to generate a sufficient amount of signal when using the neutron source. These acquisition times (3-4 days) are impractical for anything except laboratory testing. To improve the

count rate of the device, all four arrays on the chip could be made with the same SV design, thus increasing by a factor of four the active area usable at any particular time.

The layout of the circuit board, upon which the microdosimeter was mounted, is another area that can be improved. Use of more solid connectors, surface-mounted devices, and better shielding for data connections will improve overall circuit design and reduce the amount of noise in the electronics.

4.4 Limitations of This Study

This study was only performed with isotopic alpha particle and neutron source irradiations, neither of which are very relevant for clinical applications. Use of a reference neutron source at a standards laboratory would provide an absolute dose measurement against which the experimental measurements could be better compared. The small active area of the device, and subsequently low observed count rate, limited the type of experiments that could be performed – excluding for instance, use of the microdosimeters at depth within a phantom. The relatively large overall size of the prototype device was also a factor limiting the choice of experimental setups.

4.5 Future Work

Once future generations of the microdosimeters have been produced, which possess the improvements previously mentioned, further testing should be done using a clinical proton beam or with a selection of heavy charged particles (C, Fe, He, etc.) to test the microdosimeters with a range of ion species. With a more intense beam and a smaller device, measurements could then be performed within an anthropomorphic phantom. Placement of the cell-shaped microdosimeter at the location within the phantom where those cells would physically reside would allow for measuring cell-specific doses for particular radiotherapy treatment setups. This type of detector has the advantages of

being small, lightweight, and simple to produce. It is also less complicated to set up and maintain than a tissue-equivalent proportional counter. The end goal for this device is a dosimeter that provides better radiation monitoring for patients and staff.

4.6 Conclusions

This study tested the feasibility of silicon on insulator microdosimeters which were constructed with sensitive volumes that mimic the size and shape of cells within the human body. As a proof of concept, we have demonstrated that this device is capable (depending on the type of converter layer used) of determining dose equivalent with overall uncertainties less than 10% when irradiated with a ^{239}PuBe neutron source. The experimental data also agreed well with results from Monte Carlo simulations.

Low source activity and a small active area on the microdosimeter led to rather low observed count rates during measurements, requiring very long acquisition times to generate sufficient signal from the device. Higher than expected levels of leakage current across the silicon chips and noise in the signal processing electronics led to a lower detectability limit of approximately 7 keV/μm, which is much higher than the 0.4 keV/μm previously demonstrated using silicon microdosimeters (Bradley et al., 2001). There was also evidence of charge sharing across the device, which inflated the number of low energy deposition events in the recorded spectra. Overall, the microdosimeter was found to be feasible for further testing, though some specific improvements have been identified (discussed in Section 4.3) that should expand both its usefulness and robustness.

5 REFERENCES

Ainsbury, E. A., Bouffler, S. D., Dorr, W., Graw, J., Muirhead, C. R., Edwards, A. A., & Cooper, J. (2009). Radiation cataractogenesis: a review of recent studies. *Radiat Res, 172*(1), 1-9.

Augusteyn, R. C. (2010). On the growth and internal structure of the human lens. *Exp Eye Res, 90*(6), 643-654.

Autischer, M., Beck, P., Latocha, M., & Rollet, S. (2005, April 17-21). *Simulation of TEPC response to cosmic radiation during dedicated flight campaign.* Paper presented at the American Nuclear Society Monte Carlo Topical Meeting, Chattanooga, TN.

Baker, J. E., Moulder, J. E., & Hopewell, J. W. (2011). Radiation as a risk factor for cardiovascular disease. *Antioxid Redox Signal, 15*(7), 1945-1956.

The Basics of Boron Neutron Capture Therapy. (2005, 03/23). Retrieved 07/11/2014, from http://web.mit.edu/nrl/www/bnct/info/description/description.html.

Bertolini, G., & Coche, A. (1968). *Semiconductor Detectors*. North Holland, Amsterdam: Elsevier.

Blakely, E. A. (2012). Lauriston S. Taylor Lecture on Radiation Protection and Measurements: What Makes Particle Radiation so Effective? *Health Phys, 103*(5), 508-528.

Bradley, P. D. (2000). *The Development of a Novel Silicon Microdosimeter for High LET Radiation Therapy*: University of Wollongong, Department of Engineering Physics.

Bradley, P. D., & Rosenfeld, A. (1998). Tissue equivalence correction for silicon microdosimetry detectors in boron neutron capture therapy. *Medical Physics, 25*(11), pp. 2220-2225.

Bradley, P. D., Rosenfeld, A., & Zaider, M. (2001). Solid state microdosimetry. *Nucl Instrum Methods Phys Res B, 184*(1-2), 135-157.

Brown, N. A. P., & Bron, A. J. (1987). An estimate of the human lens epithelial cell size in vivo. *Exp Eye Res, 44*(6), 899-906.

Burmeister, J., Kota, C., & Maughan, R. L. (2001). Miniature tissue-equivalent proportional counters for BNCT and BNCEFNT dosimetry. *Med. Phys., 28*(9), 1911-1925.

Byrne, H. L., McNamara, A. L., Domanova, W., Guatelli, S., & Kuncic, Z. (2013). Radiation damage on sub-cellular scales: beyond DNA. *Phys Med Biol, 58*(5), 1251-1267.

Cooper, K., Gates, P., Rae, J. L., & Dewey, J. (1990). Electrophysiology of cultured human lens epithelial cells. *J Membr Biol, 117*(3), 285-298.

Dunn, W. L., & Shultis, J. K. (2011). *Exploring Monte Carlo Methods*: Elsevier Science.

Evans, T. C., Richards, R. D., & Riley, E. F. (1960). Histologic Studies of Neutron and X-Irradiated Mouse Lenses. *Radiat Res, 13*(5), 737-750.

Farahmand, M. (2004). A Novel Tissue-Equivalent Proportional Counter based on a Gas Electron Multiplier: Delft University Press 2004-06-15.

Feng, L., Stern, D. M., & Pile-Spellman, J. (1999). Human endothelium: endovascular biopsy and molecular analysis. *Radiology, 212*(3), 655-664.

Garipcan, B., Maenz, S., Pham, T., Settmacher, U., Jandt, K. D., Zanow, J., & Bossert, J. (2011). Image Analysis of Endothelial Microstructure and Endothelial Cell Dimensions of Human Arteries - A Preliminary Study. *Advanced Engineering Materials, 13*(1-2), B54-B57.

Graw, J. (2003). The genetic and molecular basis of congenital eye defects. *Nat Rev Genet, 4*(11), 876-888.

Harvey, Z. R. (2008). *Neutron Flux and Energy Characterization of a Plutonium-Beryllium Isotopic Neutron Source by Monte Carlo Simulation with Verification by Neutron Activation Analysis.* Purdue University.

Hu, N. (2013). *Silicon-on-Insulator Microdosimeter for Space Application.* (Master of Science - Research Thesis), University of Wollongong.

ICRU. (1983). Microdosimetry (Report 36). International Commission on Radiation Units and Measurements, Bethesda, MD.

ICRU. (1986). The Quality Factor in Radiation Protection (Report 40). International Commission on Radiation Units and Measurements, Bethesda, MD.

ICRU. (1993). Stopping Powers and Ranges for Protons and Alpha Particles (Report 49). International Commission on Radiation Units and Measurements, Bethesda, MD.

Jaeger, R. C., & Blalock, T. N. (2008). *Microelectronic Circuit Design* (Third ed.). New York: McGraw-Hill.

Kellerer, A. M. (1971a). Considerations on the Random Traversal of Convex Bodies and Solutions for General Cylinders. *Radiat Res, 47*(2), 359-376.

Kellerer, A. M. (1971b). Event Simultaneity in Cavities: Theory of the Distortions of Energy Deposition in Proportional Counters. *Radiat Res, 48*(2), 216-233.

Knoll, G. F. (2000). *Radiation Detection and Measurement* (Third ed.). Ann Arbor, MI: John Wiley & Sons, Inc.

Malek, A. M., & Izumo, S. (1996). Mechanism of endothelial cell shape change and cytoskeletal remodeling in response to fluid shear stress. *J Cell Sci, 109*(4), 713-726.

Masters, B. R., Vrensen, G. F., Willekens, B., & van Marle, J. (1997). Confocal light microscopy and scanning electron microscopy of the human eye lens. *Exp Eye Res, 64*(3), 371-377.

McGeachie, J. (1998). Blue Histology - Vascular System, More About Endothelial Cells. Retrieved 08/27/2013, from http://www.lab.anhb.uwa.edu.au/mb140/moreabout/endothel.htm.

Neudeck, G. W. (1989). *The PN Junction Diode* (2d ed.). Upper Saddle River, NJ: Pearson Education.

Newhauser, W. (1995). *Neutron Kerma Factor Measurements in the 25-MeV to 85-MeV Neutron Energy Range.* (Doctor of Philosophy (Medical Physics)), University of Wisconsin-Madison.

Ng, K. K. (2002). *Complete Guide to Semiconductor Devices* (Second ed.). New York: John Wiley & Sons, Inc.

Ohashi, T., & Sato, M. (2005). Remodeling of vascular endothelial cells exposed to fluid shear stress: experimental and numerical approach. *Fluid Dyn Res, 37*(1), 40-59.

Otake, M., & Schull, W. J. (1991). A review of forty-five years study of Hiroshima and Nagasaki atomic bomb survivors. Radiation cataract. *J Radiat Res, 32 Suppl*, 283-293.

Pisacane, V. L., Dolecek, Q. E., Malak, H., Cucinotta, F. A., Zaider, M., Rosenfeld, A. B., . . . Dicello, J. F. (2011). Microdosemeter instrument (MIDN) for assessing risk in space. *Radiat Prot Dosimetry, 143*(2-4), 398-401.

Pisacane, V. L., Rosenfeld, A. B., Dolecek, Q. E., Dicello, J. F., Malak, H., Zaider, M., & Ziegler, J. F. (2013). *The Science of Micro Dosimetry* (J. F. Ziegler Ed. First ed.). US Naval Academy.

Pospisil, S., & Granja, C. (2009). *Neutrons and their Detection with Silicon Diodes.* Paper presented at the Nuclear Physics Methods and Accelerators in Biology and Medicine, Fifth International Summer School.

Potter, C. M. F., Schobesberger, S., Lundberg, M. H., Weinberg, P. D., Mitchell, J. A., & Gorelik, J. (2012). Shape and Compliance of Endothelial Cells after Shear Stress In Vitro or from Different Aortic Regions: Scanning Ion Conductance Microscopy Study. *PLoS ONE, 7*(2), 1-5.

Records, R. E. (1979). *Physiology of the human eye and visual system*. Hagerstown, MD: Harper & Row.

Reinhard, M. I., Cornelius, I., Prokopovich, D. A., Wroe, A., Rosenfeld, A. B., Pisacane, V., . . . Dicello, J. F. (2005). Response of a SOI Microdosimeter to 238PuBe Neutron Source. *Nuclear Science Symposium Conference Record, 2005 IEEE, Vol. 1*(October), pp. 68-72.

Robman, L., & Taylor, H. (2005). External factors in the development of cataract. *Eye (Lond), 19*(10), 1074-1082.

Rossi, H. H., & Rosenzweig, W. (1955). A device for the measurement of dose as a function of specific ionization. *Radiology, 64*(3), 404-411.

Rozenfeld, A. (2011). Advanced Semiconductor Dosimetry in Radiation Therapy. *AIP Conference Proceedings, 1345*(1), 48-74.

Rozenfeld, A. (2013). [MIDN-4 Technical Process Notes].

Schrewe, U. J., Brede, H. J., & Dietze, G. (1989). Dosimetry in mixed neutron-photon fields with tissue-equivalent proportional counters. *Radiat. Prot. Dosim., 29*(1/2), 41-45.

Shiraishi, F. (1969). Performance deterioration of surface barrier detectors by fission fraggment bombardment. *Nuclear Instruments and Methods, 69*(2), 316-322.

Stewart, S., Duncan, G., Marcantonio, J. M., & Prescott, A. R. (1988). Membrane and communication properties of tissue cultured human lens epithelial cells. *Investigative Ophthalmology & Visual Science, 29*(11), 1713-1725.

Sumagin, R., Brown, C. W., 3rd, Sarelius, I. H., & King, M. R. (2008). Microvascular endothelial cells exhibit optimal aspect ratio for minimizing flow resistance. *Ann Biomed Eng, 36*(4), 580-585.

Tarzia, J. P., & Rashidifard, N. B. (2013, June 5, 2013). *Dose Equivalent Characterization of a 1 Ci Americium-Beryllium Neutron Calibration Source.* Paper presented at the 32nd International Dosimetry and Records Symposium, Scottsdale, Arizona.

Thiriet, M. (2007). *Biology and Mechanics of Blood Flows: Part II: Mechanics and Medical Aspects*: Springer.

Tran, L., & Chartier, L. (2014). *Preliminary Characterisation of Fourth Generation Microdosimeter from the University of Florida*. Internal Report. Centre for Medical Radiation Physics at the University of Wollongong.

Wunstorf, R. (1997). Radiation hardness of silicon detectors: current status. *Nuclear Science, IEEE Transactions on, 44*(3), 806-814.

Yanoff, M., Duker, J. S., & Augsburger, J. J. (2009). *Ophthalmology*. London: Mosby Elsevier.

Yusuf, S. W., Sami, S., & Daher, I. N. (2011). Radiation-induced heart disease: a clinical update. *Cardiol Res Pract, 2011*, 9.

Zeghbroeck, V. (2007). *Principles of Semiconductor Devices and Heterojunctions*: Prentice Hall PTR.

Ziebell, A. L., Lim, W. H., Reinhard, M. I., Cornelius, I., Prokopovich, D. A., Siegele, R., . . . Rosenfeld, A. B. (2008). A Cylindrical Silicon-on-Insulator Microdosimeter: Charge Collection Characteristics. *IEEE Transactions on Nuclear Science, 55*(6), 3414-3420.

Ziegler, J. F. (2013). [Quad Multichannel Dosimeter Manual].

6 APPENDIX

6.1 Circuit Board Schematic

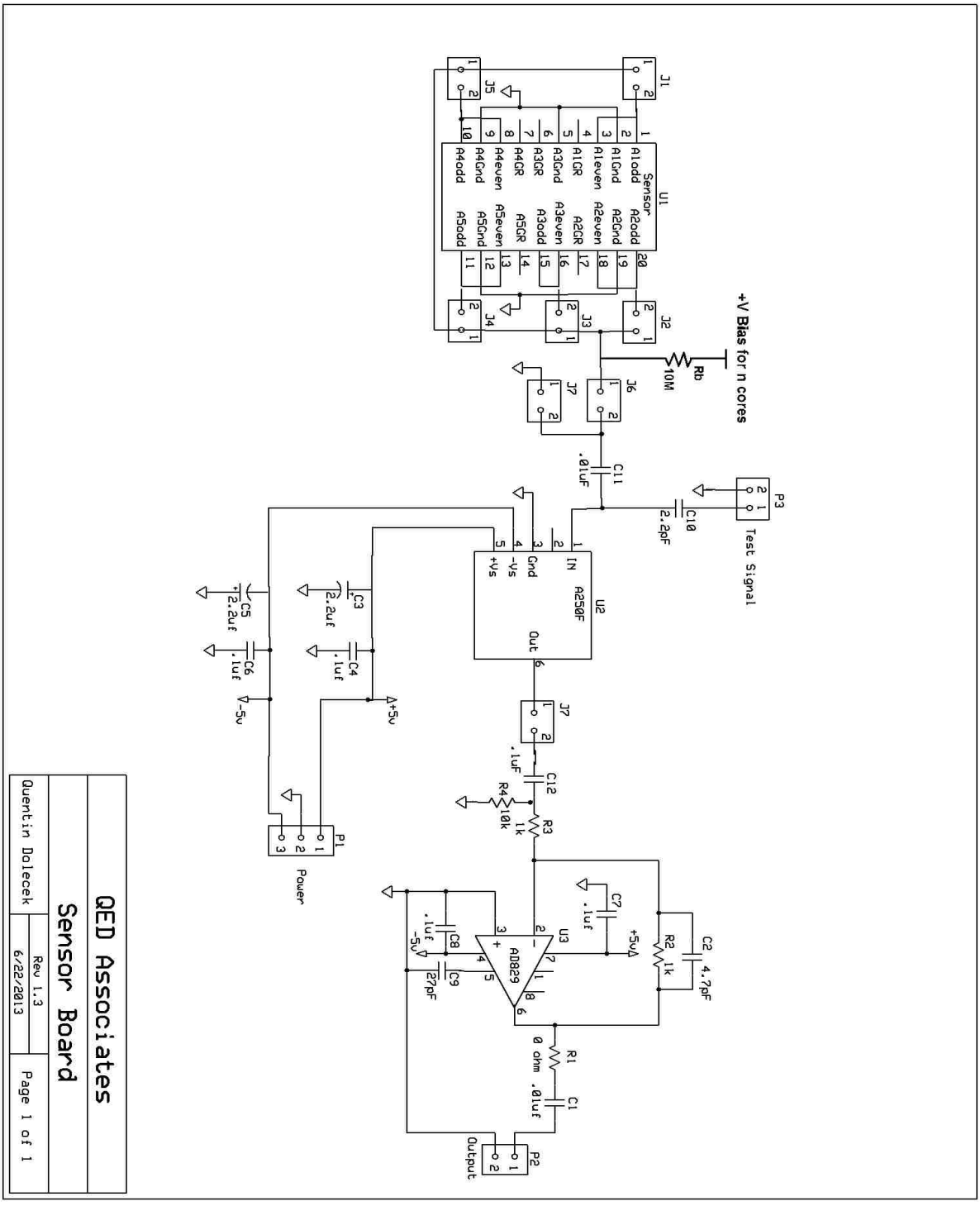

Figure 6.1: Electronics schematic - modified for application of bias voltage. Adapted from original schematic (Quentin Dolecek, personal communication, October 28, 2013).

6.2 Calibration Worksheet

	A	B	C	D	E	F
1	Date	6/12/2014	Time	11:54 AM	Experimente	TM
2	Board #	2				
3	**Alpha Calibration**					
4	Source	Source 2				
5	Mean Energy	4.674	MeV			
6	Temp	73	F			
7	Bias	2	V			
8	Chip #	13				
9	Array #	2				
10	**Pulser Calibrations**					
11	**Frequency**	90	Hz			
12	**Gain**	1x	4.3x	11x	34x	
13	Pulse Height	h	h	h	h	
14	1					
15	0.5	211	877			
16	0.2	103	416			
17	0.1	57	220	549		
18	0.05	32	112	280	860	
19	0.02		45	115	364	
20	0.01			56	198	
21	0.005				113	
22						
23	**Gain**	1x	4.3x	11x	34x	
24	m	0.0025	0.0005	0.0002	0.0001	
25	b	-0.0435	-0.0040	-0.0008	-0.0019	
26						
27	href	43				
28	yref	193.09	kev/um of a peak			
29	Pref	0.06579				
30	alpha	-127.531	-11.627	-2.263	-5.564	kev/um
31	beta	7.456	1.428	0.537	0.177	
32						
33	ADC lld	20	37	49	70	
34	ADC uld	900	Ch			
35	ymin	21.60	41.21	24.07	6.83	keV/um
36	ymax	6583.19	1273.65	481.36	153.76	keV/um

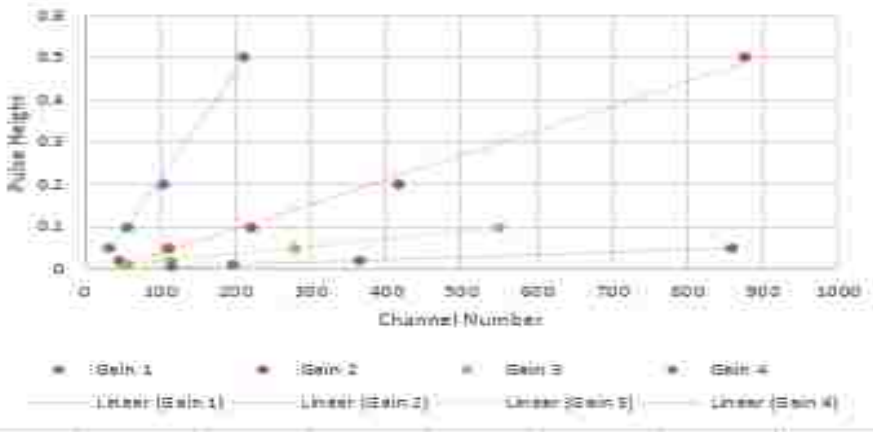

Figure 6.2: Sample calibration worksheet.

6.3 Results of LSU Leakage Current Measurements

Table 6.1: Reverse bias voltages before 0.5 µA leakage current limit was reached.

Chip #	Array #	Limiting Voltage (V)	Chip #	Array #	Limiting Voltage (V)
LSU 3	1	1.9	LSU 4	1	3.0
	2	1.4		2	0.5
	4	0.6		4	1.7
	5	0.5		5	1.4
LSU 5	1	5.2	LSU 8	1	1.0
	2	1.8		2	0.7
	4	1.1		4	0.8
	5	2.8		5	1.0
LSU 9	1	1.4	LSU 10	1	2.9
	2	1.3		2	0.9
	4	1.2		4	0.9
	5	1.8		5	1.4
LSU 11	1	2.7	LSU 12	1	3.4
	2	0.6		2	1.8
	4	1.2		4	0.6
	5	3.1		5	3.5
LSU 13	1	4.3	LSU 14	1	2
	2	2.2		2	2.2
	4	1		4	0.5
	5	2.2		5	2.8
LSU 15	1	2	LSU 16	1	4.7
	2	2.2		2	5.0
	4	0.8		4	1.1
	5	2.7		5	4.3
No Array 2	1	8.3	No Array 4	1	0.7
	2	3.4		2	0.5
	4	1.2		4	0.5
	5	0.7		5	2.7
OG 1	1	6.7	OG 2	1	4.0
	2	3.8		2	1.5
	4	3.3		4	0.7
	5	6.1		5	2.5

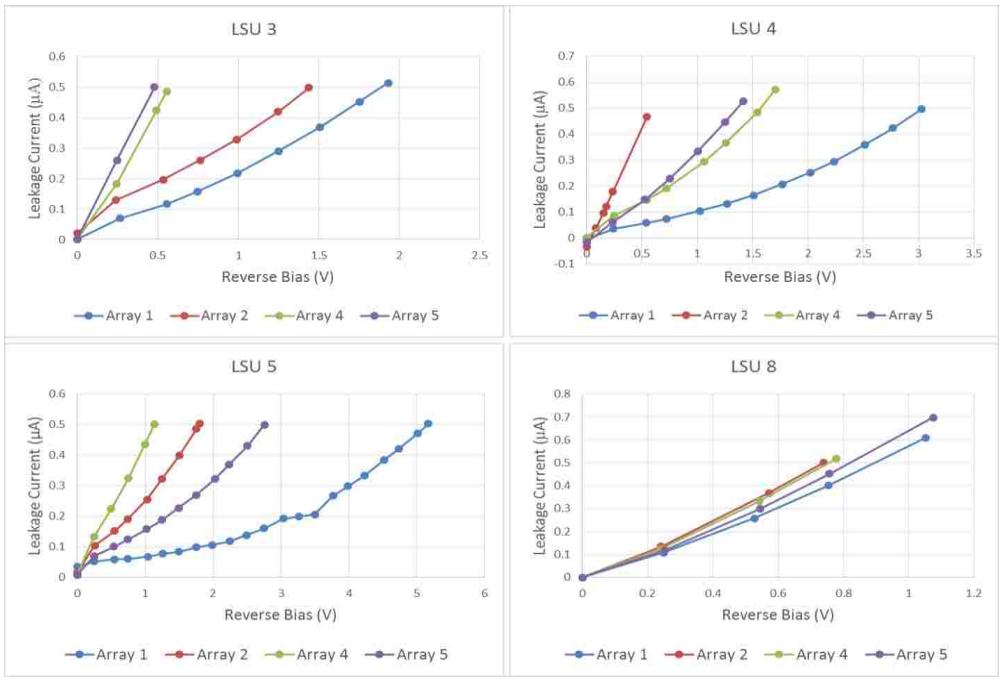

Figure 6.3: LSU I-V plots for chips LSU 3, LSU 4, LSU 5, and LSU 8 (note: LSU 1, LSU 2, LSU 6, and LSU 7 were sent to UOW for testing).

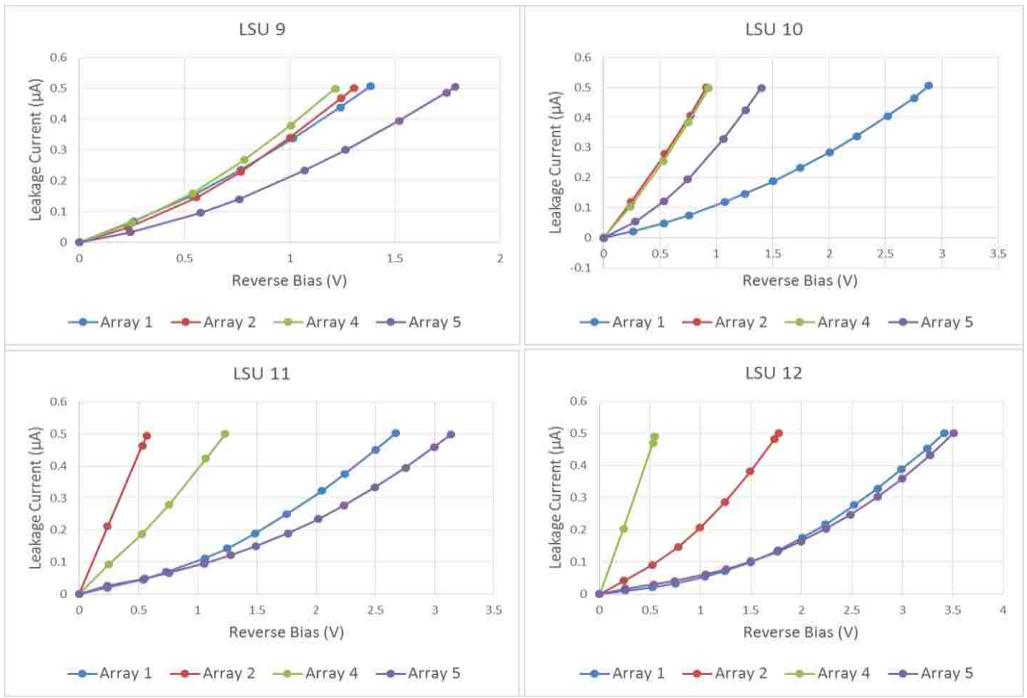

Figure 6.4: LSU I-V plots for chips “LSU 9”, “LSU 10”, “LSU 11”, and “LSU 12”.

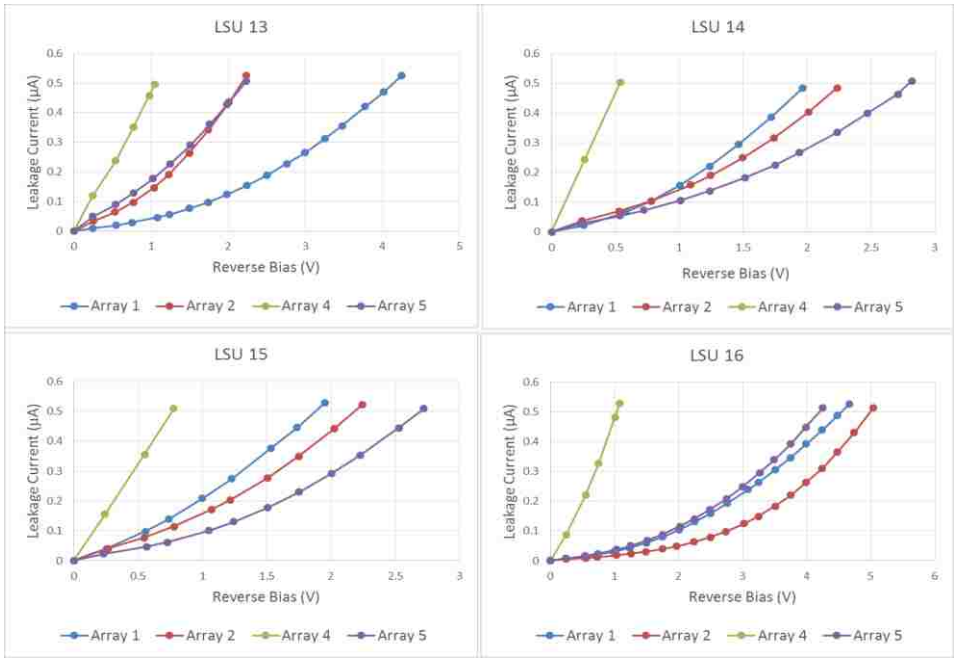

Figure 6.5: LSU I-V plots for chips “LSU 13”, “LSU 14”, “LSU 15”, and “LSU 16”.

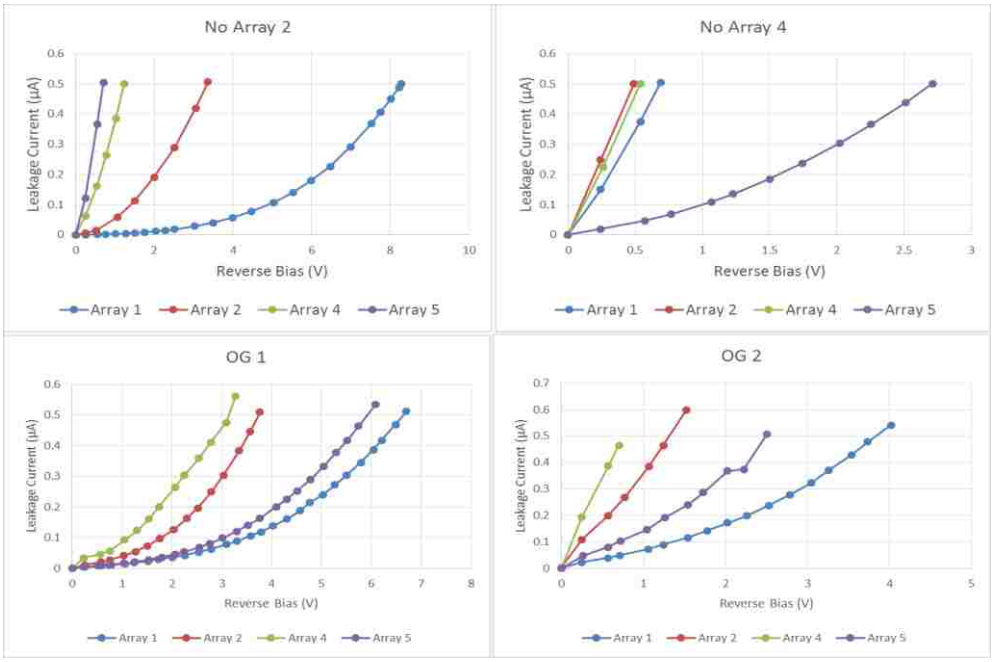

Figure 6.6: LSU I-V plots for chips “No Array 2”, “No Array 4”, “OG 1”, and “OG 2”.

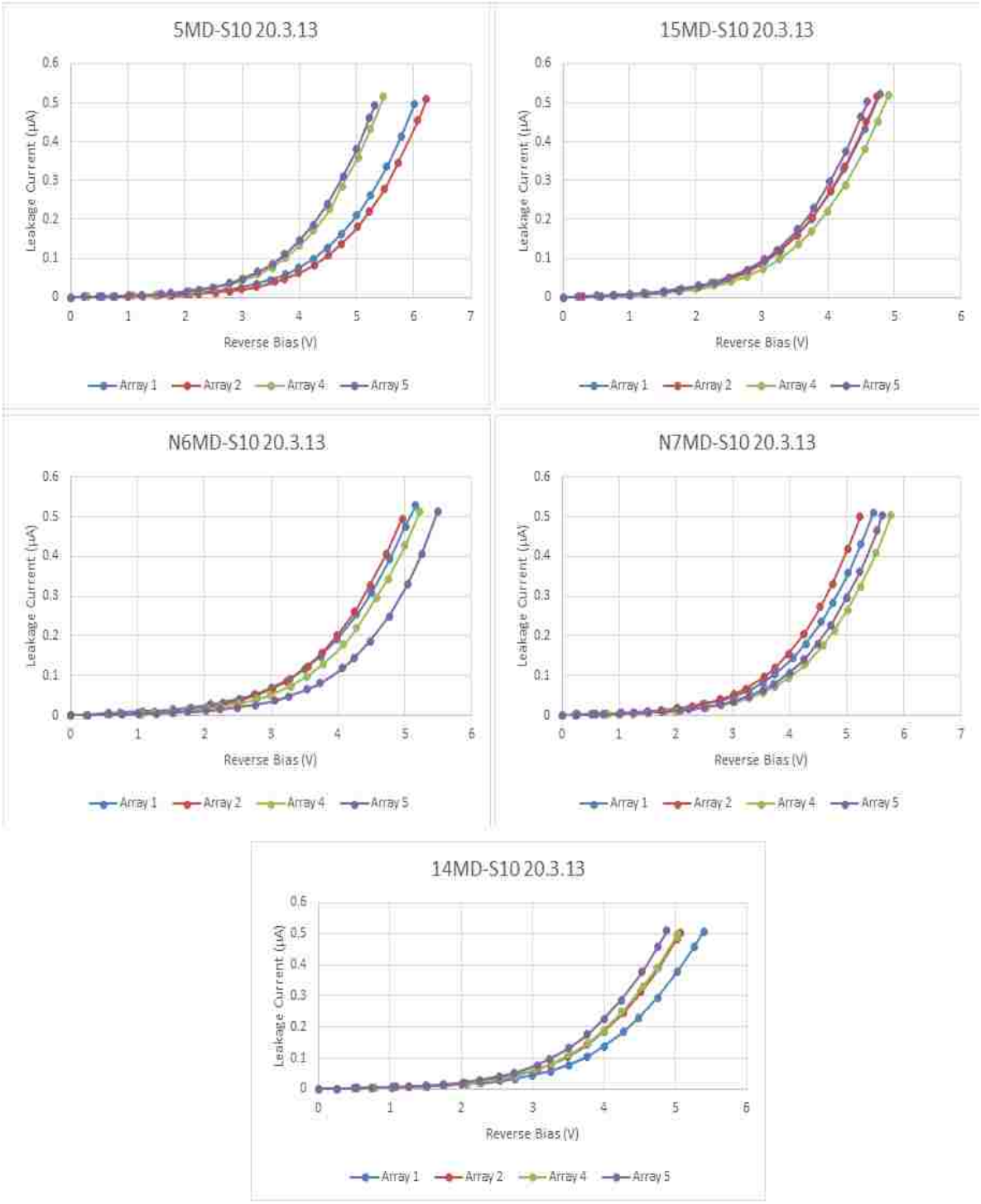

Figure 6.7: LSU I-V plots for UOW chips “5MD-S10”, “14MD-S10”, “15MD-S10”, “N6MD-S10”, and “N7MD-S10”.

6.4 LSU Chip Surface Images

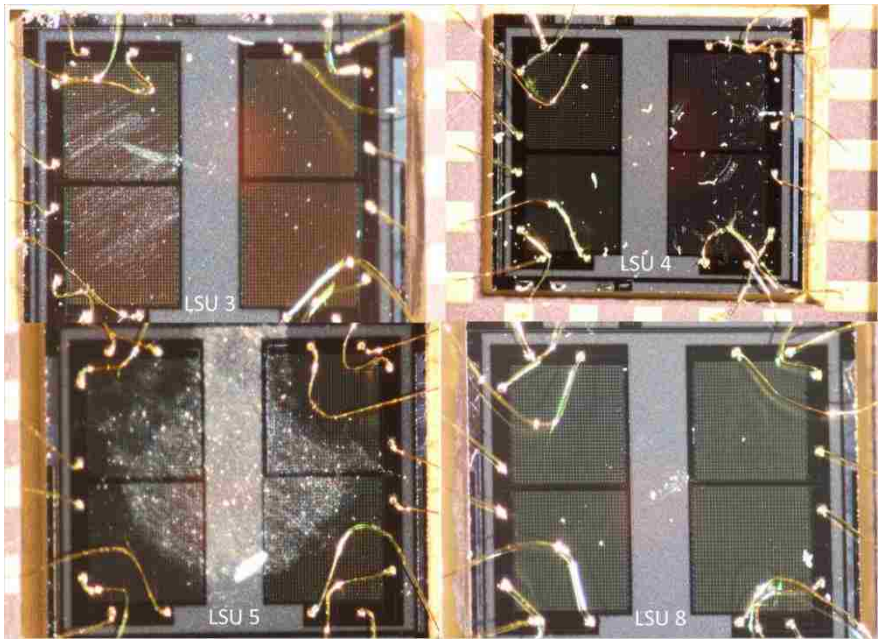

Figure 6.8: Surface images of “LSU 3”, “LSU 4”, “LSU 5”, and “LSU 8”.

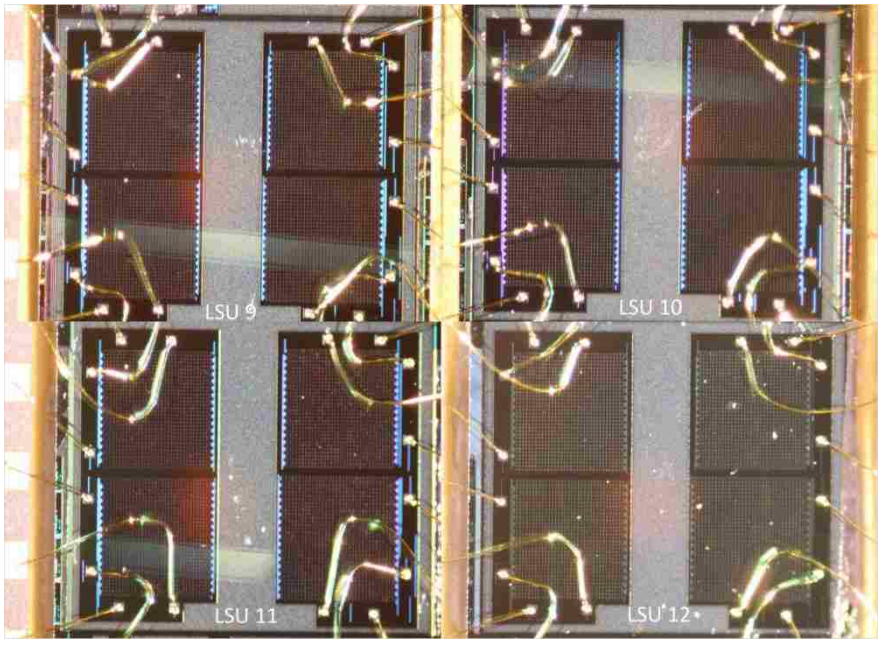

Figure 6.9: Surface images of “LSU 9”, “LSU 10”, “LSU 11”, and “LSU 12”.

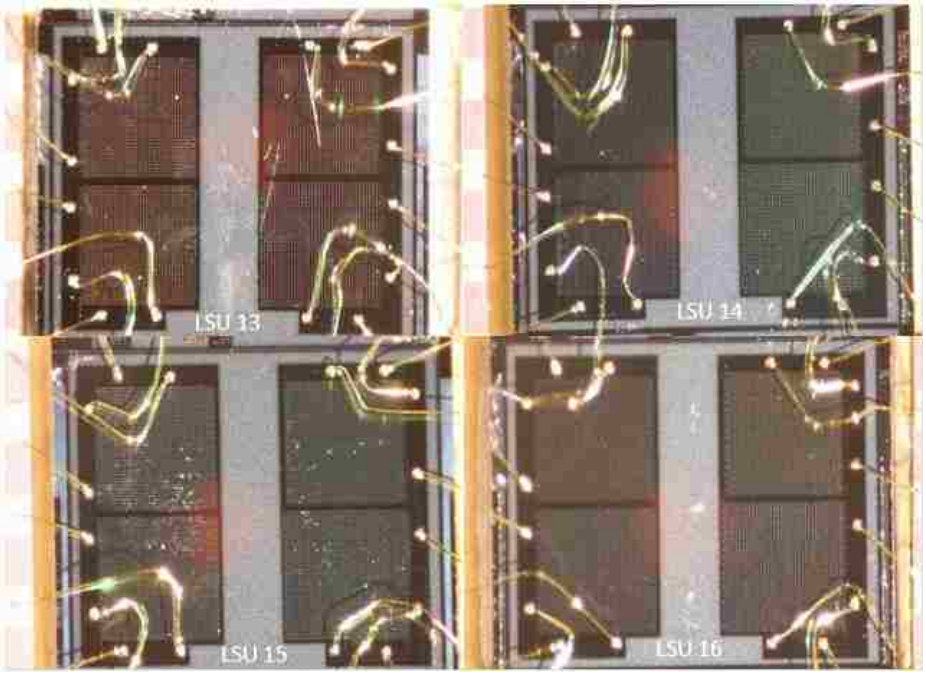

Figure 6.10: Surface images of “LSU 13”, “LSU 14”, “LSU 15”, and “LSU 16”.

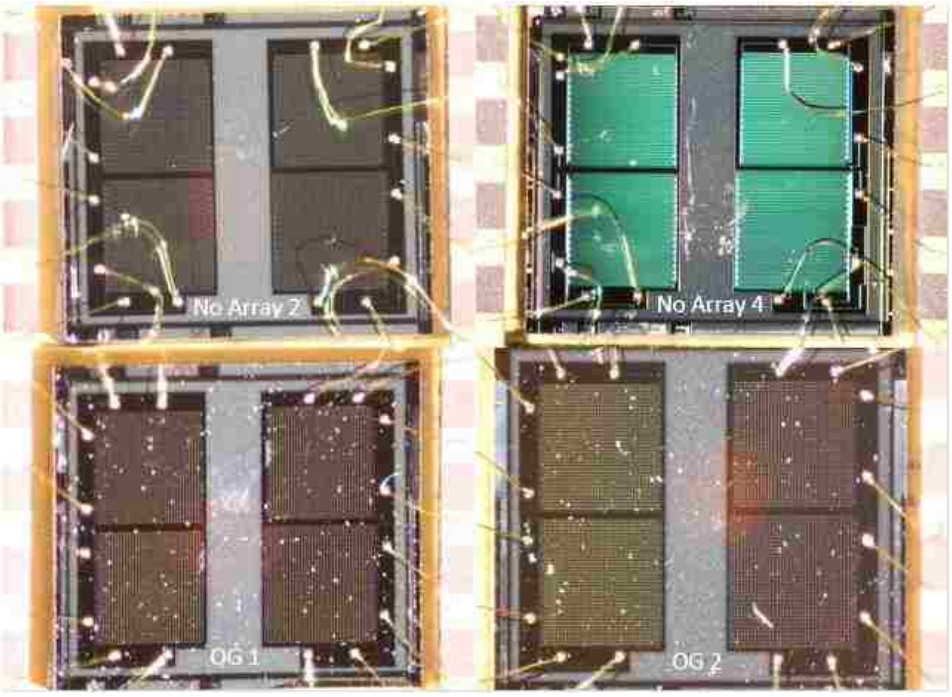

Figure 6.11: Surface images of “No Array 2”, “No Array 4”, “OG 1”, and “OG 2”.

6.5 Results of UOW I-V, and C-V Measurements

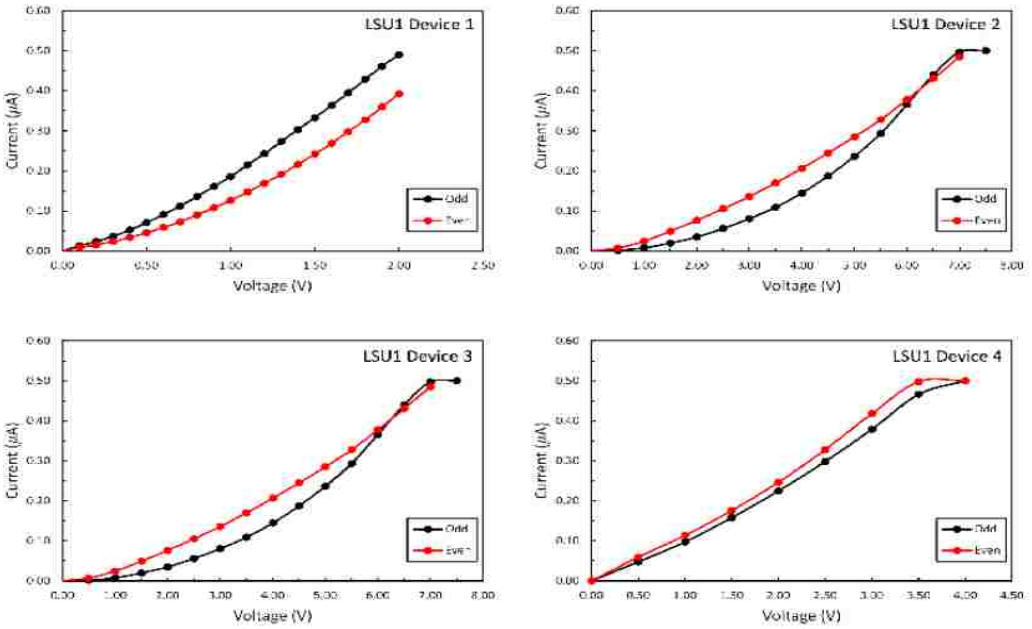

Figure 6.12: “LSU 1” I-V plots from UOW.

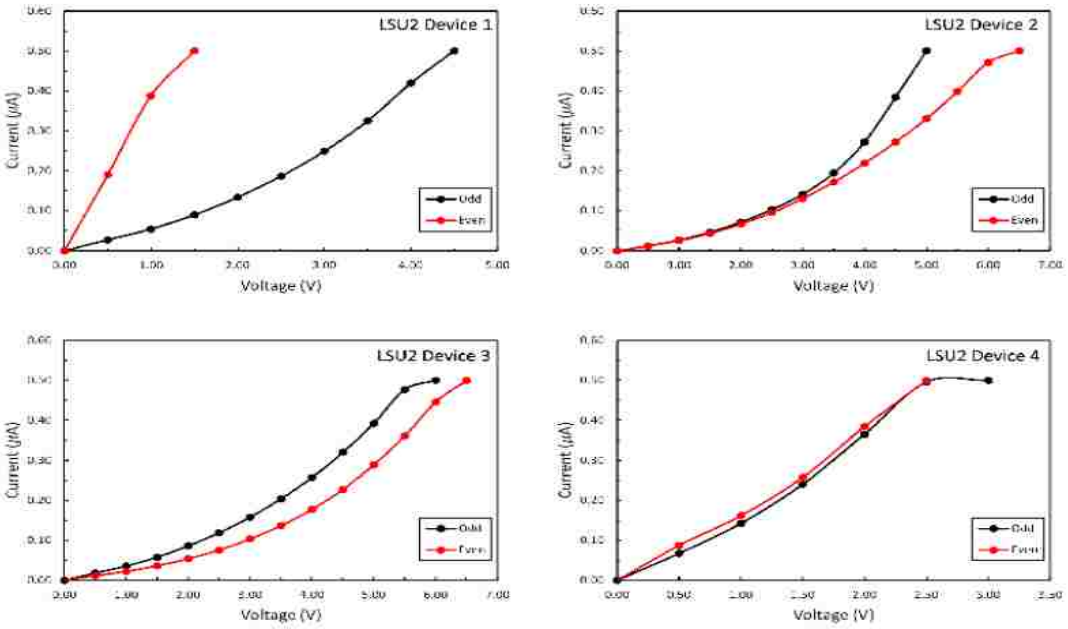

Figure 6.13: “LSU 2” I-V plots from UOW.

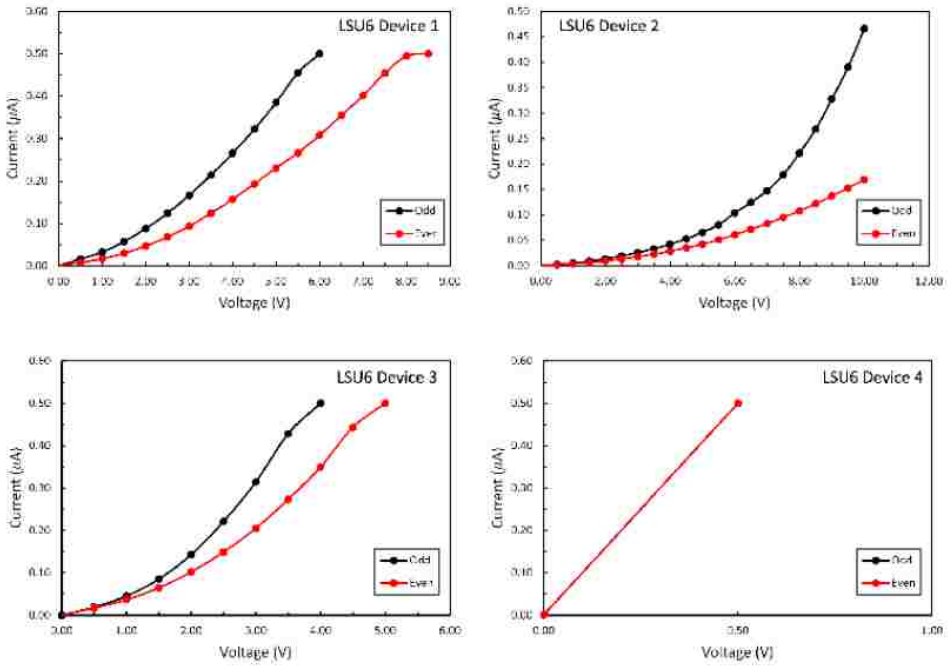

Figure 6.14: “LSU 6” I-V plots from UOW.

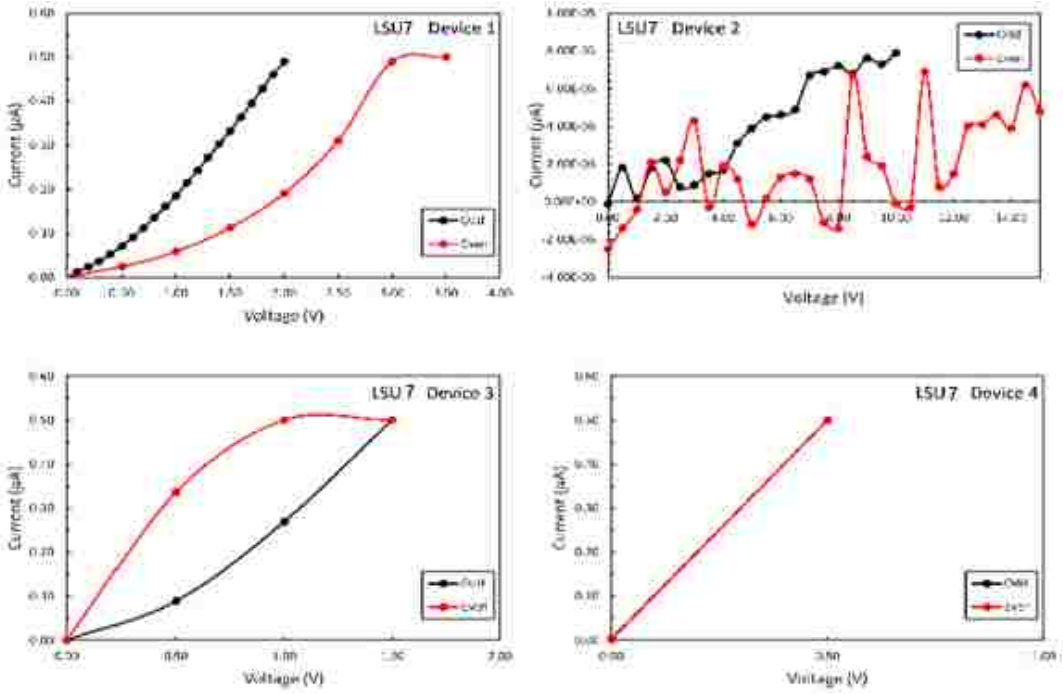

Figure 6.15: “LSU 7” I-V plots from UOW.

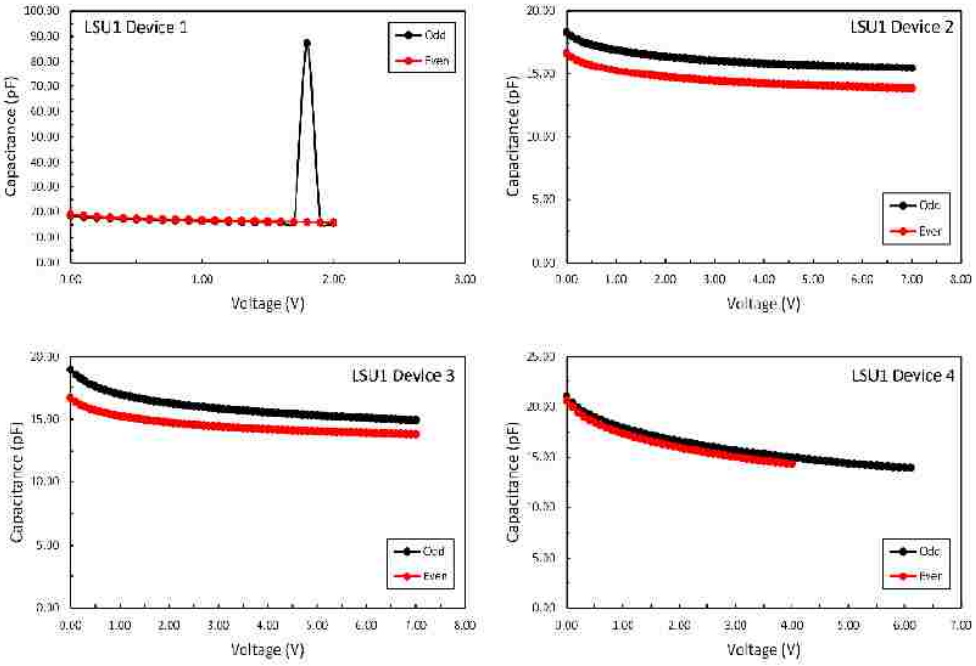

Figure 6.16: “LSU 1” C-V plots from UOW.

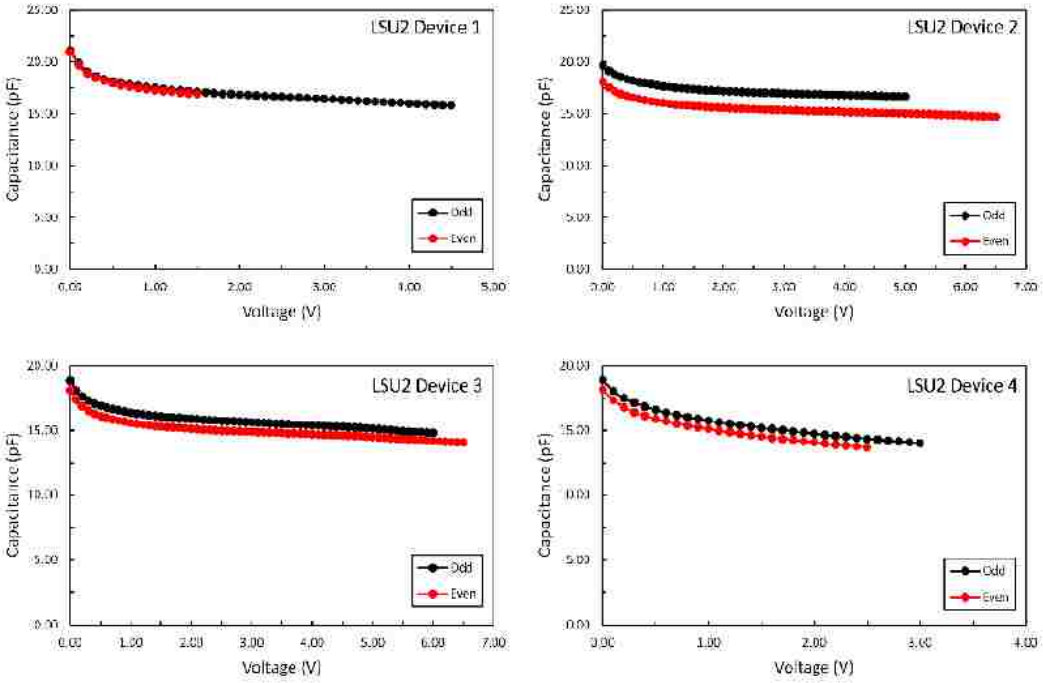

Figure 6.17: “LSU 2” C-V plots from UOW.

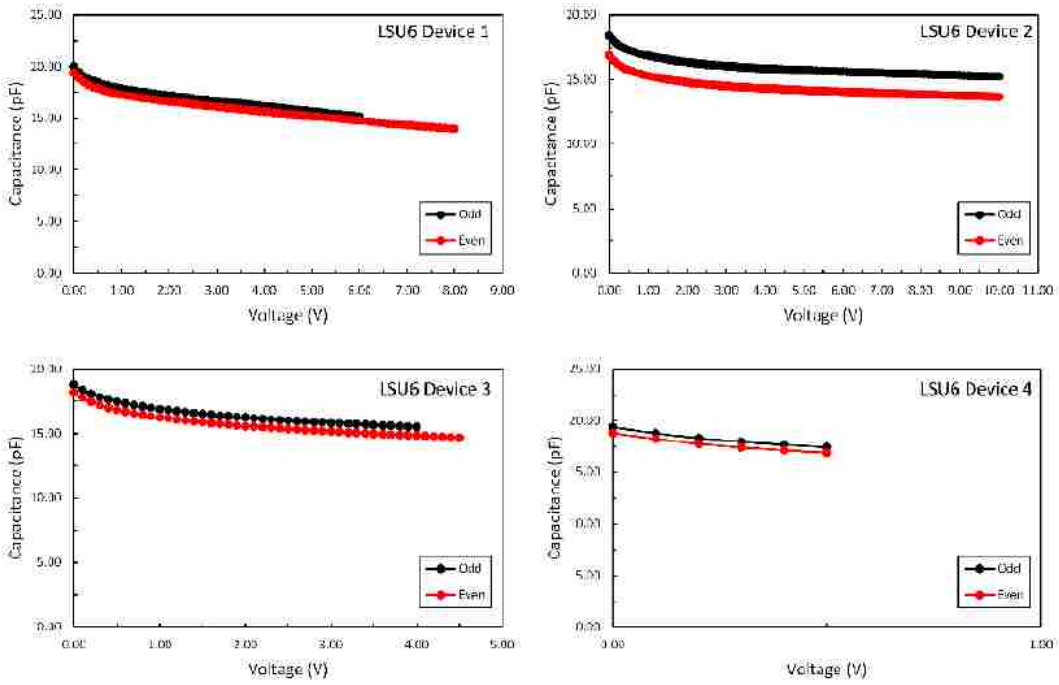

Figure 6.18: “LSU 6” C-V plots from UOW.

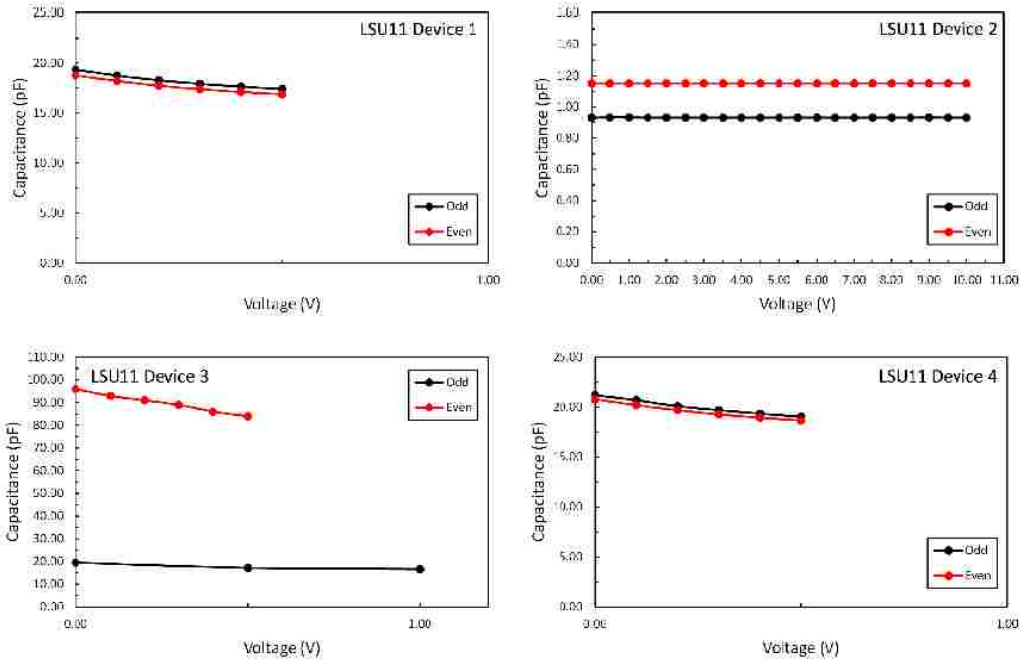

Figure 6.19: “LSU 11” C-V plots from UOW.

VITA

Anthony Mazza grew up outside of Pittsburgh, Pennsylvania. He earned a B.S. in physics from Wheeling Jesuit University in 2006. While an undergraduate, he received his initial training in medical physics through an educational partnership with the Schiffler Cancer Center at Wheeling Hospital. After graduation, he spent a year in New Orleans engaged in Hurricane Katrina relief work through the Jesuit Volunteer Corps, followed by additional volunteer and non-profit endeavors across the country. Returning to Louisiana, and the world of medical physics, he enrolled in the Medical and Health Physics program at Louisiana State University to pursue a Master of Science in Medical Physics. Following graduation, Anthony will be seeking a CAMPEP accredited residency program in medical physics.